UNIVERSITY OF OKLAHOMA

GRADUATE COLLEGE

# PORE CONNECTIVITY IN SHALE FORMATIONS

A DISSERTATION

SUBMITTED TO THE GRADUATE FACULTY

in partial fulfillment of the requirements for the

Degree of

DOCTOR OF PHILOSOPHY

By

DAVUD DAVUDOV
Norman, Oklahoma
2018

Downloaded from SHAREOK. Persistent Handle URL: https://hdl.handle.net/11244/316788

PORE CONNECTIVITY IN SHALE FORMATIONS

A DISSERTATION APPROVED FOR THE
MEWBOURNE SCHOOL OF PETROLEUM AND GEOLOGICAL ENGINEERING

BY

Dr. Rouzbeh G. Moghanloo, Chair

Dr. Dimitrios V. Papavassiliou

Dr. Carl Sondergeld

Dr. Deepak Devegowda

Dr. Siddharth Misra

Dr. Omid Mohammadzadeh

© Copyright by DAVUD DAVUDOV 2018
All Rights Reserved.

## *Dedication*

*To my father and mother, Sarraf and Kemale*

*for their unconditional love and support*

*To my sister and nephew, Mahsati and Samsinur*

*&*

*To Vusale and Masume*

*for always being joy and love in my life*

## Acknowledgements

Once a dream, now reality; this journey would not be possible without the guidance, encouragement, continuous support of my advisor, Dr. Rouzbeh Ghanbarnezhad Moghanloo. I deeply appreciate him for guiding and challenging me to accomplish my dreams.

I am also extremely grateful to my committee members, Dr. Dimitrios V. Papavassiliou, Dr. Carl Sondergeld, Dr. Deepak Devegowda, Dr. Siddharth Misra and Dr. Omidreza Mohammadzadeh for their guidance and support of my research.

I also thank Unconventional Shale Gas Consortium, Dr. Ali Tinni, Dr. Mark Curtis and Joseph Comisky for providing the experimental data that make this research possible.

I want to express my gratitude to the Mewbourne School of Petroleum and Geological Engineering for their support. Thanks to all the friends in Oklahoma for our joyful time we spend together.

To my father, mother, and only sister, thank you for encouraging me in all my pursuits and supporting me to follow my dreams, even when they took me thousands of miles away from you. I owe my deepest appreciation to all of you for your unconditional love and support. I am everything I am, because of you.

Last but not the least I would like to say thanks to my wife and daughter Masume, who have always been by my side and have been joy in my life.

Above all, I owe all my gratitude to God; for all that I am and ever hope to be.

# Table of Contents

Acknowledgements ..... v

Table of Contents ..... vi

List of Tables ..... ix

List of Figures ..... x

Abstract ..... xv

Chapter 1 - Introduction ..... 1

1.1 Pore Connectivity in Shales ..... 4

1.2 Permeability Models – Pore Connectivity ..... 7

1.3 Objective and Outline ..... 8

Chapter 2 - Permeability Model Based on Critical Path Analysis ..... 12

2.1 Introduction ..... 12

2.2 New Critical Path Analysis Model ..... 16

2.3 Evaluation of Permeability Models ..... 18

2.3.1 Results for Tight Sandstone Samples ..... 19

2.3.2 Results for Shale Samples ..... 25

2.4 Discussion ..... 29

2.4.1 Correlation Between Calculated Parameters ..... 29

2.4.2 Limitations of the CPA-based Models ..... 34

2.4.3 Advantages of the CPA-based Models ..... 36

2.5 Conclusions ..... 36

Chapter 3 - Scale Dependent Connectivity of Shale Matrix ..... 38

3.1 Introduction ..... 38

3.2 Accessible Porosity and Permeability ..... 39
3.2.1 Accessible Porosity ..... 39
3.2.2 Permeability ..... 44
3.3 Connected Porosity and Hydraulic Connectivity – Percolation Theory ..... 46
3.3.1 Accessible/Connected Porosity ..... 46
3.3.2 Hydraulic Conductivity and Coordination Number ..... 47
3.4 Conclusions ..... 49
Chapter 4 - Impact of Connectivity Loss on Permeability Reduction ..... 50
4.1 Introduction ..... 50
4.2 Effect of Pore Compressibility and Connectivity Loss ..... 52
4.3 Results ..... 54
4.4 Conclusions ..... 66
Chapter 5 – Permeability Based on SEM Images ..... 68
5.1 Introduction ..... 68
5.2 Methodology ..... 70
5.2.1 Direct Pore Scale Modelling – Lattice Boltzmann Method ..... 70
5.2.2 Pore Connectivity – Euler Poincare characteristics ..... 74
5.3 Results ..... 75
5.3.1 Static Properties ..... 75
5.3.2 LBM Simulation Results ..... 79
5.4 Conclusions ..... 85
Chapter 6 – Accessible Porosity based on MICP ..... 87
6.1 Introduction ..... 87

6.2 Mathematical Model ..... 88
6.2.1 Pore Compressibility Calculation ..... 88
6.2.2 Accessible Pore Calculation ..... 93
6.3 Results and Discussion ..... 94
6.3.1 Pore Compressibility Results ..... 94
6.3.2 Comparison with Ultrasonic Velocity Measurements ..... 98
6.3.4 Accessible porosity ..... 101
6.4 Applications ..... 105
6.5 Conclusions ..... 108
Chapter 7 – Relative Permeability Model Based on Percolation Theory ..... 109
7.1 Introduction ..... 109
7.2 Relative Permeability Model - Phase Connectivity ..... 114
7.2.1 Residual Saturation ..... 117
7.3 Conclusions ..... 120
Chapter 8 – Conclusions and Future Recommendations ..... 121
8.1 Major Contributions and Conclusions ..... 121
8.2 Recommendations for Future Work ..... 122
References ..... 124

# List of Tables

Table 2.1: Input parameters for 60 sandstone samples ..... 21

Table 2.2: Input parameters for 10 shale samples..... 26

Table 3.1: Summary of sample properties obtained with FTIR method..... 39

Table 3.2: Summary porosity and permeability values for different sample sizes..... 45

Table 4.1: Porosity and permeability data for sandstone samples under effective stress ..... 55

Table 4.2: Porosity and permeability data for shale samples under effective stress..... 55

Table 4.3: Calculated parameters for sandstone samples under effective stress ..... 60

Table 4.4: Calculated parameters for shale samples under effective stress ..... 62

Table 5.1: Porosity obtained from 2D slices for Eagle Ford sample ..... 77

Table 5.3: Summary of results for Eagle Ford sample as a function of sample size ..... 85

Table 6.1: Parameters of power law fit function of pore and grain compressibility ..... 97

# List of Figures

Figure 1.1: Methods used to study the pore structure of shales ..... 2

Figure 1.2: SEM images of a) Barnett and b) Haynesville shale ..... 3

Figure 1.3: Pore aspect ratio of the a) Barnett and b) Haynesville ..... 4

Figure 1.4: Three dimensional volumes constructed from SEM images a) all pores b) connected pores ..... 5

Figure 1.5: Porous media considering the valve effects of pore throats ..... 8

Figure 2.1: A 12×12 square lattice model with a) $p = 0.51$ and b) $p = 0.62$ ..... 12

Figure 2.2: Demonstration of critical pore throat radius obtained from MICP data ..... 14

Figure 2.3: Illustration of finding critical pore throat radius from MICP data ..... 20

Figure 2.4: Illustration of finding pore space fractal dimension from MICP data ..... 20

Figure 2.5: Comparison of calculated and measured permeability values (comparative plots) for tight sandstone samples ..... 25

Figure 2.6: Comparison of calculated and measured permeability values (comparative plots) for shale samples ..... 29

Figure 2.7: Interplay among key parameters for sandstone samples a) Maximum pore throat radius as a function of critical pore throat radius; b) Measured permeability as a function of maximum pore throat radius; c) Measured permeability as a function of critical pore throat radius ..... 31

Figure 2.8: Interplay among key parameters for shale samples a) Maximum pore throat radius as a function of critical pore throat radius; b) Measured permeability as a function of maximum pore throat radius ; c) Measured permeability as a function of critical pore throat radius ..... 33

Figure 2.9: MICP test results for unconfined and 7000 psia confining pressure cases ..... 35

Figure 3.1: Mercury injection capillary pressure data for Barnett samples a) Incremental volume b) Cumulative volume..... 40

Figure 3.2: Mercury injection capillary pressure data for Haynesville samples a) Incremental volume b) Cumulative volume..... 41

Figure 3.3: Fraction of accessible porosity as a function of sample size (without corrections)... 42

Figure 3.4: Fraction of accessible porosity as a function of sample size after conformance and compression corrections..... 43

Figure 3.5: Histogram of the MICP porosity fraction from 45 samples in plug size for the a) Barnett and b) Haynesville ..... 43

Figure 3.6: Predicted permeability as a function of sample size ..... 45

Figure 3.7: Average coordination number as a function of sample size for the Barnett and Haynesville shale samples a) Daigle model b) Proposed model ..... 48

Figure 4.1: Porosity as a function of effective stress..... 56

Figure 4.2: Permeability as a function of effective stress..... 57

Figure 4.3: Interconnectivity parameter and coordination number as a function of effective stress for a) sandstone #1 b) sandstone #2..... 58

Figure 4.4: Permeability reduction as a function of effective stress for a) sandstone #1 b) sandstone #2..... 59

Figure 4.5: Plot of $(K/K_0)^{1/3}$ as a function of $ln(P_e/P_o)$ for a) shale #1 b) shale #2..... 61

Figure 4.6: Interconnectivity parameter and coordination number as a function of effective stress calculated from proposed model (after micro-crack closure corrected) for a) shale #1 b) shale #2 ..... 63

Figure 4.7: Permeability reduction as a function of effective stress calculated from proposed model (after micro-crack closure corrected) for a) shale #1 b) shale #2 ..... 64
Figure 4.8: Coordination number ratio as a function of effective stress for different fractal dimension numbers ..... 65
Figure 4.9: Shale gas permeability considering the combined effects of Non-Darcy flow regimes, pore volume shrinkage and pore connectivity loss (solid line) ..... 66
Figure 5.1: Example of 2D grayscale and binary images from Eagle Ford sample ..... 69
Figure 5.2: Major workflow of Chapter 5 ..... 69
Figure 5.3: Velocity discretization in D3Q19 lattice scheme ..... 72
Figure 5.4: Boundary conditions in the LBM ..... 73
Figure 5.5: Euler values for ideal solid objects ..... 75
Figure 5.6: Pore size distribution obtained from 2D slices for Eagle Ford sample ..... 76
Figure 5.7: 3D total and connected porosity for Eagle Ford sample as a function of sample size 78
Figure 5.8: 3D view of Eagle Ford shale sample for a) 1 μm b) 2 μm c) 3 μm d) 4 μm ..... 79
Figure 5.9: LBM Simulation through bundle of tubes a) initial structure b) fluid velocity profile ..... 80
Figure 5.10: 3D view of Berea sandstone a) matrix b) pore ..... 81
Figure 5.11: Velocity magnitude through pore structure Berea sandstone ..... 82
Figure 5.12: 3D view of Eagle Ford shale sample a) matrix b) pore ..... 82
Figure 5.13: Velocity magnitude through pore structure of Eagle Ford sample ..... 83
Figure 5.14: Connected porosity and permeability as a function of sample size ..... 84
Figure 5.15: Connected porosity, permeability, and EPC connectivity as a function of sample size ..... 85

Figure 6.1: Three stages during MICP experiment. ..... 90
Figure 6.2: MICP curve divided into 3 stages. ..... 90
Figure 6.3: Pore compressibility for a) Barnett b) Haynesville ..... 96
Figure 6.4: Grain compressibility for a) Barnett b) Haynesville ..... 97
Figure 6.5: Comparison of bulk compressibility calculated from MICP and velocity measurements for Haynesville samples a) H-2 b) H-3 c) H-4 d) H-5 ..... 100
Figure 6.6: Comparison of bulk compressibility calculated from MICP and velocity measurements ..... 101
Figure 6.7: Results for 11 Barnett samples a) Accessible porosity vs total porosity b) Accessible pore fraction vs total porosity c) Accessible porosity vs MICP porosity without any corrections d) Accessible porosity vs conformance and grain compression corrected MICP porosity ..... 102
Figure 6.8: Results for 11 Haynesville samples a) Accessible porosity vs total porosity b) Accessible pore fraction vs total porosity c) Accessible porosity vs MICP porosity without any corrections d) Accessible porosity vs intrusion corrected MICP porosity ..... 103
Figure 6.9: Contribution of each correction factor on calculated accessible porosity a) Barnett b) Haynesville ..... 105
Figure 6.10: Volume contribution from intrusion and compaction (Sample B11) ..... 106
Figure 6.11: Mercury saturation curve from MICP data (Sample B1) ..... 107
Figure 6.12: Pore size distribution calculated from MICP data (Sample B1) ..... 107
Figure 7.1: Relative permeability results for shale sample #1 (Calmar) ..... 112
Figure 7.2: Relative permeability results for shale sample #2 (Colorado) ..... 113
Figure 7.3: Illustration of phase connectivity as a function of saturation ..... 114
Figure 7.4: Coordination number of the saturating phase as a function of saturation ..... 116

Figure 7.5: Relative permeability estimated from Eq. 7.14 ..... 117

Figure 7.6: Difference between mercury intrusion and extrusion versus pore body to throat ratio shows a directly proportional relationship ..... 119

Figure 7.7: Residual saturation as a function of phase connectivity ..... 120

# Abstract

Shale formations demonstrate distinct characteristics, such as a wide spectrum of pore size from micro-scale to nano-scale, ultra-low permeability, and complex pore network system. Despite extensive research work over years to characterize details of shale and extremely tight formations, the interplay between pore connectivity and permeability still remains to be understood. In this research, analytic and numerical methods were used in tandem with experimental data to characterize and evaluate pore and hydraulic connectivity of shale formations. Impact of sample size, effective stress, pore structure and topology on the connectivity were evaluated.

A new analytic model is proposed and developed using percolation theory and critical path analysis to explicitly express permeability as a function of pore connectivity. The definition of critical pore throat radius and electrical conductivity were revisited and reformulated from previously developed Katz & Thompson model. The new permeability model is expressed as a function of maximum pore radius, porosity, fractal dimension, and percolation threshold/average coordination number that makes it suitable for exploring the impact of pore connectivity on permeability.

Next, accessible porosity and interconnected porosity is evaluated using mercury injection capillary pressure (MICP) data. Several samples from Barnett and Haynesville formations with different sizes are used to understand the effect of sample size on accessible and interconnected porosity. MICP data combined with percolation theory were used to explain the connectivity loss with increasing sample size.

Additionally, a novel approach is presented to explain intrinsic permeability reduction of shale samples as a function of effective stress. Experimental results have shown orders of magnitude reduction in permeability as effective stress increases; this permeability reduction is usually explained through closure of micro-fracture while impact of pore connectivity loss is often

neglected. Thus, an alternative approach is proposed here through which permeability reduction is described owing to combination of three main mechanisms: (1) micro crack closure (2) pore shrinkage and (3) connectivity loss due to bond breakage between interconnected pores.

Next, a complementary study was conducted to model fluid flow through three-dimensional (3D) pore structure constructed using stacked focused ion beam scanning electron microscopy (FIB-SEM) images. Lattice Boltzmann Method (LBM) is used to simulate fluid flow to calculate permeability of the 3D pore volume. Finally, pore connectivity is quantified based on Euler-Poincare Characteristics as a function of sample size and impact of pore connectivity on permeability calculations is analyzed.

Furthermore, accessible/fluid saturated porosity values calculated using mercury injection capillary pressure (MICP) data are evaluated for Barnett and Haynesville shale samples. A general approach is proposed consisting of three distinct corrections to accurately estimate the accessible porosity of shale sample using MICP data: (1) conformance, (2) grain compressibility, and (3) inaccessible pore compressibility. Accessible porosity calculated for both Barnett and Haynesville formations have been analyzed and compared to understand the impacts of pore structure and topology on the connectivity.

Finally, a two-phase relative permeability model based on percolation theory is proposed and impact of the phase connectivity on relative permeability curves is investigated. Additionally, major factor dominating residual saturation is discussed.

The result of this study suggests that in shale formations accessible porosity and permeability are strong function of pore/hydraulic connectivity. Moreover, unlike conventional formations, pore connectivity can significantly vary depending on pore structure, pore geometry, sample size, and the effective stress.

# Chapter 1 - Introduction

As production from shale plays maintain its role as one of the main energy resources in the U.S., prediction of formation deliverability during the production life becomes a decision-making factor for future investments. Shale formations have distinct characteristics such as low porosity, nano-scale pores, extremely low permeability, and complicated microstructure; hence, production from these very tight formations becomes very challenging and expensive. According to International Union of Pure and Applied Chemistry (IUPAC) definition, shale matrix can be considered a combination of microporous, mesoporous, and macroporous systems depending upon the scale we select to study. IUPAC defines microporous material a system where pores have diameters of less than 2 nm; mesoporous material a system with pore diameters between 2 nm and 50 and macroporous material where pore diameters are greater than 50 nm.

The complexity of shale reservoirs can, in part, be attributed to the geological and petrophysical heterogeneity of the reservoir rocks themselves. Shales are fine-grained sedimentary rocks with more than 67% of their grains smaller than 5 μm in diameter comprised of common minerals such as silica dioxide; the shale matrix also may contain considerable amounts of clays, silt, mud and organic matter (Kuila et al., 2012; Sondergeld et al., 2010a, 2010b).

Microstructure, pore structure and characteristics of unconventional reservoirs are critical parameters which control storage capacity and flow properties of reservoir. However, because of their ultra-fine size associated with broad pore size distribution makes it challenging to characterize these microstructures. Thus, as summarized in **Figure 1.1,** an extensive research with hybrid techniques including combination of fluid intrusion, imaging and/or radiation methods have been conducted to study shale microstructure features from micrometer to nanometer scale (Bustin et al., 2008; Chalmers et al., 2012; Clarkson et al., 2012; Curtis et al., 2011).

Shale reservoirs are mainly composed of the inorganic minerals and the organic matter; wherein, the latter is an essential constituent of a productive shale gas reservoir (Potter et al., 2005). Because of their completely unlike nature and properties, these components will also affect the reservoir characteristics significantly. Generally, 70-94% by volume of rock composition is composed of the inorganic minerals such as clays, carbonate and quartz (Tinni, 2015). On the other hand, organic matter is usually quantified by total organic carbon (TOC) and might be in both solid and liquid forms.

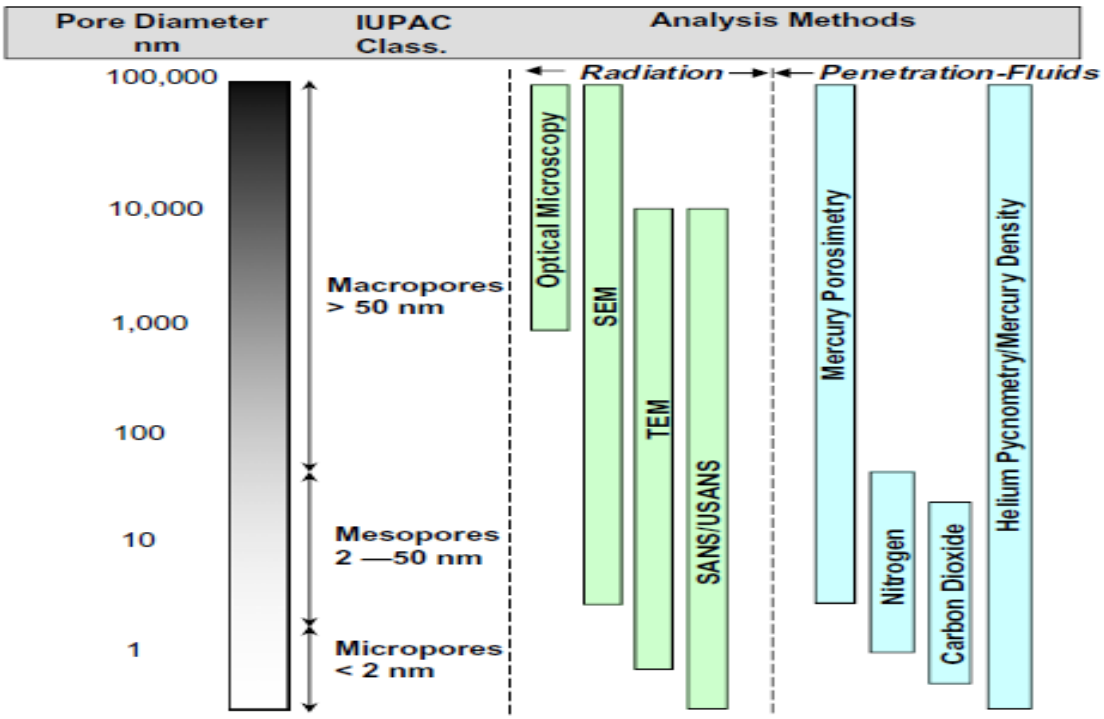


**Figure 1.1: Methods used to study the pore structure of shales (Bustin et al., 2008)**

Small grains combined with the clay minerals generate multifarious types of pore with different shape and geometry. Pores are observed at various locations inside the shale matrix; the porosity in the Barnett is dominantly within the organic matter (Loucks et al., 2012, 2009), where the

porosity in the Haynesville shale is most prevalent in the inorganic part (Chalmers et al., 2012; Curtis et al., 2011).

High resolution images obtained from scanning electron microscopy (SEM) technique are widely used to analyze the high degree heterogeneity at desired spatial scale in shale formations. A distribution of nanometer size of inorganic and organic pores has been observed and investigated based on SEM imaging technique (Curtis et al., 2011, 2010, Loucks et al., 2012, 2009; Pommer and Milliken, 2015; Tran et al., 2017). **Figure 1.2** illustrates an example for SEM images obtained from Barnett and a Haynesville shale samples (Davudov et al., 2016; Davudov and Ghanbarnezhad Moghanloo, 2016). In the Barnett sample, the darker material is the organic matter, while the lighter gray matrix is composed mostly of quartz and clays. It is observed that most of the porosity resides within the organic matter, with only a few pores located within the inorganic matrix. Grayscale segmentation of the pores resulted in a porosity of 3.2% by area, and an average aspect ratio of 1.61. The average aspect ratio indicates that most of the pores tend to be more circular in nature. In contrast, the porosity in the Haynesville shale image (segmented porosity 4.7%) is located primarily in the inorganic matrix.

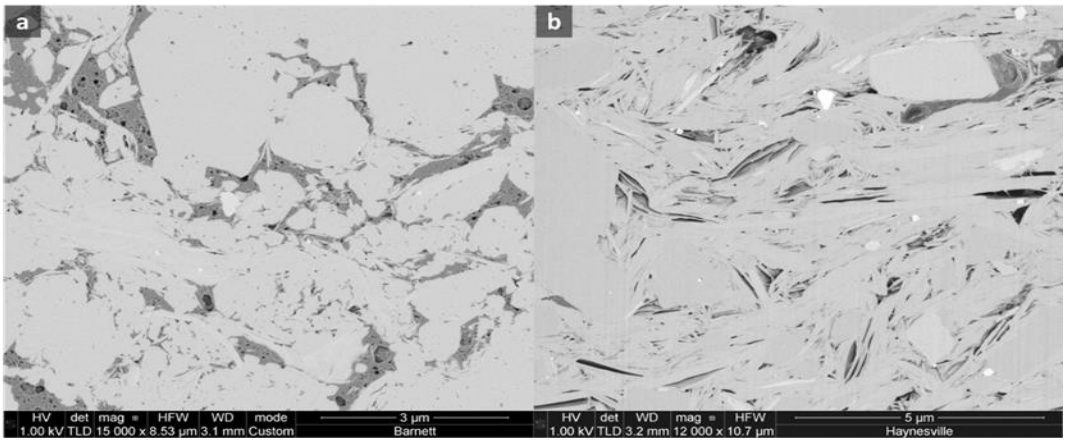


**Figure 1.2: SEM images of a) Barnett and b) Haynesville shale (Davudov et al., 2016)**

Due to the host material, the shape of the pores in this image are more elongated than those observed in Barnett samples, with an average aspect ratio of 2.77. Histograms of the aspect ratios for both samples are shown in **Figure 1.3**. The Haynesville has a significant population of pores with aspect ratios greater than 2.00 (Davudov and Ghanbarnezhad Moghanloo, 2016).

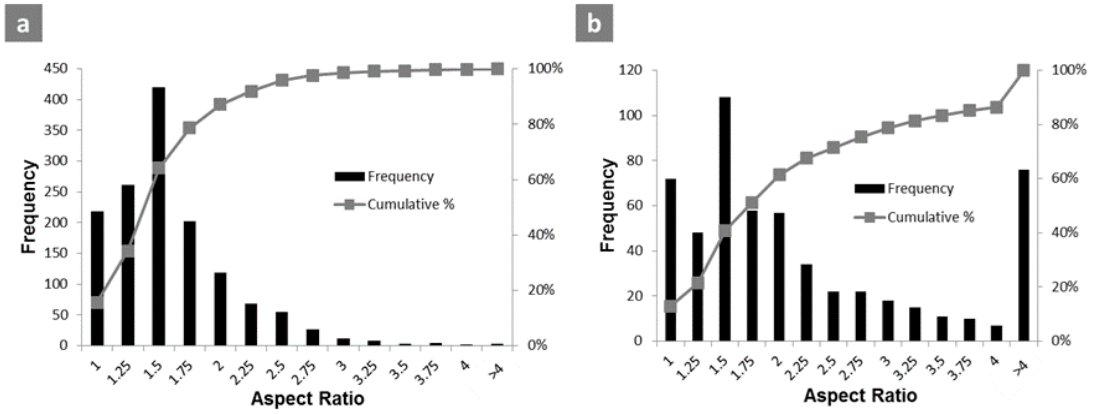


**Figure 1.3: Pore aspect ratio of the a) Barnett and b) Haynesville (Davudov et al., 2016)**

### 1.1 Pore Connectivity in Shales

Pore connectivity is one of the crucial parameters affecting effective porosity and fluid transport/permeability. Numerous studies have constructed three-dimensional volume of shale sample obtained from the scanning electron microscopy (SEM) technique (Curtis et al., 2012b, 2011; Sisk et al., 2010) and further analyzed for total and connected pore system as illustrated in **Figure 1.4**.

Mercury injection capillary pressure (MICP) is another widely used experimental techniques to evaluate pore throat size and pore connectivity in shale formations. Compared to other experimental techniques, the major advantages of MICP test is that they give direct information about pore throats which is the key parameter for hydraulic conductivity and fluid transport (Hu et al., 2015; King et al., 2015; Klaver et al., 2015). Moreover, in the literature it has been reported

that shale porosity calculated from MICP test is strong function of sample size; mercury porosity is decreasing with increasing sample size and it has been suggested that this is due to the effect of restricted pore connectivity (Comisky et al., 2011; Tinni et al., 2014).

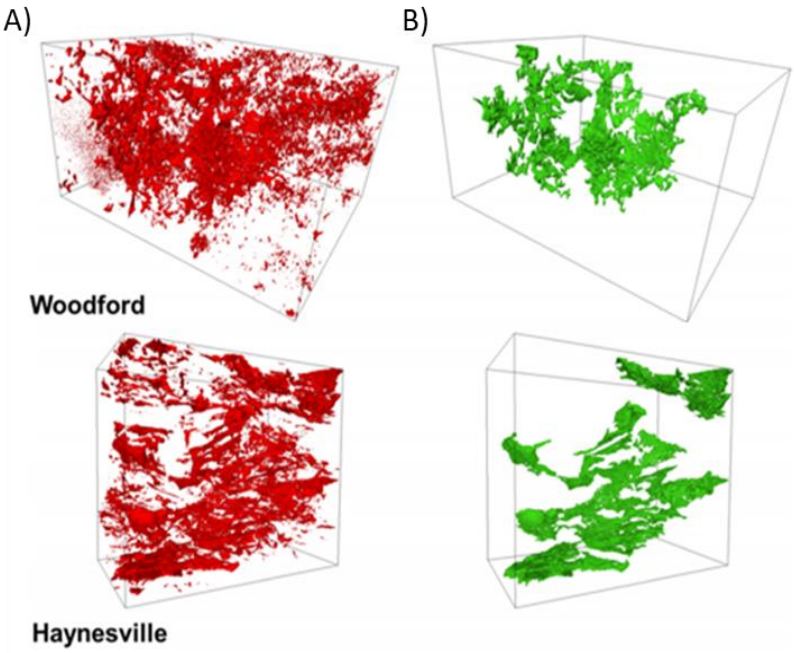


**Figure 1.4: Three dimensional volumes constructed from SEM images a) all pores b) connected pores (Curtis et al., 2012b)**

To further investigate pore connectivity, numerous studies have used Wood's metal injection into shale samples (Hu et al., 2014; Klaver et al., 2015), which later SEM images of the samples are analyzed to understand how and which part of the pores are connected. It has been observed that Wood's metal essentially penetrated the edge pores, and micro-cracks, where the concentration of Wood's metal in the middle section of sample can be as low as 0.1% of the concentration at the edges (Hu et al., 2014). Moreover, since shales have pores associated with the inorganic minerals and the organic matter Tinni (2012) has suggested to consider effect of pore wettability on pore connectivity as well.

Alternatively, some studies have evaluated pore connectivity in terms of average pore throat number, usually defined as coordination number. After analyzing 3D shale microstructure constructed from SEM images, pore network is extracted and coordination number in shale is calculated in the range of 3 (Ma et al., 2014; Yang et al., 2015), where this value is around 6-8 in sandstone samples.

More importantly, in conventional samples, pore connectivity is considered a constant parameter that remains intact in most of the applications; however, asphaltene deposition and fines migration may adversely affect and plug the flow path (Davudov and Moghanloo, 2019; Moghanloo et al., 2018). Because pore connectivity is high in conventional rock samples, tortuosity parameter is often considered as the primary parameter in permeability models and calculations.

However, it has been well accepted that the pore connectivity in shale formations is very weak and unlike conventional formations, pore connectivity in shale formations might be further reduced due to mechanisms like sample size, effective stress, deposition of precipitates such as asphaltene deposition during production life. As an example, based on experimental research it has been reported that during huff and puff gas injection permeability of the Eagle Ford shale sample has been reduced as much as 300%; 83% of total permeability is reduced owing to pore blockage and 17 % reduction was due to adsorption mechanism (Shen and Sheng, 2017). Consequently, conventional approaches used to characterize and formulate pore connectivity in shale formations are not sufficient enough; hence, tortuosity appears to become the secondary parameter affecting fluid transport, in the absence of “strong” pore connectivity. Thus, the main question remains to be addressed (the main goal of this dissertation) is how to quantify the connectivity or connectivity loss in shale and ultra-tight formations.

## 1.2 Permeability Models – Pore Connectivity

The interplay between porosity/storage and permeability/hydraulic conductivity has been studied for decades. As a result, many theoretical models have been developed to estimate permeability of porous media (Bernabe et al., 2010; Civan, 2001; Doyen, 1988; Pape et al., 2000), where many early models were considering porous media as a bundle of capillary tubes. One of the fundamental permeability models is Kozeny-Carmen (KC) equation (Carman, 1937), which relates permeability to porosity ( $\phi$ ), tortuosity (τ), hydraulic pore radius ($r_h$), and constant term (c):

$$K = \frac{r_h^2}{c}\frac{\phi}{\tau}, \tag{1.1}$$

Many variations of the KC model have been proposed in the literature. Based on the assumption that the electrical field lines and the fluid stream lines are identical, the equivalent channel model is proposed (Walsh and Brace, 1984):

$$K = \frac{r_h^2}{c}\frac{\sigma_b}{\sigma_w}, \tag{1.2}$$

where $r_h$ is hydraulic radius, $\sigma_b$ is bulk electrical conductivity, and $\sigma_w$ is saturating fluid electrical conductivity (Han and Misra, 2018; Tathed et al., 2018).

Later, Civan (2011) suggested that the KC equation cannot properly address the gate /valve effect and predict permeability when pore throats are blocked. The blockage of pore throats creates isolated pores; therefore, the KC equation needs to be modified to include an interconnectivity parameter, Γ as:

$$k = \Gamma\phi\left(\frac{\phi}{1-\phi}\right)^{2\eta} \tag{1.3}$$

where $\eta$ is the exponent usually considered as 1 and Γ is a measure of the pore space connectivity which represents the valve effect of the pore throats (**Figure 1.5**). The number of pore throats

(coordination number) and the valve effect controls the pore and hydraulic connectivity in an interconnected network (Civan, 2011). Consequently, **Eq. 2.3** predicts that permeability can become zero even if the porosity is nonzero.

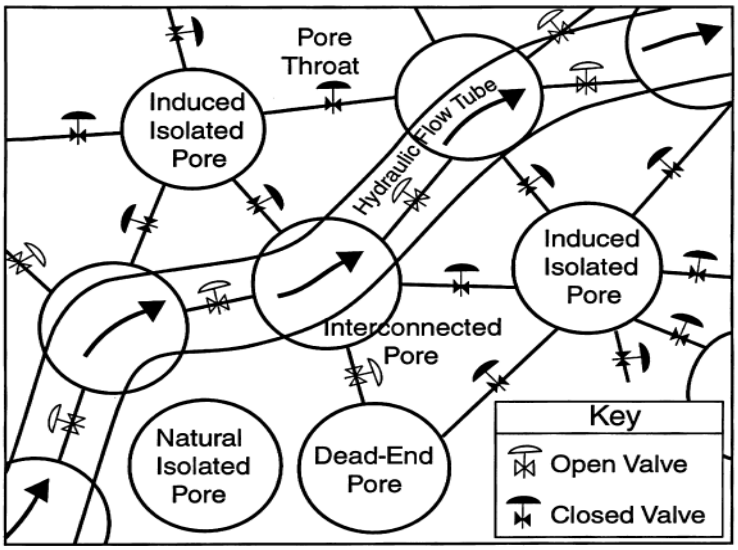


**Figure 1.5: Porous media considering the valve effects of pore throats (Civan, 2011)**

Although KC type equations are widely used, these models cannot address pore/hydraulic interconnectivity effect properly. Thus, alternative models based on percolation theory which is the study of pathways in disordered media (Hunt and Gee, 2002; Hunt, 2001; Sahimi, 1995) were developed to address issues associated with bundle of capillary tube hypothesis.

Percolation theory is considered one of the best approaches to model permeability while accounting the impact of pore connectivity (Bernabe et al., 2010; Hu et al., 2015). The most important advantage of percolation theory-based permeability models is that the pore connectivity can be expressed explicitly, which will allow to evaluate it separately.

## 1.3 Objective and Outline

This dissertation examines effect of various parameters on pore connectivity in shale and ultra-tight formations. The research is driven by the following *hypothesis*: *Pore connectivity is a scale-*

*dependent property governing fluid flow in shale formations and additional connectivity loss may occur because of pore throat closure and/or two-phase phenomena.*

The main objectives of the work are as follows:

**Obj. 1:** Develop an analytic permeability model based on percolation theory to evaluate impact of pore connectivity

**Obj. 2:** Evaluate pore connectivity loss as a function of sample size and under effective stress.

**Obj. 3:** Assess permeability of shale sample obtained from stacked SEM images and evaluate impact of connectivity on permeability calculations.

**Obj. 4:** Evaluate accessible porosity based on mercury injection capillary pressure (MICP) data.

**Obj. 5:** Investigate connectivity loss in two phase flow systems.

In Chapter 2, the first objective is addressed where a new permeability model is developed using critical path analysis (CPA). In CPA based models, critical pore throat radius and electrical conductivity are considered as the key parameters of the pore network. The definition of both parameters in Katz and Thompson model is revisited and a new permeability model is developed as a function of maximum pore throat radius, porosity, fractal dimension, and percolation threshold/average coordination number. Two different datasets are used to validate proposed model: 1) experimental data obtained for 60 tight sandstone samples and 2) 9 shale samples with experimentally measured permeability values.

Chapter 3 addresses the second objective where pore and hydraulic connectivity of shale formations is investigated based on mercury injection capillary pressure (MICP) data and percolation theory for different sample sizes. Using MICP data measured at the laboratory for different sample sizes, accessible porosity and permeability are estimated for Barnett and

Haynesville samples. Next, pore and hydraulic connectivity (average coordination number) for both Barnett and Haynesville samples are evaluated using percolation theory.

In Chapter 4, aligned with second objective, a novel approach is examined to describe how connectivity loss impacts intrinsic permeability of shale formations under effective stress levels. Significant permeability reduction under effective stress is observed for shale samples; the permeability reduction is often explained due to micro-fracture closure and impact of pore connectivity loss is often neglected. Thus, an alternative model is proposed here through which permeability reduction is described owing to combination of three main mechanisms: (1) micro crack closure at early stage (2) pore shrinkage and (3) connectivity loss due to bond breakage between interconnected pores at later stage.

Chapter 5 presents numerical simulation of fluid flow through intrinsic pore structure of Eagle Ford shale sample obtained from stacked SEM images to address the third objective. Permeability values obtained from simulation models are analyzed to understand impact of sample size on permeability reduction in shale formations. Further, pore connectivity of studied shale sample has been evaluated which is defined based on Euler Poincare Characteristics.

Chapter 6 examines the fourth objective where a novel approach is proposed to correct accessible/fluid saturated porosity values calculated using mercury injection capillary pressure (MICP) for shale samples. A mathematical model is developed consisting of three distinct corrections to accurately estimate accessible porosity of shale sample using MICP data: (1) conformance, (2) grain compressibility, and (3) inaccessible pore compressibility. Samples from both Barnett and Haynesville shale plays (11 samples for each shale plays) are used to validate the proposed methodology.

In Chapter 7, the fifth objective is addressed. In this chapter, percolation theory has been applied to expresses relative permeability for two phase flow system. Previously developed models with their underlying assumptions and limitations have been discussed and an alternative model is proposed to improve limitations of previous models. Experimentally measured relative permeability results from literature were then used to validate the proposed models. Furthermore, impact of phase connectivity on the relative permeability and residual saturation of non-wetting phase is discussed.

Finally, Chapter 8 provides a summary of this dissertation's findings, conclusions, and future suggestions.

# Chapter 2 - Permeability Model Based on Critical Path Analysis

## 2.1 Introduction

In this chapter, **Obj. 1** is sought to develop a permeability model, based on critical path analysis, such that impact of pore connectivity can be explicitly evaluated. As discussed earlier, traditional permeability models based on capillary tube hypothesis are not sophisticated enough to address the complex pore network in tight formations. Thus, percolation theory-based models were developed to address issues associated with bundle of capillary tube models.

In percolation theory, the minimum fraction of pore volume required to be filled to form a connected cluster is called critical percolation threshold ($p_c$). The percolation threshold is an important parameter, as the flow behavior drastically changes at that point. A typical square site model is illustrated in **Figure 2.1** where 51% of sites in left figure and 62% of sites in right side figure are occupied. Percolation threshold for 2D square lattice is around 59.75%, which is why connected cluster can be only formed in the right case.

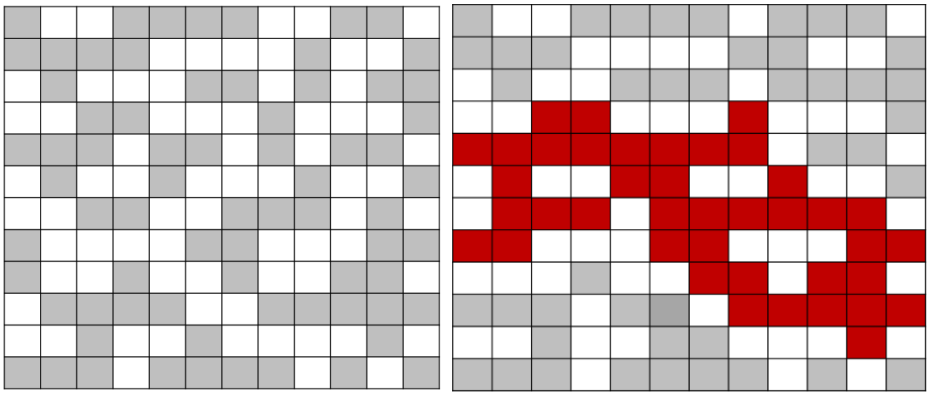

**Figure 2.1: A 12×12 square lattice model with a) $p = 0.51$ and b) $p = 0.62$. Grey boxes are occupied parts, however the largest cluster (red) which connects left and right boundaries occurs above percolation threshold**

Based on percolation theory, in cylindrical pores, the electrical conductance, $g_e$ is expressed as:

$$g_e = \frac{\pi \sigma_w r^2}{l}, \tag{2.1}$$

Correspondingly hydraulic conductance, $g_h$ is given as:

$$g_h = \frac{\pi r^4}{8\mu l}, \tag{2.2}$$

where $\sigma_w$ is the electrical conductivity of the fluid saturating the pore, μ is dynamic viscosity, and $l$ is the pore length along which fluid flows. Friedman and Seaton (1998) and Hunt (2001) have suggested that in porous media macroscopic conductance is equal to critical conductance ($g_m = g_c$). Thus, combing **Eq. 2.1** and **2.2** permeability can be related to electrical conductivity and critical pore diameter which is the bases of critical path analysis (CPA) (Skaggs 2011):

$$k = \frac{r_c^2}{c} \frac{\sigma_b}{\sigma_w}, \tag{2.3}$$

where, $r_c$ is critical pore radius which is defined as the largest value of radius for which an interconnected path may exist across the system length from one side toward the other side (**Figure 2.2**). Katz and Thompson (1986, 1987) model was one of the earliest attempts to apply CPA; they defined electrical conductivity as a function of porosity, critical pore radius, pore throat radius corresponding to the optimal path of electrical conductivity, $r_e$, and volume fraction associated with the connected pore space that includes pore throat sizes $r_e$ and greater, $S(r_e)$, as:

$$k = \frac{r_c^2}{c} \frac{r_e}{r_c} \phi S\left(r_e\right) \tag{2.4}$$

Alternatively, they have expressed permeability as a function of the effective pore throat diameter corresponding to the highest hydraulic conductance, $r_h$:

$$k = \frac{r_h^2}{c} \frac{r_h}{r_c} \phi S\left(r_h\right) \tag{2.5}$$

Katz and Thompson (1986, 1987) argued that both critical pore radius and formation factor can be estimated from mercury intrusion capillary pressure (MICP) data and used a set of 50 samples with absolute permeability ranging from 0.005 to 5000 md to validate their model.

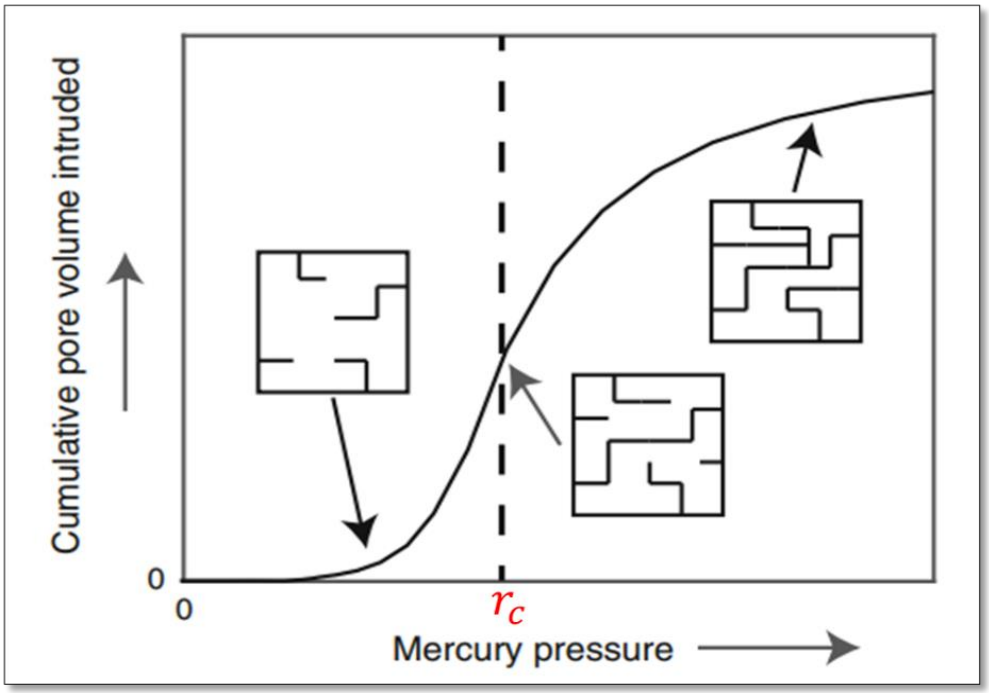


**Figure 2.2: Demonstration of critical pore throat radius obtained from MICP data (Adopted from Daigle and Johnson 2015)**

Later, Hunt (2001) integrated fractal and percolation theories to express critical pore radius as a function of maximum pore radius, $r_m$, fractal dimension, $D$, and critical porosity corresponding to the critical pore radius, $\phi_c$ as:

$$r_c = r_{\mathrm{m}} \left(1-\phi_c\right)^{\frac{1}{3-D}} \tag{2.6}$$

He also defined electrical conductivity as:

$$\frac{\sigma_b}{\sigma_w} = \frac{\pi}{w}\left(\frac{r_c}{r_{\mathrm{m}}}\right)^2 \tag{2.7}$$

where $w$ is a constant representing uniform aspect ratio.

By combining **Eq. 2.5** and **2.7**, Hunt (2001) suggested to formulate permeability as:

$$k = \frac{\pi}{w}\frac{r_c^2}{c}\left(\frac{r_c}{r_{\mathrm{m}}}\right)^2 = \frac{\pi}{w}\frac{r_{\mathrm{m}}^2}{8}\left(1-\phi_c\right)^{\frac{4}{3-D}} \tag{2.8}$$

In similar form, Daigle (2016) expressed critical pore-throat size as:

$$r_c = r_{\mathrm{m}}\left(1-\frac{\phi}{\beta}p_c\right)^{\frac{1}{3-D}} \tag{2.9}$$

where $\phi$ is porosity, $\beta$ is the ratio of pore volume to the sum of the pore and solid volumes in the fractal model, and $p_c$ is critical percolation threshold. Alternatively, electrical conductivity has been formulized as (Ghanbarian et al., 2014):

$$\frac{\sigma_b}{\sigma_w} = \left[\frac{\phi\left(1-p_c\right)}{1-\phi p_c}\right]^2 \tag{2.10}$$

Combining **Eq. 2.8** and **2.10**, Daigle (2016) formulated permeability as:

$$k = \frac{r_{\mathrm{m}}^2}{c}\left(1-\frac{\phi}{\beta}p_c\right)^{\frac{2}{3-D}}\left[\frac{\phi\left(1-p_c\right)}{1-\phi p_c}\right]^2 \tag{2.11}$$

**Eq. 2.11** has further simplified for tight formations as (Davud Davudov and Moghanloo, 2018a):

$$k = \frac{r_{\mathrm{m}}^2}{c}\phi^m\left(1-p_c\right)^{\frac{2}{3-D}+m} \tag{2.12}$$

More recently, Ghanbarian et al. (2017) formulized critical pore radius as:

$$r_c = r_{\mathrm{m}}\left(1-\frac{\phi p_c}{\beta}\right)^{\frac{1}{3-D}} \tag{2.13}$$

where $\beta/\phi = r_m^{3-D}/(r_m^{3-D} - r_o^{3-D})$ and can be approximated as 1 in case $r_m \gg r_o$ (Ghanbarian et al. 2017). They further modified electrical conductance originally defined by KT as:

$$\frac{\sigma_b}{\sigma_w}=\frac{\phi}{3}\left[1-\left(\frac{r_c}{3r_{\mathrm{m}}}\right)^{3-D}\right]=\frac{\phi}{3}\left[1-\left(\frac{1}{3}\right)^{3-D}\left(1-\frac{\phi_c}{\beta}\right)\right] \tag{2.14}$$

Finally, by combining **Eq. 2.13** and **2.14**, Ghanbarian et al. (2017) formulated permeability as:

$$k=\frac{r_{\mathrm{m}}^2}{c}\frac{\phi}{3}\left(1-\frac{\phi_c}{\beta}\right)^{\frac{2}{3-D}}\left[1-\left(\frac{1}{3}\right)^{3-D}\left(1-\frac{\phi_c}{\beta}\right)\right] \tag{2.15}$$

## 2.2 New Critical Path Analysis Model

In this section, percolation theory is combined with Katz-Thompson (KT) model to formulate an alternative permeability model as a function of explicitly expressed hydraulic connectivity. In the KT model (**Eq. 2.4**), formulated permeability is strong function of electrical conductivity and critical pore throat radius. Using fractal and percolation theories, both parameters are substituted with equivalent terms explicitly functions of critical percolation threshold (average coordination number).

**Critical pore throat radius:** Assuming probability density function of pore throat sizes, $f$ (r), follows a power law function, it can be expressed as (Skaggs 2011; Ghanbarian et al. 2017):

$$f(r)=\frac{D}{r_o^{-D}-r_m^{-D}}r^{-D-1}, \tag{2.16}$$

where $r_m$ is the maximum accessible pore throat size, $r_o$ is the minimum pore throat radius, and $D$ is the fractal dimension of the pore space.

Integrating **Eq. 2.16**, porosity, $\phi$ can be expressed as (Ghanbarian et al. 2017):

$$\phi=\int_{r_o}^{r_m}sf(r)r^3dr=s\frac{D}{r_o^{-D}-r_m^{-D}}\frac{r_m^{3-D}-r_o^{3-D}}{3-D}, \tag{2.17}$$

where $s$ is shape factor. Similarly, critical porosity, $\phi_c$ corresponding to critical percolation threshold, $p_c$ can be expressed as:

$$\phi_c = \phi p_c = \int_{r_c}^{r_m} sf(r)r^3 dr = s\frac{D}{r_o^{-D} - r_m^{-D}}\frac{r_m^{3-D} - r_c^{3-D}}{3-D}, \quad (2.18)$$

Combining **Eq. 2.17** and **2.18**, critical percolation threshold, $p_c$ can be formulized as:

$$p_c = \frac{r_m^{3-D} - r_c^{3-D}}{r_m^{3-D} - r_o^{3-D}} = \frac{\beta}{\phi}\left[1 - \left(\frac{r_c}{r_m}\right)^{3-D}\right] \quad (2.19)$$

where$\frac{\beta}{\phi}$ is $\frac{r_m^{3-D}}{r_m^{3-D} - r_o^{3-D}}$. Rearranging **Eq. 2.19**, critical pore throat size, $r_c$ can be written as follow:

$$r_c = r_m\left(1 - \frac{\phi}{\beta}p_c\right)^{\frac{1}{3-D}}, \quad (2.20)$$

**Electrical conductivity:** Following Kirkpatrick (1979), Katz and Thompson (1987) defined electrical conductivity as:

$$\frac{\sigma_b}{\sigma_w} = \phi[p(r_e) - p_c]^t, \quad (2.21)$$

where $p(r_e)$ is the probability of a given pore throat radius to be equal or greater than $r_e$ and $t$ is universal constant equal to 2 (Sahimi 1995). However, in several studies it has been shown that, best correlation for the entire electrical conductivity can be expressed as (Bernabé and Bruderer, 1998; Montaron, 2009; Zhou et al., 1997):

$$\frac{\sigma_b}{\sigma_w} \propto \left[\frac{p - p_c}{1 - p_c}\right]^t, \quad (2.22)$$

Thus, instead of **Eq. 2.21**, electrical conductivity can be formulated as:

$$\frac{\sigma_b}{\sigma_w} = \phi\left[\frac{p(r_e) - p_c}{1 - p_c}\right]^t, \quad (2.23)$$

Following the same methodology from **Eq. 2.19**, $p(r_e)$ can be easily defined as a function of corresponding pore throat radius:

$$p(r_e) = \frac{\beta}{\phi}\left[1 - \left(\frac{r_e}{r_m}\right)^{3-D}\right] = \frac{\beta}{\phi}\left[1 - \left(\frac{r_e}{r_c}\frac{r_c}{r_m}\right)^{3-D}\right] \quad (2.24)$$

**Eq. 2.19** and **2.24** can be plugged into **Eq. 2.23** and after some rearrangement, electrical conductance can be written as:

$$\frac{\sigma_b}{\sigma_w} = \phi \left[ \frac{\left(\frac{r_c}{r_m}\right)^{3-D}\left(1-\left(\frac{r_e}{r_c}\right)^{3-D}\right)}{\frac{\phi}{\beta}-1+\left(\frac{r_c}{r_m}\right)^{3-D}} \right]^t, \tag{2.25}$$

Finally, combining **Eq. 2.4** and **2.25**, permeability can be estimated as:

$$k = \frac{r_c^2}{c}\phi \left[ \frac{\left(\frac{r_c}{r_m}\right)^{3-D}\left(1-\left(\frac{r_e}{r_c}\right)^{3-D}\right)}{\frac{\phi}{\beta}-1+\left(\frac{r_c}{r_m}\right)^{3-D}} \right]^t, \tag{2.26}$$

Further assuming $\frac{r_e}{r_c} = \frac{1}{1+t}$ (Katz and Thompson 1986), **Eq. 2.26** can be written as:

$$k = \frac{r_c^2}{c}\phi \left[ \frac{\left(\frac{r_c}{r_m}\right)^{3-D}\left(1-\left(\frac{1}{1+t}\right)^{3-D}\right)}{\frac{\phi}{\beta}-1+\left(\frac{r_c}{r_m}\right)^{3-D}} \right]^t, \tag{2.27}$$

When $r_m \gg r_o$, then $\frac{\phi}{\beta} \approx 1$ (Ghanbarian et al 2017) and **Eq. 2.27** can be simplified as:

$$k = \frac{r_c^2}{c}\phi \left[ 1-\left(\frac{1}{1+t}\right)^{3-D} \right]^t, \tag{2.28}$$

In case **Eq. 2.21** is used to formularize electrical conductivity instead of **Eq. 2.23**, then permeability can be alternatively expressed as:

$$k = \frac{r_c^2}{c}\phi \left[ (1-p_c)\left(1-\left(\frac{1}{1+t}\right)^{3-D}\right) \right]^t, \tag{2.29}$$

Please note that critical pore throat radius appears in all CPA-based permeability models discussed in this chapter is described using a similar formulation originated by Hunt (2001); the contribution of this work lies upon a different formulation for electrical conductivity term compared to the existing models.

## 2.3 Evaluation of Permeability Models

Previously discussed CPA-based permeability models (**Eq. 2.4, 2.8, 2.11, 2.15, and 2.28**) are evaluated and compared for two datasets: experimental data for 60 tight sandstone samples and 9

shale samples. To assess the accuracy of the models, the root mean square log-transformed error (RMSLE) is used:

$$RMSLE = \sqrt{\frac{1}{N}\sum_{1}^{N}[log(k_{meas}) - log(k_{cal})]^2} \quad (2.30)$$

*2.3.1 Results for Tight Sandstone Samples*

All discussed permeability models are evaluated using 60 tight sandstone samples from six different shale plays within the US and Argentina for which the permeability values have been experimentally measured. In these samples, porosity values range from 0.6 to 21 % and measured permeability values fall between 3E-4 – 6.4E-1 md. All permeability measurements were conducted at 70º F temperature and 800 psia confining pressure. For all samples, Klinkenberg corrected values were determined and implemented using the Jones-Owens method (Jones and Owens, 1980). All experimental data for tight sandstone samples are obtained through personal communication with Mr. Joseph Comisky. To determine parameters needed for permeability models MICP data is used. First entry pressure is determined after blank and conformance corrections and maximum pore throat radius ($r_m$) corresponding to the first entry pressure is calculated based on Washburn model (Washburn, 1921). Next, following Katz and Thompson (1986) critical pore throat radius ($r_c$) values are obtained from the point on the logarithmic-scale differential intrusion plot with the highest ordinate (**Figure 2.3)**. Finally, fractal dimension of pore space is predicted as fitting parameter to mercury saturation from **Eq. 2.31** as illustrated in **Figure 2.4** (Ghanbarian and Sahimi, 2017):

$$S_{Hg}(r) = \frac{r_m^{3-D} - r^{3-D}}{r_m^{3-D} - r_o^{3-D}} \quad (2.31)$$

All calculated parameters for tight sandstone samples are summarized in **Table 2.1.**

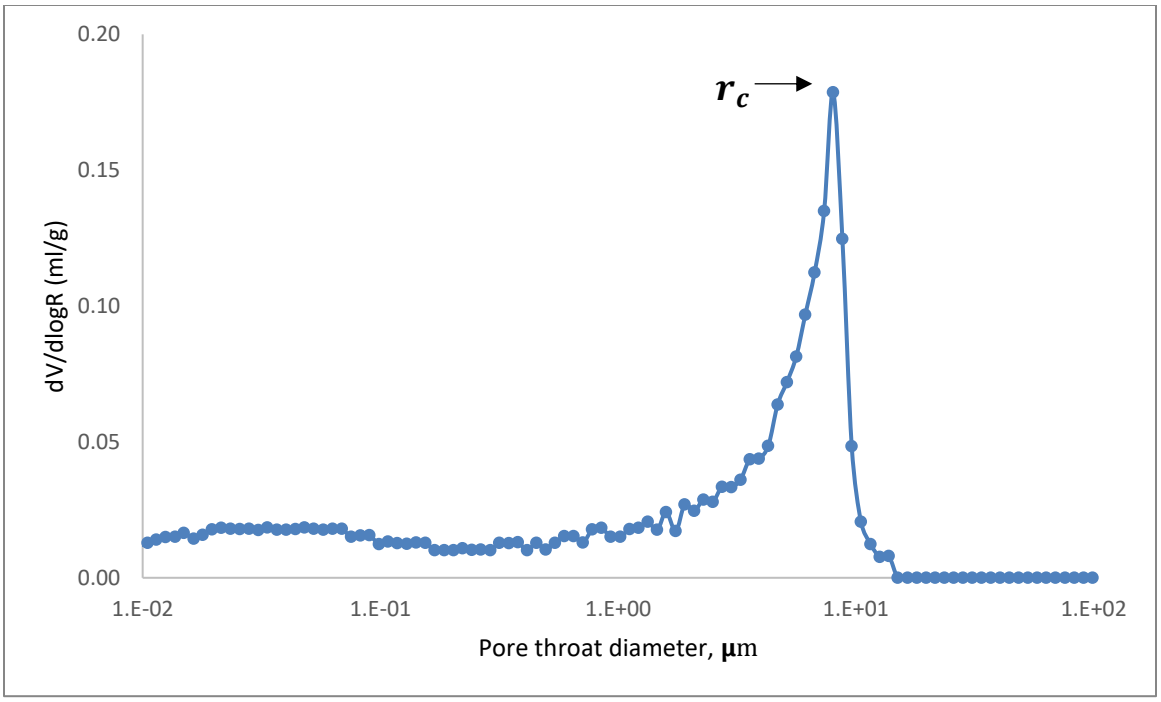


**Figure 2.3: Illustration of finding critical pore throat radius from MICP data**

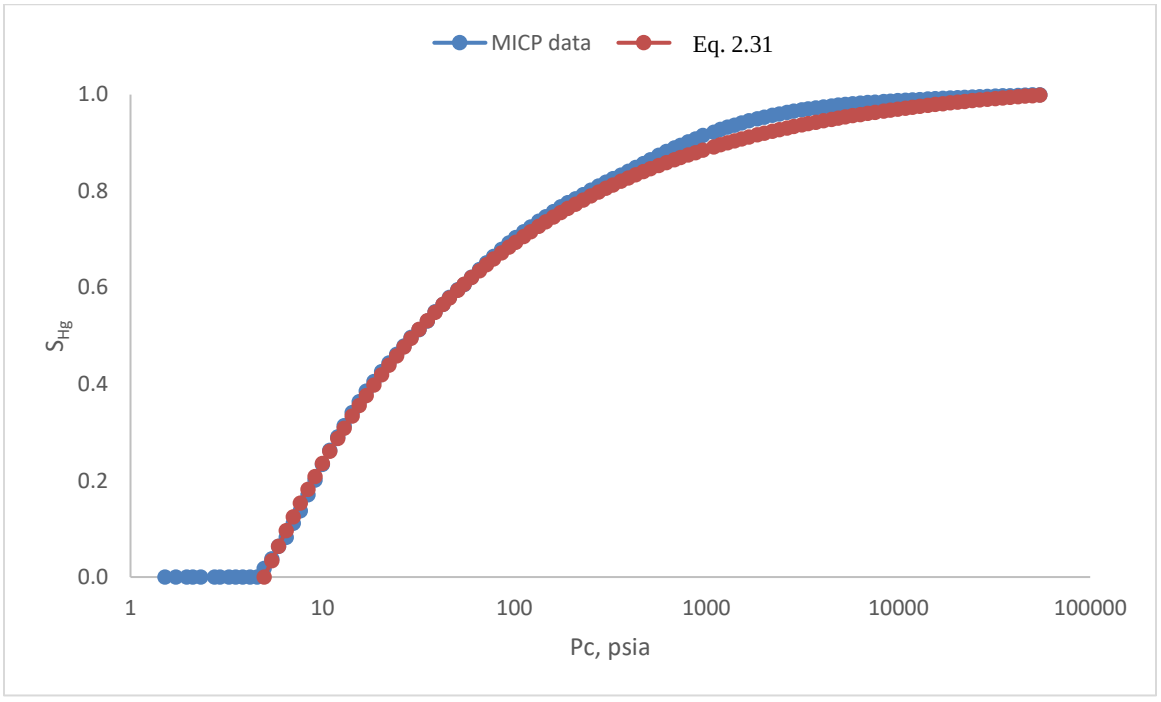


**Figure 2.4: Illustration of finding pore space fractal dimension from MICP data**

**Table 2.1: Input parameters for 60 sandstone samples**

| Sample # | $\phi$ | Measured K, md | $r_m$, µm | $r_c$, µm | $D$ |
|---|---|---|---|---|---|
| **S1** | 0.053 | 3.0E-04 | 0.07 | 0.041 | 2.18 |
| **S2** | 0.006 | 4.0E-04 | 0.10 | 0.059 | 2.00 |
| **S3** | 0.067 | 6.0E-04 | 0.07 | 0.035 | 2.24 |
| **S4** | 0.010 | 7.0E-04 | 0.16 | 0.071 | 2.49 |
| **S5** | 0.008 | 8.0E-04 | 0.13 | 0.077 | 2.47 |
| **S6** | 0.017 | 9.0E-04 | 0.21 | 0.045 | 2.04 |
| **S7** | 0.075 | 1.0E-03 | 0.07 | 0.024 | 2.27 |
| **S8** | 0.071 | 1.2E-03 | 0.23 | 0.112 | 2.37 |
| **S9** | 0.015 | 1.4E-03 | 0.13 | 0.054 | 2.03 |
| **S10** | 0.064 | 1.4E-03 | 0.08 | 0.038 | 2.28 |
| **S11** | 0.085 | 1.5E-03 | 0.18 | 0.059 | 2.46 |
| **S12** | 0.021 | 1.8E-03 | 0.19 | 0.077 | 2.17 |
| **S13** | 0.008 | 2.0E-03 | 0.23 | 0.111 | 2.47 |
| **S14** | 0.071 | 2.0E-03 | 0.16 | 0.045 | 2.41 |
| **S15** | 0.058 | 2.5E-03 | 0.10 | 0.078 | 2.29 |
| **S16** | 0.074 | 3.0E-03 | 0.23 | 0.123 | 2.46 |
| **S17** | 0.032 | 3.2E-03 | 0.36 | 0.121 | 2.35 |
| **S18** | 0.101 | 3.2E-03 | 0.19 | 0.071 | 2.51 |
| **S19** | 0.070 | 4.1E-03 | 0.19 | 0.085 | 2.43 |
| **S20** | 0.086 | 5.0E-03 | 0.30 | 0.148 | 2.46 |
| **S21** | 0.064 | 6.0E-03 | 0.21 | 0.077 | 2.42 |
| **S22** | 0.051 | 6.0E-03 | 0.33 | 0.158 | 2.43 |
| **S23** | 0.052 | 6.1E-03 | 0.13 | 0.077 | 2.31 |
| **S24** | 0.072 | 7.0E-03 | 0.37 | 0.177 | 2.44 |
| **S25** | 0.078 | 7.0E-03 | 0.25 | 0.132 | 2.48 |
| **S26** | 0.094 | 9.0E-03 | 0.43 | 0.194 | 2.51 |
| **S27** | 0.065 | 9.0E-03 | 0.28 | 0.136 | 2.39 |
| **S28** | 0.078 | 9.5E-03 | 0.33 | 0.160 | 2.51 |
| **S29** | 0.075 | 1.1E-02 | 0.52 | 0.195 | 2.48 |
| **S30** | 0.096 | 1.3E-02 | 0.52 | 0.255 | 2.56 |
| **S31** | 0.083 | 1.3E-02 | 0.73 | 0.227 | 2.59 |
| **S32** | 0.084 | 1.4E-02 | 0.52 | 0.233 | 2.50 |
| **S33** | 0.086 | 1.6E-02 | 0.36 | 0.208 | 2.54 |
| **S34** | 0.104 | 1.8E-02 | 0.39 | 0.173 | 2.58 |
| **S35** | 0.091 | 1.8E-02 | 0.63 | 0.279 | 2.53 |
| **S36** | 0.083 | 1.8E-02 | 0.57 | 0.278 | 2.51 |
| **S37** | 0.080 | 1.8E-02 | 0.33 | 0.145 | 2.51 |
| **S38** | 0.082 | 1.9E-02 | 0.47 | 0.189 | 2.55 |
| **S39** | 0.099 | 2.0E-02 | 0.35 | 0.208 | 2.56 |
| **S40** | 0.085 | 2.1E-02 | 0.69 | 0.305 | 2.49 |
| **S42** | 0.095 | 2.2E-02 | 0.36 | 0.100 | 2.56 |

| | | | | | |
|---|---|---|---|---|---|
| **S42** | 0.090 | 2.5E-02 | 1.07 | 0.178 | 2.58 |
| **S43** | 0.094 | 2.6E-02 | 0.61 | 0.325 | 2.59 |
| **S44** | 0.086 | 2.6E-02 | 0.63 | 0.177 | 2.54 |
| **S45** | 0.085 | 2.8E-02 | 0.51 | 0.271 | 2.56 |
| **S46** | 0.092 | 3.0E-02 | 1.17 | 0.304 | 2.59 |
| **S47** | 0.098 | 3.6E-02 | 0.56 | 0.325 | 2.59 |
| **S48** | 0.109 | 3.9E-02 | 0.35 | 0.271 | 2.58 |
| **S49** | 0.094 | 4.0E-02 | 1.28 | 0.334 | 2.59 |
| **S50** | 0.151 | 4.6E-02 | 0.42 | 0.189 | 2.65 |
| **S51** | 0.066 | 4.7E-02 | 0.52 | 0.306 | 2.52 |
| **S52** | 0.109 | 6.1E-02 | 1.37 | 0.510 | 2.67 |
| **S53** | 0.118 | 1.7E-01 | 2.56 | 1.367 | 2.71 |
| **S54** | 0.080 | 1.8E-01 | 0.87 | 0.667 | 2.59 |
| **S55** | 0.160 | 1.8E-01 | 0.73 | 0.356 | 2.70 |
| **S56** | 0.122 | 1.9E-01 | 1.50 | 1.046 | 2.69 |
| **S57** | 0.083 | 2.0E-01 | 1.49 | 0.721 | 2.62 |
| **S58** | 0.156 | 2.2E-01 | 0.52 | 0.364 | 2.67 |
| **S59** | 0.210 | 6.0E-01 | 0.68 | 0.525 | 2.74 |
| **S60** | 0.134 | 6.4E-01 | 2.14 | 1.496 | 2.72 |

When CPA-based permeability models are compared with experimentally measured permeability values for tight sandstone samples, for KT model (**Eq. 2.4**) the RMSLE to achieve through around 0.53 (**Figure 2.5a**) and best result for Hunt model (**Eq. 2.8**) is achieved for *w* value of 89 and *c* being 8 with RMSLE of 0.49 (**Figure 2.5b**). Daigle model (**Eq. 2.12**) manifests the minimum error with RMSLE = 0.46 (**Figure 2.5c**) with constant c being 56.5 and t being considered as 1.2. Ghanbarian (**Eq. 2.15**) and proposed models (**Eq. 2.28**) yield the most accurate predictions with RMSLE ~ 0.32 (**Figure 2.5d and e**). Overall results suggest that, CPA-based models are accurate enough for permeability estimation from tight sandstone samples. Out of 60 samples studied around 6 to 8 of them falls outside range of factor of three boundary lines (three times greater or smaller) based on results calculated from **Eq. 2.15 and 2.28**.

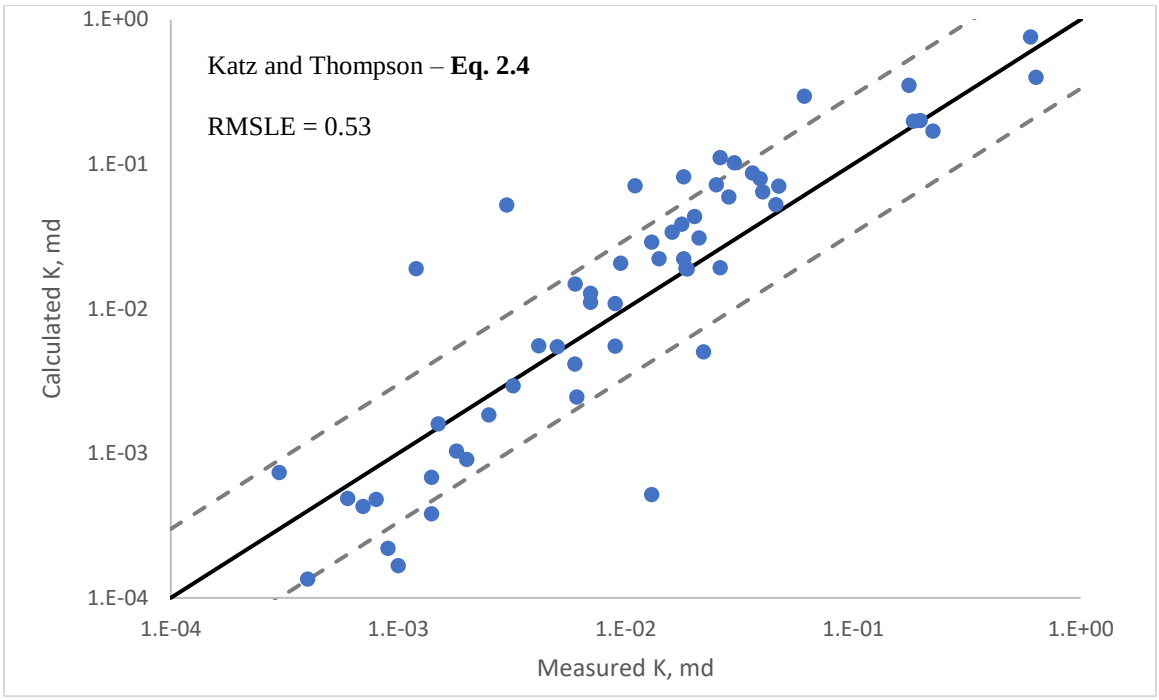
Katz and Thompson – **Eq. 2.4**
RMSLE = 0.53
Calculated K, md
Measured K, md
1.E+00
1.E-01
1.E-02
1.E-03
1.E-04
1.E-04
1.E-03
1.E-02
1.E-01
1.E+00

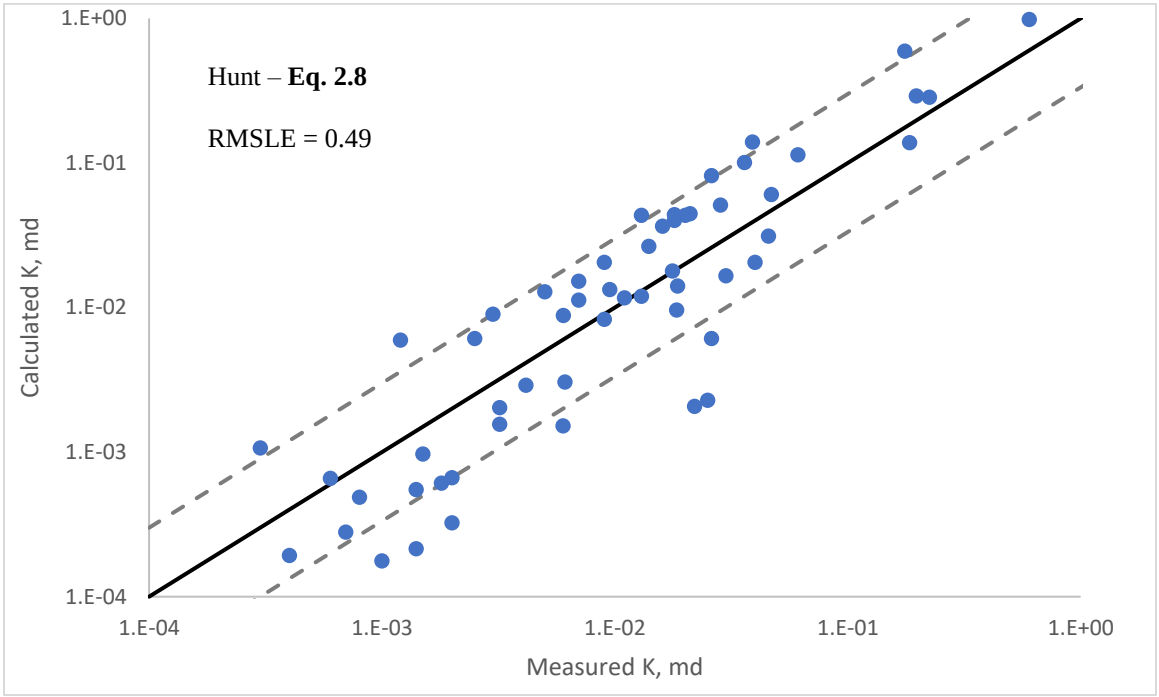
Hunt – **Eq. 2.8**
RMSLE = 0.49
Calculated K, md
Measured K, md
1.E+00
1.E-01
1.E-02
1.E-03
1.E-04
1.E-04
1.E-03
1.E-02
1.E-01
1.E+00

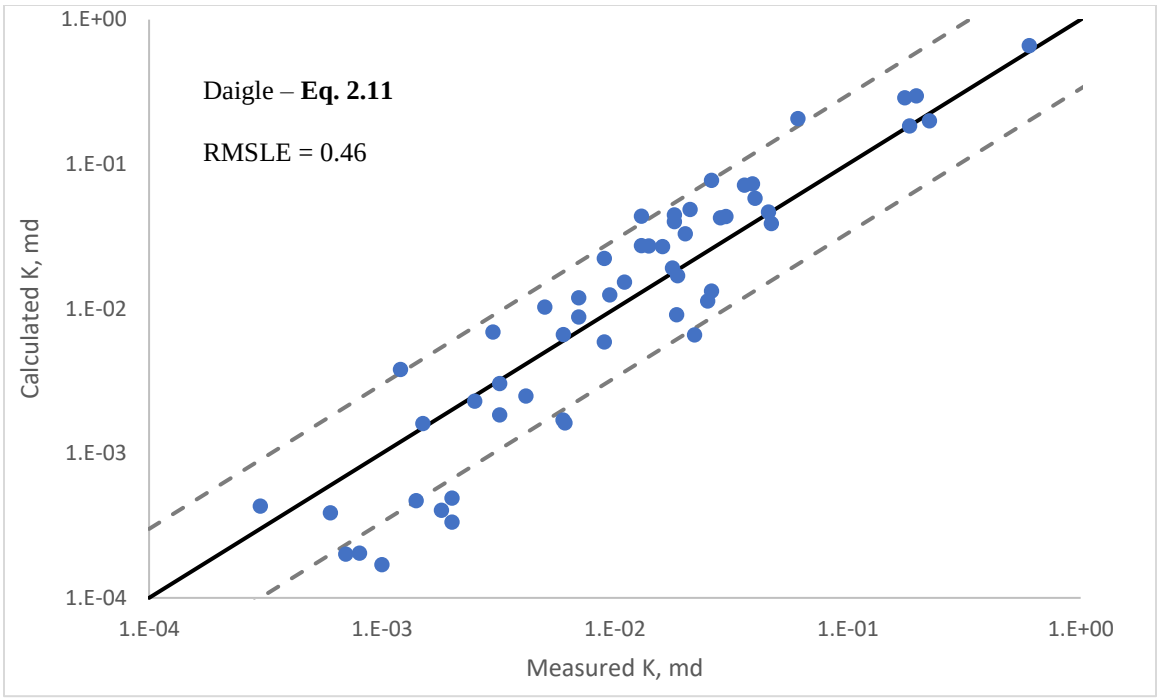
Daigle – **Eq. 2.11**
RMSLE = 0.46
Calculated K, md
Measured K, md
1.E+00
1.E-01
1.E-02
1.E-03
1.E-04
1.E-04
1.E-03
1.E-02
1.E-01
1.E+00

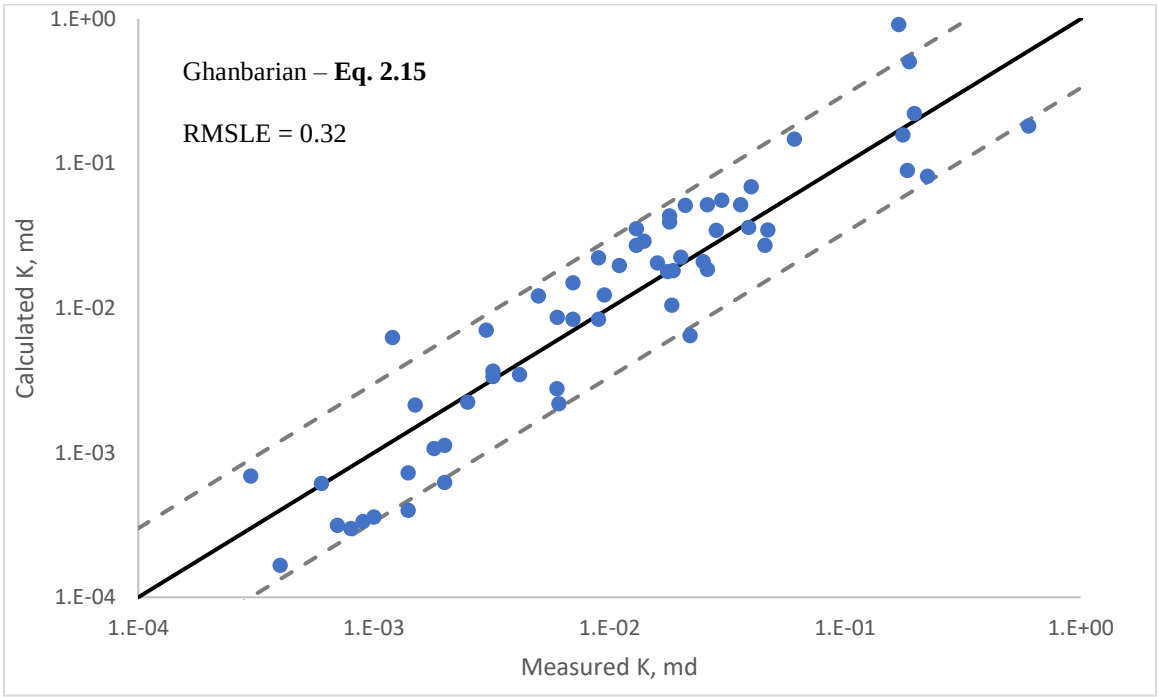
Ghanbarian – **Eq. 2.15**
RMSLE = 0.32
Calculated K, md
Measured K, md
1.E+00
1.E-01
1.E-02
1.E-03
1.E-04
1.E-04
1.E-03
1.E-02
1.E-01
1.E+00

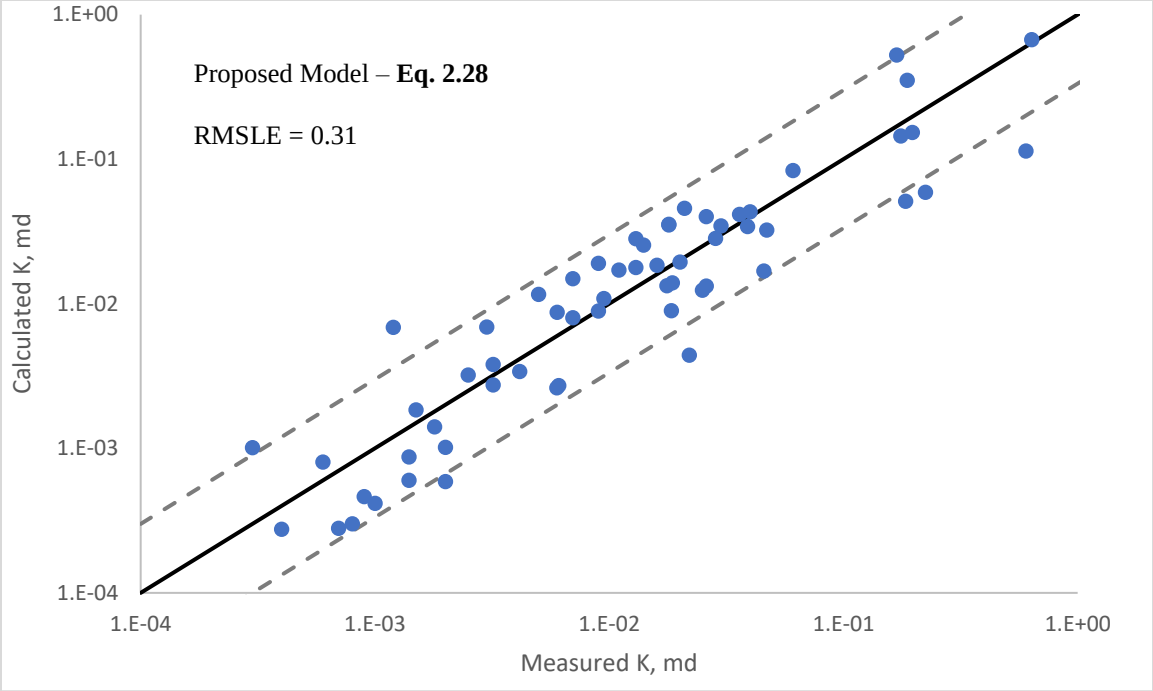


**Figure 2.5: Comparison of calculated and measured permeability values (comparative plots) for tight sandstone samples (Solid and dashed line represents 1:1 and factor of three boundary lines respectively).**

### *2.3.2 Results for Shale Samples*

Similarly, for the 16 shale samples studied all permeability models are evaluated and compared with experimental measurements. In these samples, porosity values range from 1.5 to 8 % and measured permeability values fall between 2.1E-3 – 1.7E-5 md. All permeability measurements were conducted using nitrogen gas under confining pressure ranging between 3000 – 6000 psi. The permeability measurement for all shale samples has been conducted by Unconventional Shale Gas Consortium at the University of Oklahoma.

Following the same procedure, parameters needed for permeability models are determined from MICP data. In addition to blank and conformance corrections, also compression correction has been considered for shale samples (Bailey, 2009; Lan et al., 2017) and maximum pore throat radius

($r_m$) is calculated based on Washburn (1921) equation. Critical pore throat radius ($r_c$) values are obtained from the point on the logarithmic-scale differential intrusion plot with the highest ordinate. However, for 2 samples peak point has not been reached and for 5 samples experimental error have been observed thus are excluded from calculations. Finally, fractal dimension of pore space is predicted as fitting parameter to mercury saturation from **Eq. 2.31**. All calculated parameters for tight sandstone samples are summarized in **Table 2.2.**

**Table 2.2: Input parameters for 10 shale samples**

| Sample # | $\phi$ | Measured K, md | $r_m$, µm | $r_c$, µm | $D$ |
|---|---|---|---|---|---|
| **S1** | 0.05 | 1.70E-05 | 5.4E-03 | 3.2E-03 | 2.50 |
| **S2** | 0.07 | 6.30E-05 | 7.6E-03 | 3.2E-03 | 2.40 |
| **S3** | 0.01 | 1.04E-04 | 3.8E-02 | 1.2E-02 | 2.23 |
| **S4** | 0.05 | 1.27E-04 | 1.0E-02 | 2.7E-03 | 2.05 |
| **S5** | 0.05 | 1.38E-04 | 8.1E-03 | 2.7E-03 | 2.21 |
| **S6** | 0.06 | 2.89E-04 | 2.9E-02 | 1.0E-02 | 2.00 |
| **S7** | 0.06 | 6.31E-04 | 7.6E-03 | 3.6E-03 | 2.31 |
| **S8** | 0.07 | 1.29E-03 | 4.8E-02 | 7.2E-03 | 2.59 |
| **S9** | 0.08 | 1.72E-03 | 1.3E-02 | 5.4E-03 | 2.38 |

When CPA-based permeability models are evaluated for shale samples, for KT model (**Eq. 2.4**) RMSLE is around 0.72 (**Figure 2.6a**) and best result for Hunt model (**Eq. 2.8**) is achieved for *w* value of 2 and *c* being 8 with RMSLE = 0.82 (**Figure 2.6b**). For Daigle model (**Eq. 2.11**) the minimum RMSLE of 0.51 can be achieved when constant $c$ is considered 32.5 and when parameter, $t$ replaced with 1.3 instead of original value of 2 (**Figure 2.6c**). If exponent 2 is used in calculations that RMSLE will be as high as 2.78 (not shown as figure). For Ghanbarian model (**Eq. 2.15**) RMSLE is calculated as 0.54 with c being 3 (**Figure 2.6d**) and proposed model (**Eq. 2.28**) yield one of the most accurate predictions with RMSLE ~ 0.54 (**Figure 2.6e**) with $t$ being 1.75.

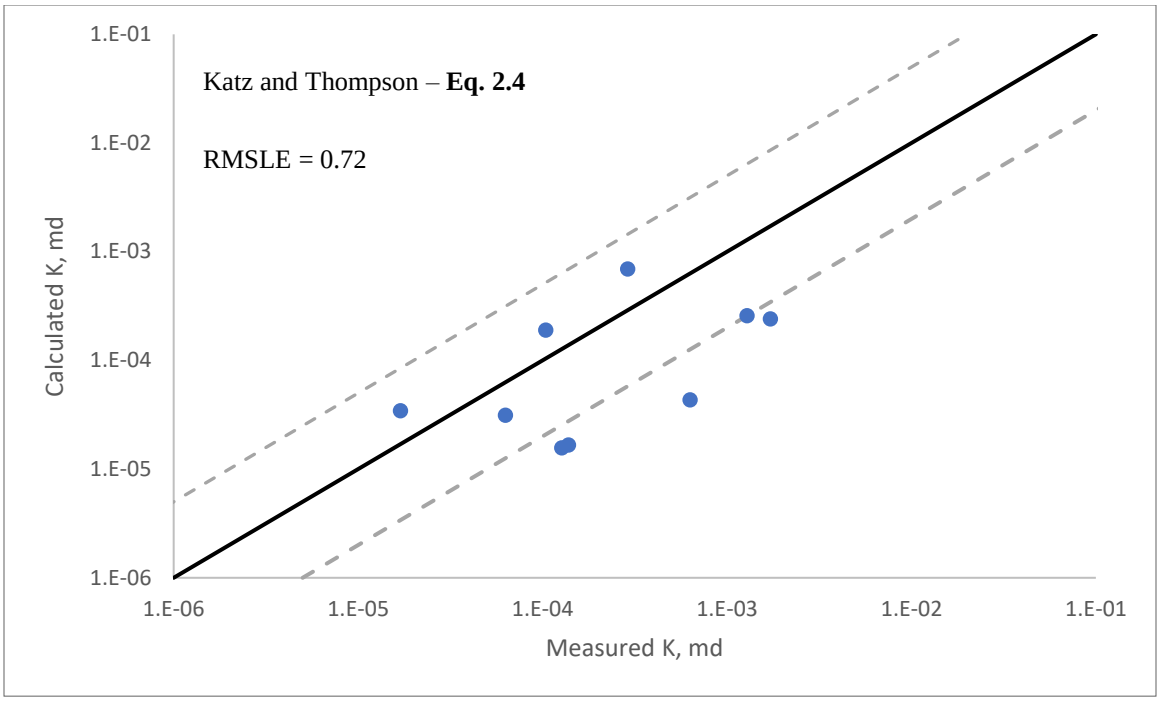
Katz and Thompson – **Eq. 2.4**
RMSLE = 0.72
Calculated K, md
Measured K, md
1.E-01
1.E-02
1.E-03
1.E-04
1.E-05
1.E-06

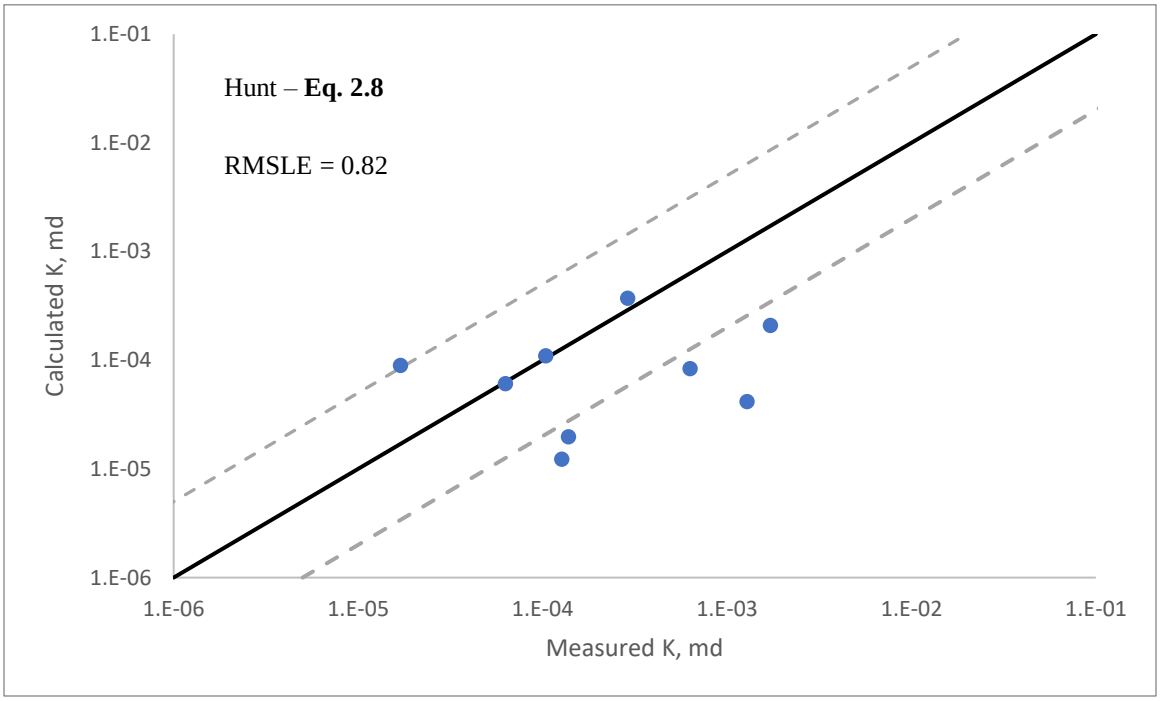
Hunt – **Eq. 2.8**
RMSLE = 0.82
Calculated K, md
Measured K, md
1.E-01
1.E-02
1.E-03
1.E-04
1.E-05
1.E-06

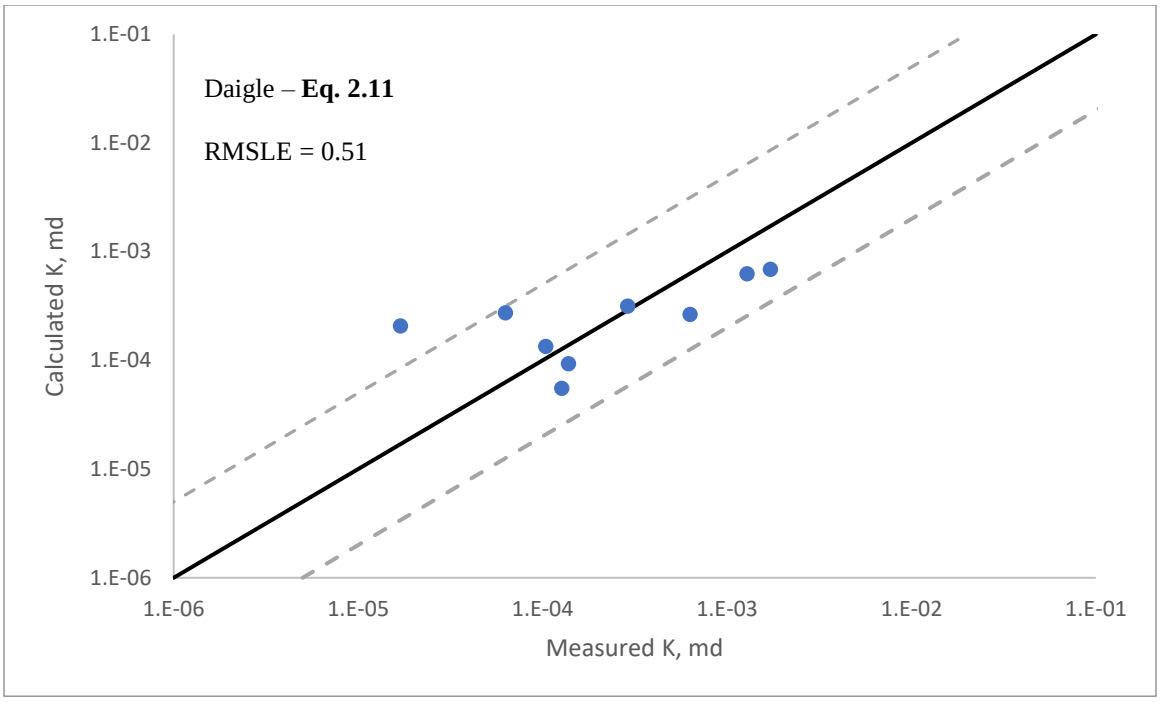
Daigle – **Eq. 2.11**
RMSLE = 0.51
Calculated K, md
Measured K, md
1.E-01
1.E-02
1.E-03
1.E-04
1.E-05
1.E-06
1.E-06
1.E-05
1.E-04
1.E-03
1.E-02
1.E-01

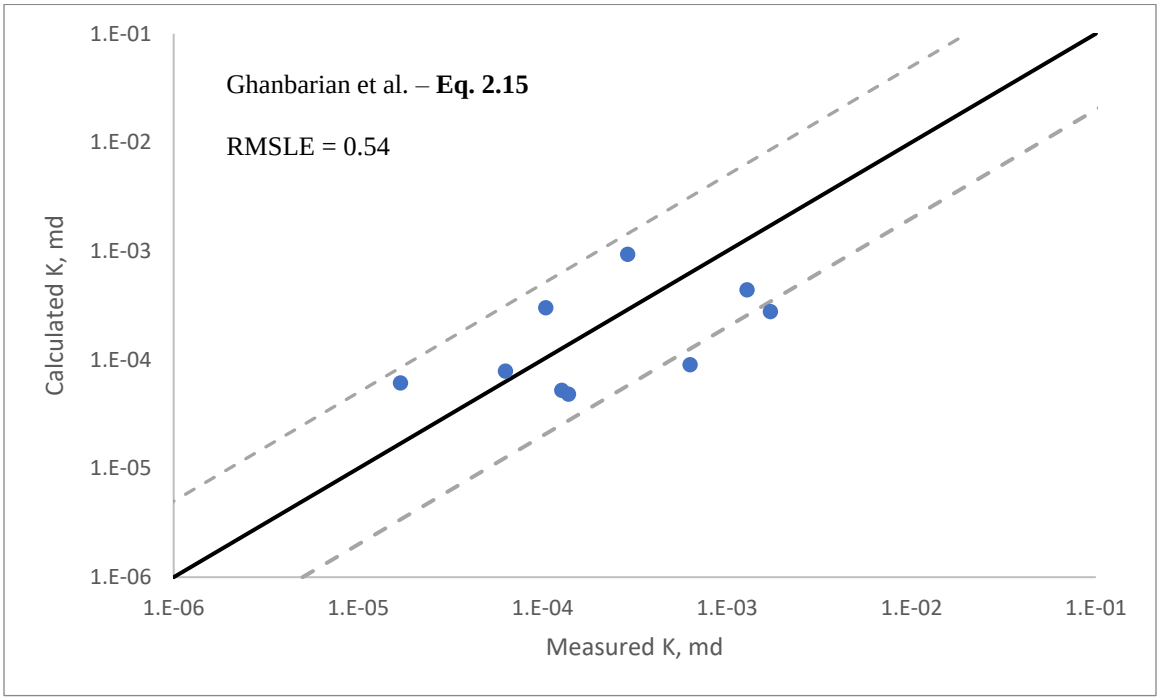
Ghanbarian et al. – **Eq. 2.15**
RMSLE = 0.54
Calculated K, md
Measured K, md
1.E-01
1.E-02
1.E-03
1.E-04
1.E-05
1.E-06
1.E-06
1.E-05
1.E-04
1.E-03
1.E-02
1.E-01

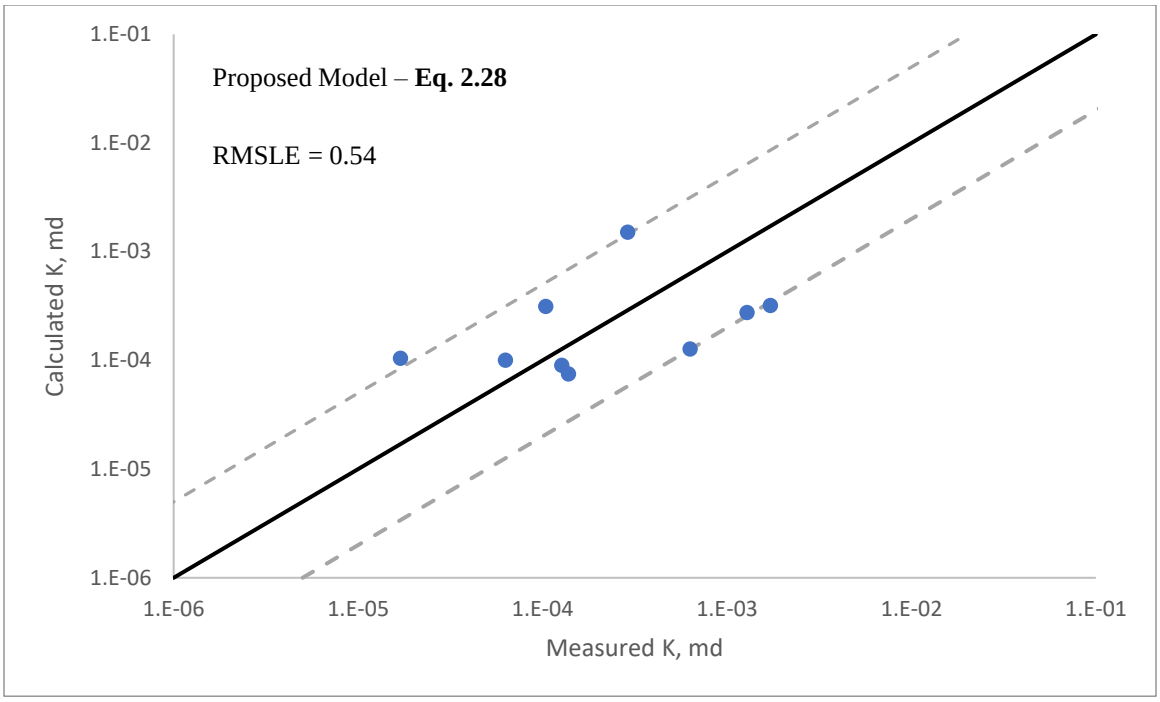


**Figure 2.6: Comparison of calculated and measured permeability values (comparative plots) for shale samples (Solid and dashed line represents 1:1 and factor of five boundary lines respectively).**

When compared with tight sandstone results, CPA-based models are less accurate for shale samples. This might be due to miscalculation of critical pore throat radius and/or maximum pore throat radius from MICP test data and/or due to higher estimation of experimental results because of micro-crack effect which will be discussed in more detail in next section.

## 2.4 Discussion

In this section, the limitations and advantages of CPA-based permeability models are discussed

### *2.4.1 Correlation Between Calculated Parameters*

Interplay among several key parameters used in CPA-based permeability models is evaluated for both set of data. **Figure 2.7a** shows maximum pore throat radius as a function of critical pore throat radius for sandstone samples; it can be observed that there is a strong correlation ($R^2 = 0.88$).

Moreover, consistent with **Eq. 2.20,** exponent in power law function is close to 1; i.e. a linear relation is deduced.

**Figure 2.7b** demonstrates measured permeability as a function of maximum pore throat radius and **Figure 2.7c** illustrates the correlation between measured permeability and critical pore throat radius. When fitted with power law function, the exponent becomes 1.85 in both cases, consistent with the universal value of exponent $t$ ($\approx 2$) used in the analytic permeability models.

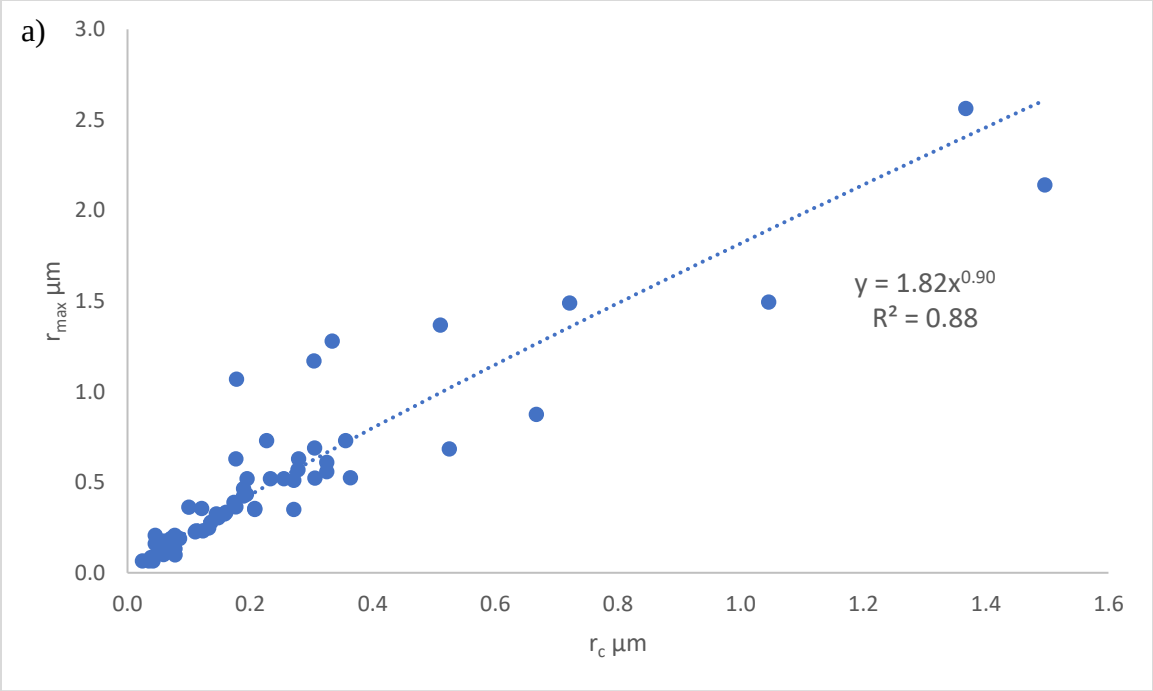

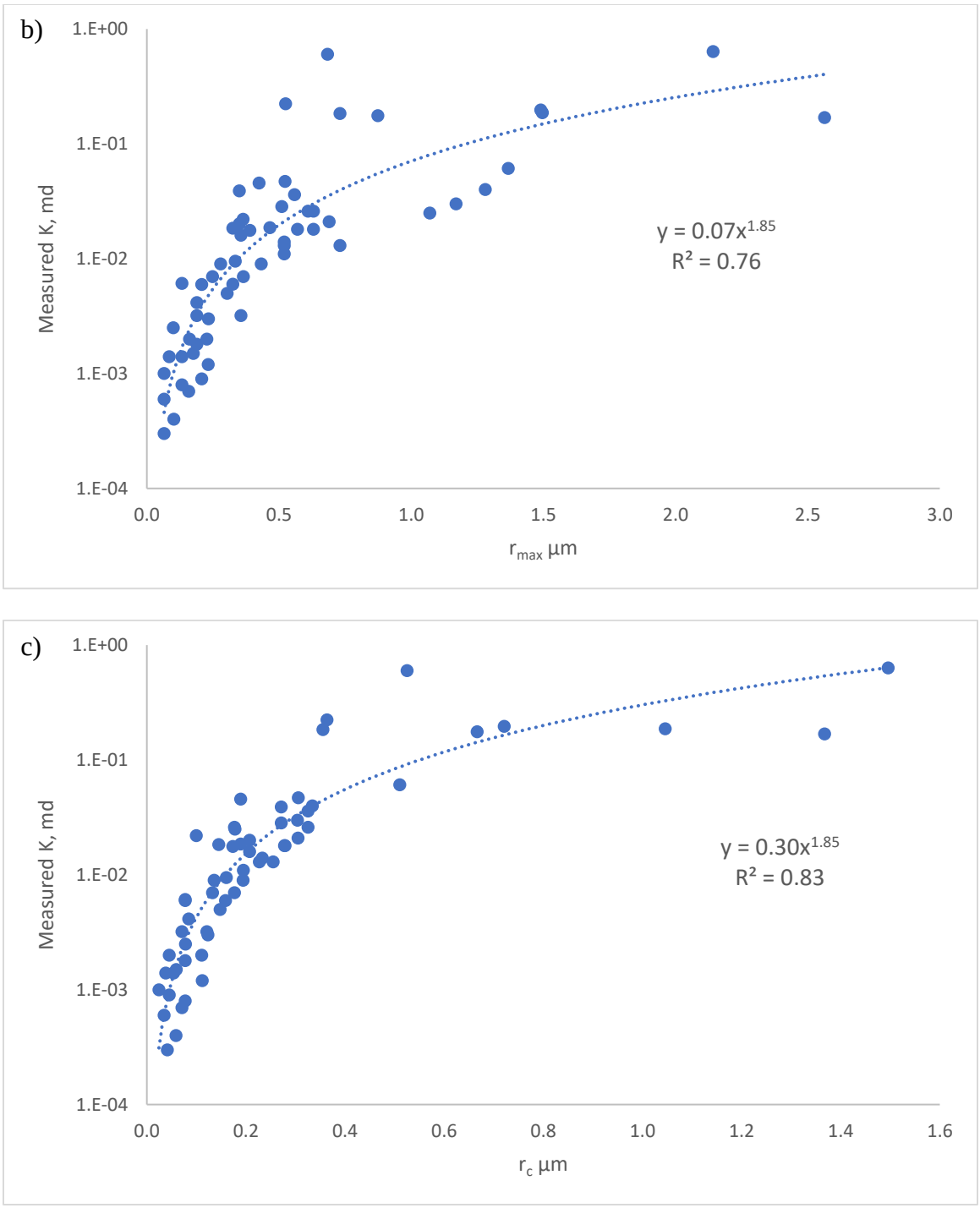


**Figure 2.7: Interplay among key parameters for sandstone samples a) Maximum pore throat radius as a function of critical pore throat radius; b) Measured permeability as a function of maximum pore throat radius; c) Measured permeability as a function of critical pore throat radius**

Similarly, for shale samples **Figure 2.8a** shows strong correlation ($R^2$ = 0.78) between maximum pore throat radius and critical pore throat radius with exponent in power law function being around 1.2.

**Figure 2.8b and c** illustrates measured permeability as a function of maximum and critical pore throat radius and after 2 outliners are excluded, power law correlation with exponent being around 1.65 and 3.38 are observed, respectively.

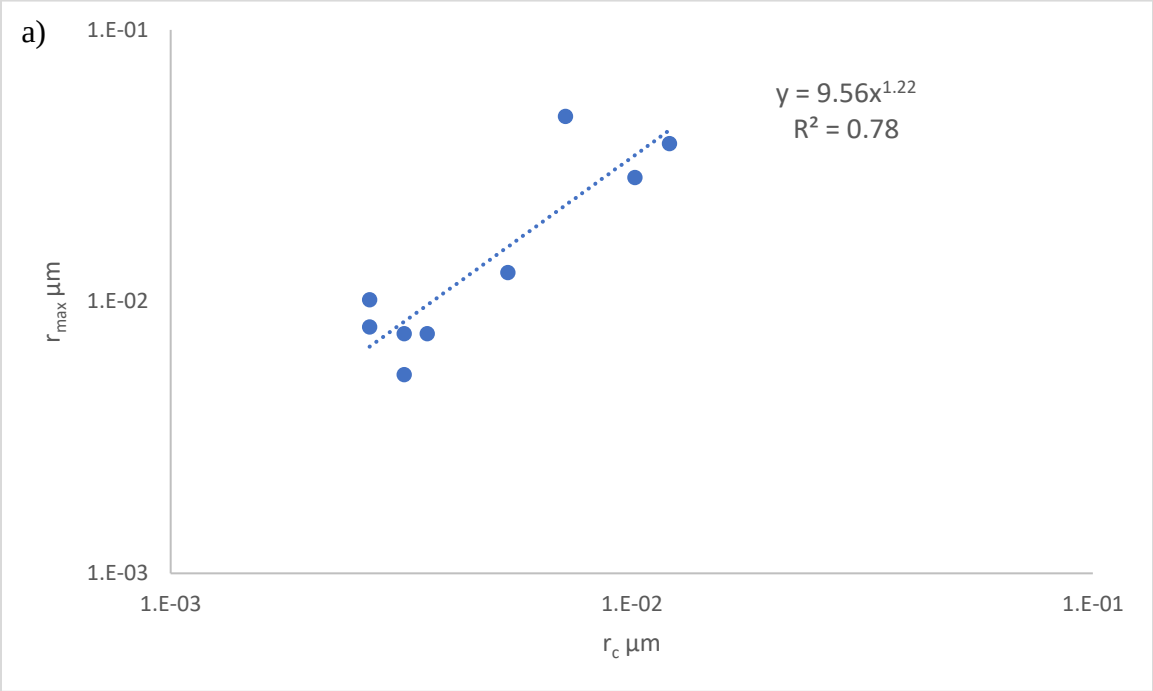

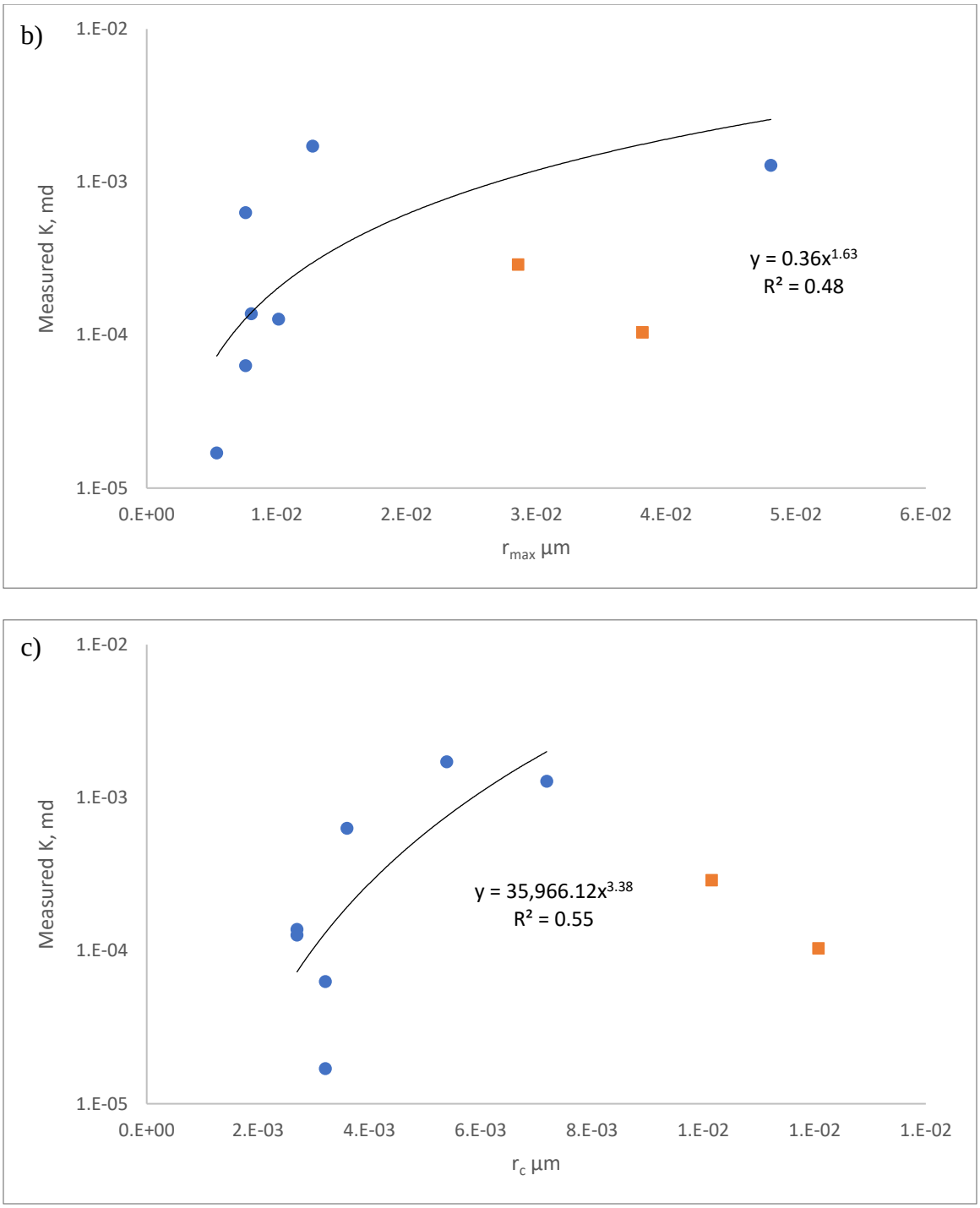


**Figure 2.8: Interplay among key parameters for shale samples a) Maximum pore throat radius as a function of critical pore throat radius; b) Measured permeability as a function of maximum pore throat radius ; c) Measured permeability as a function of critical pore throat radius**

### *2.4.2 Limitations of the CPA-based Models*

Although CPA-based permeability models can accurately predict permeability of tight formations, there are certain limitations that needs to be discussed, especially for shale formations. As it has been discussed previously, error for shale samples are higher than that of tight sandstone samples. Moreover, in most cases calculated permeability values are underestimated if critical pore throat radius, $r_c$ obtained from MICP is used for calculations. This might be due to higher estimation of experimental results because of micro-crack effect. Another possible reason for this might be due to the effect of compression stage during MICP measurements which may lead to significant pore structure change because of pore connectivity loss/collapse. Recently several experiments have been conducted to evaluate the effect of confining pressure on MICP test results (Guise et al., 2018). They have shown that, when confining pressure is applied, MICP test results might significantly shift. As illustrated in **Figure 2.9**, under 7000 psi confining pressure, critical pore throat radius reduces to 0.008 μm from base case value of 0.046 μm.

Moreover, as it has been discussed in the literature, during MICP test if pressure values are smaller than critical intrusion/entry pressure, then pressure value will not be sufficient for mercury to intrude into samples and at this stage, pores and grains are compressed owing to effective pressure (Lan et al. 2017; Bailey 2009). Thus, the confining pressure occurred during compression stage may cause to pore connectivity loss and consequently smaller critical pore throat size estimation.

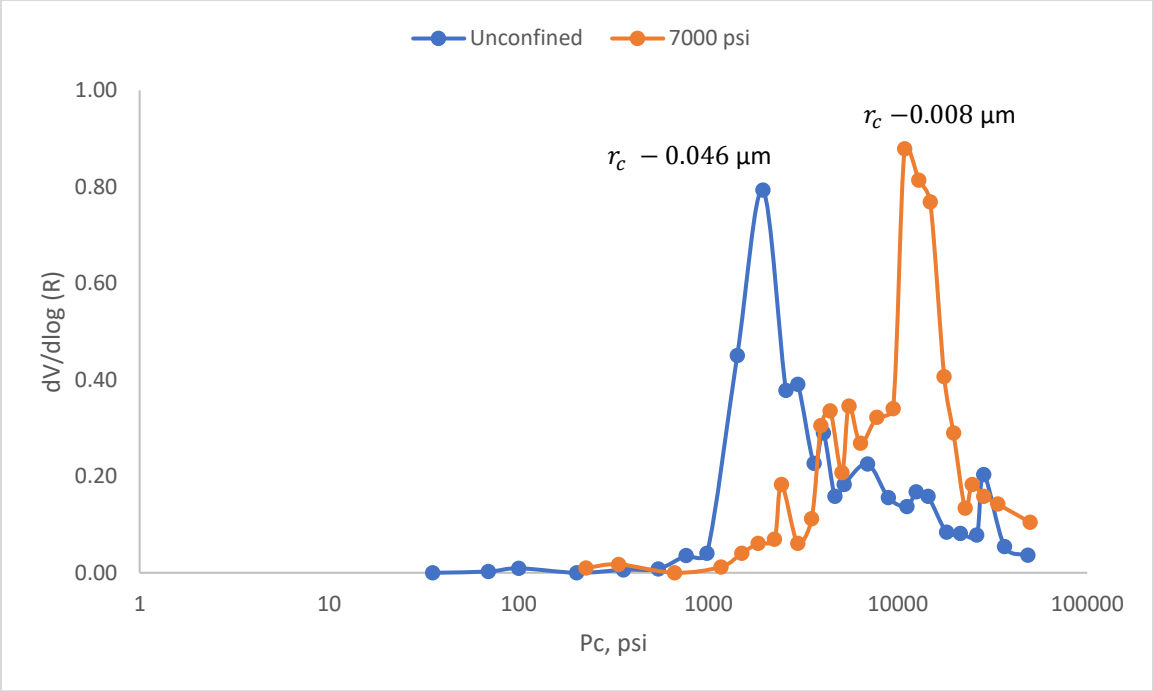


**Figure 2.9: MICP test results for unconfined and 7000 psia confining pressure cases (modified from Guise et al., 2018)**

As an alternative method, low-pressure $N_2$ adsorption/desorption experiments can be used to determine critical percolation threshold and fractal dimension (Daigle et al., 2015; Liu and Seaton, 1994; Ojha et al., 2017a, 2017c; Seaton, 1991), however it should be noted that pore size distribution obtained from adsorption data reflects the complete pore volume, not only pore throats (Daigle et al. 2015; Daigle 2016).

Another major assumption is that pore throat size distribution of samples fit power law function (**Eq. 2.16**). Although power law pore size distribution has been observed for shale samples (Curtis et al., 2010), some of the samples may not fit this assumption which might be the probable reason for the outliers in results.

### *2.4.3 Advantages of the CPA-based Models*

The major advantage of the proposed model is that the impact of interconnectivity can be easily accounted and evaluated as it explicitly appears in equations. Replacing critical pore-throat radius as a function of maximum pore-throat size from **Eq. 2.20** and further expressing percolation threshold, ($p_c$), as a function of average coordination number, ($z$), as $p_c = 1.5/z$ (Hunt et al., 2014; Sahimi, 2011), **Eq. 2.28** can be rewritten as:

$$k = \frac{r_m^2}{c}\phi\left[1-\left(\frac{1}{1+t}\right)^{3-D}\right]^t\left(\frac{z-1.5}{z}\right)^{\frac{2}{3-D}}, \tag{2.32}$$

Alternatively, based on cumulant expansion method, percolation threshold is estimated in terms of coordination number as (Hori and Yonezawa, 1977):

$$p_c = 1-\exp\left(-\frac{2}{z}\right), \tag{2.33}$$

Substituting **Eq. 2.33** into **Eq. 2.28** yields alternative form of permeability model as:

$$k = \frac{r_m^2}{c}\phi\left[1-\left(\frac{1}{1+t}\right)^{3-D}\right]^t exp\left(-\frac{\eta}{z}\right), \tag{2.34}$$

where $\eta = \dfrac{4}{3-D}$.

It is obvious from **Eq. 2.32 and 34** that $\frac{r_{max}^2}{c}\phi$ represents maximum achievable permeability and $\left(\frac{z-1.5}{z}\right)^{\frac{2}{3-D}}$ or $exp\left(-\frac{\eta}{z}\right)$ represents pore/hydraulic conductivity. By analyzing **Eq. 2.32 or 34**, the impact of connectivity can be distinguished and evaluated separately.

## 2.5 Conclusions

In this chapter, a new permeability model based on critical path analysis is developed. Critical pore throat radius and electrical conductivity used in Katz and Thompson model is revisited and

redefined. The permeability in the new model is a function of the maximum pore throat radius, porosity, fractal dimension and percolation threshold. The proposed model is compared with previously developed CPA-based permeability models and validated with experimental data for tight sandstone and shale sample. Comparing to previous model, proposed model performs the better results. The other advantage of the new model is that the impact of pore interconnectivity/hydraulic conductivity can be easily accounted and evaluated as it explicitly appears in the equation.

# Chapter 3 - Scale Dependent Connectivity of Shale Matrix

## 3.1 Introduction

This chapter addresses **Obj. 2** where impact of sample size on pore connectivity is investigated based on mercury injection capillary pressure (MICP) data. In previous studies, shale porosity based on MICP test for different particle sizes has been investigated by several researchers (Comisky et al., 2011; Tinni et al., 2014). Based on experimental results it has been concluded that mercury porosity is decreasing with increasing particle size and suggested that this is due to the effect of restricted pore connectivity. This is consisted with Hu et al., (2014) results where the concentration of injected Wood's metal significantly decreases in the middle section of the sample when compared to the edges and surfaces. In this study, MICP porosity for different sample sizes are investigated and then accessible porosity defined as fraction of pore volume that has been invaded by mercury and hydraulic connectivity based on experimental data coupled with percolation theory is analyzed (D. Davudov and Moghanloo, 2018).

To analyze accessible and interconnected porosity, samples from Barnett, and Haynesville formations with several different sizes are selected with MICP data. The sample sizes analyzed in this study is obtained after 1-inch core plug samples are crushed, and series of mesh size are used to break out several sample sizes from the same depth interval. Particles with average sizes of 25.4mm (core plug), 5.7mm, 3.5mm, 1.6mm, and 0.7mm are selected for MICP tests. The properties of the selected shale samples are summarized in **Table 3.1**. All experimental measurements used for this chapter have been conducted by Unconventional Shale Gas Consortium at the University of Oklahoma.

**Table 3.1: Summary of sample properties obtained with FTIR method.**

| *Sample* | *Quartz + Feldspars (wt %)* | *Clays (wt %)* | *Carbonates (wt %)* | *TOC (wt %)* | *Others (wt %)* |
|---|---|---|---|---|---|
| *Barnett* | 21 | 65 | 4 | 5 | 5 |
| *Haynesville* | 5 | 42 | 43 | 2 | 8 |

To evaluate fraction of accessible pore volume, ratio of porosity calculated from MICP test to absolute total porosity, ($\phi_{LPP}$) are calculated. Total porosity values are estimated from crushed sample low-pressure pycnometer (LPP) test results which all samples were obtained from the same depths as the samples used for MICP.

## 3.2 Accessible Porosity and Permeability

The basis for this study is to measure and compare accessible porosity and permeability values based on MICP test on a variety of sample sizes for Barnett and Haynesville shale samples. Next by applying percolation theory, accessible (fluid saturated) porosity, pore connectivity and permeability are evaluated as a function of sample size.

### *3.2.1 Accessible Porosity*

Pore volume values calculated based MICP test data are considered as accessible pore volume invaded with mercury ($\phi_a$), where absolute total porosity ($\phi_{LPP}$) is determined based on crushed sample LPP test and fraction of accessible porosity ($\phi_a/\phi_{LPP}$) is analyzed to determine impact of sample size on accessible porosity. The calculated LPP porosity is around 5.9% and 5.4% for Barnett and Haynesville samples, respectively. Since LPP porosity represents absolute (total) porosity, it is assumed that it will be same for all particle size (based on definition of REV). Incremental and cumulative mercury volume measured in milliliters per gram (ml/g) for all sample sizes are illustrated in **Figure 3.1 & 3.2** for both formations. As it can be seen for the both samples, as sample size increases cumulative mercury volume and porosity decreases.

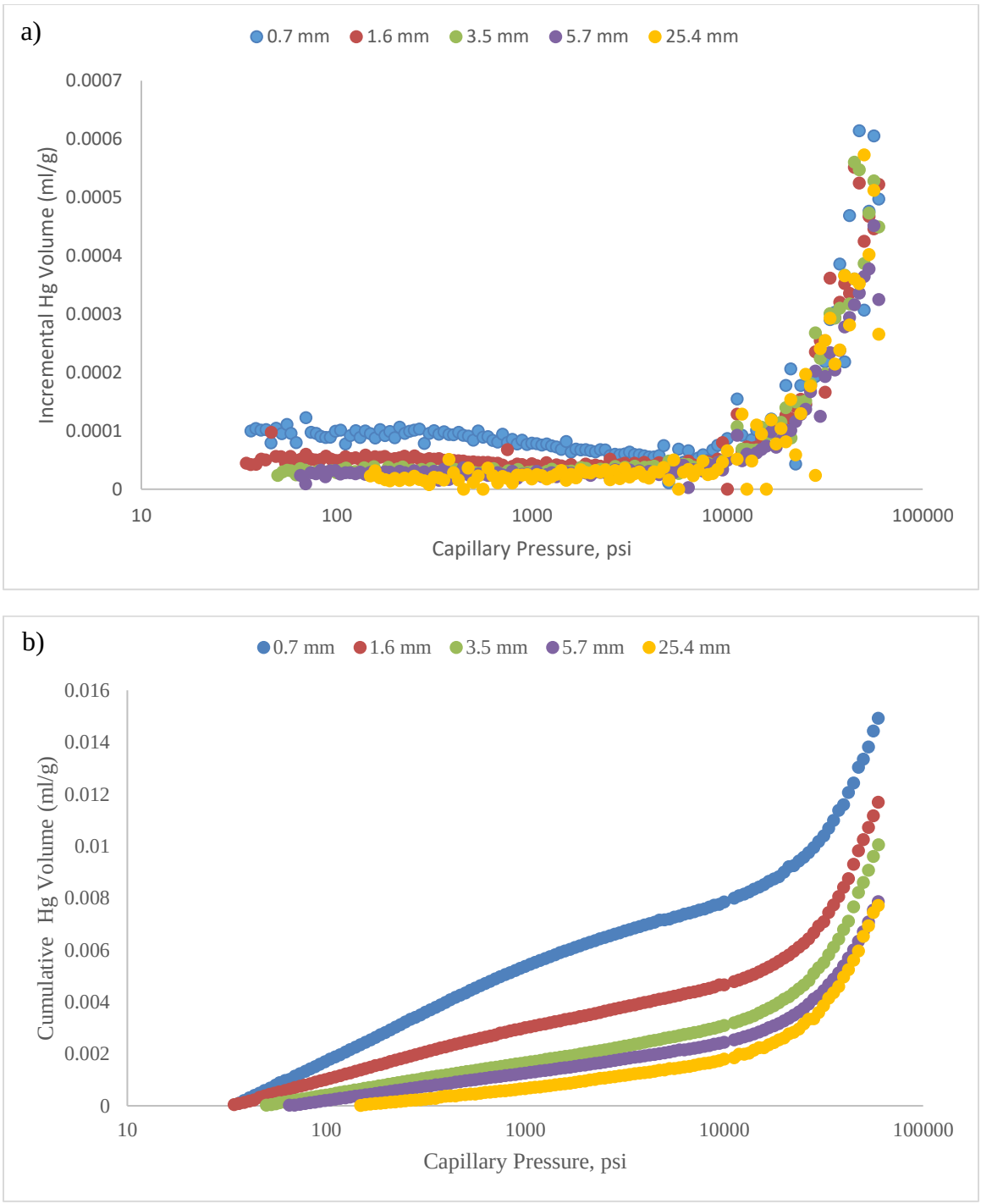


**Figure 3.1: Mercury injection capillary pressure data for Barnett samples a) Incremental volume b) Cumulative volume**

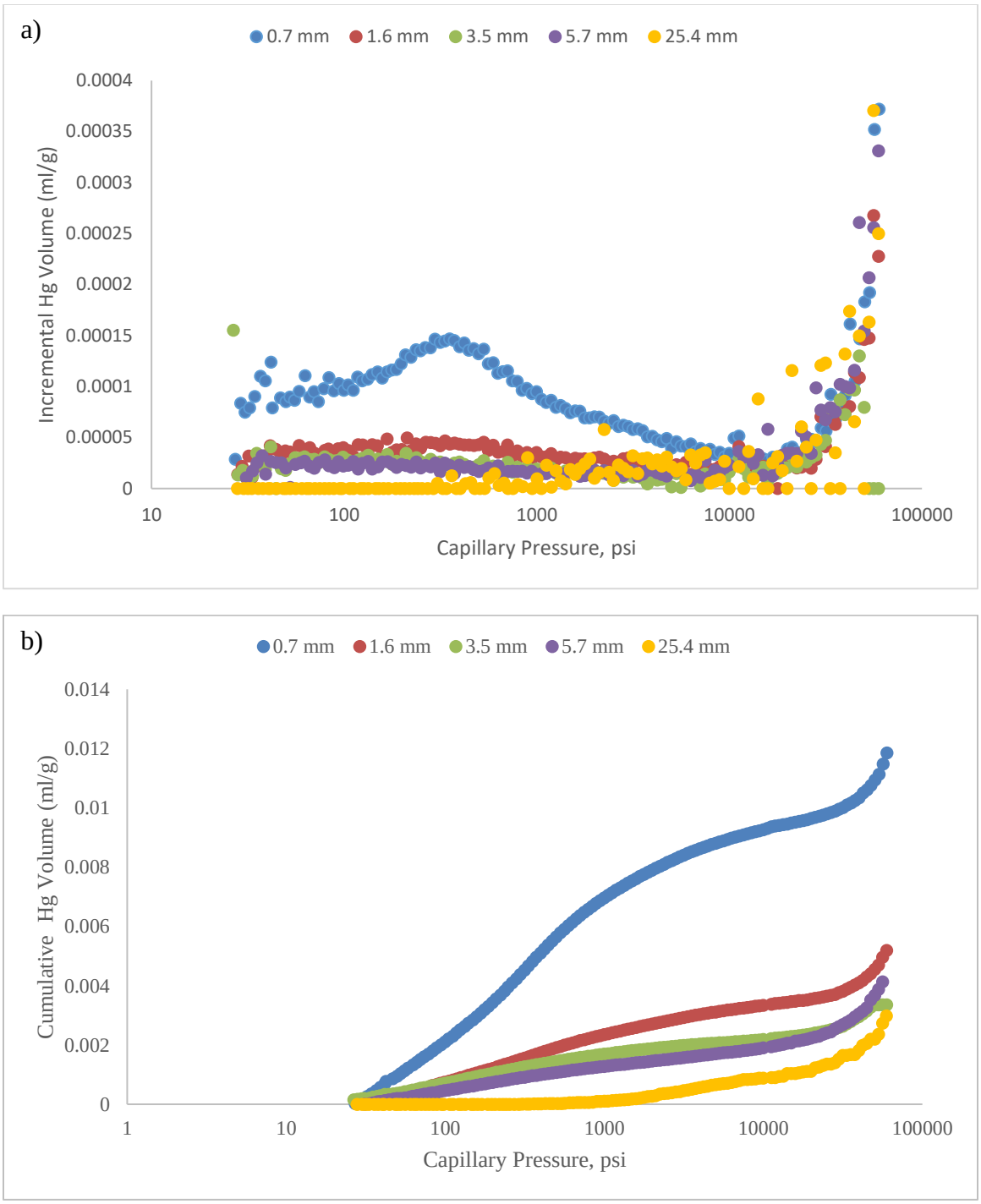


**Figure 3.2: Mercury injection capillary pressure data for Haynesville samples a) Incremental volume b) Cumulative volume**

The fraction of accessible porosity values, $(\phi_a/\phi_{LPP})$ plotted as a function of sample size is illustrated in **Figure 3.3** calculated from raw MICP data, whereas **Figure 3.4** shows results after

MICP data has been corrected considering conformance and pore compression corrections (Comisky et al., 2011; Davudov et al., 2018a). Results show a dramatic difference between porosity values measured from MICP as a function of particle size for any given sample as illustrated in **Figure 3.3 and 3.4.** It can be observed that, in all cases, accessible porosity is smallest for the core plug and largest for finest particle size range. This can be explained through diminishing of the pore connectivity as sample size increases which results in less amount of mercury gets intruded, consistent with reduction in accessible porosity for larger samples. In addition, results indicate that for all sample sizes, accessible pore fraction for Barnett is higher than Haynesville. Results suggest that around 30 % of pores are saturated and accessible in Barnett shale sample whereas this value is around 15% for Haynesville.

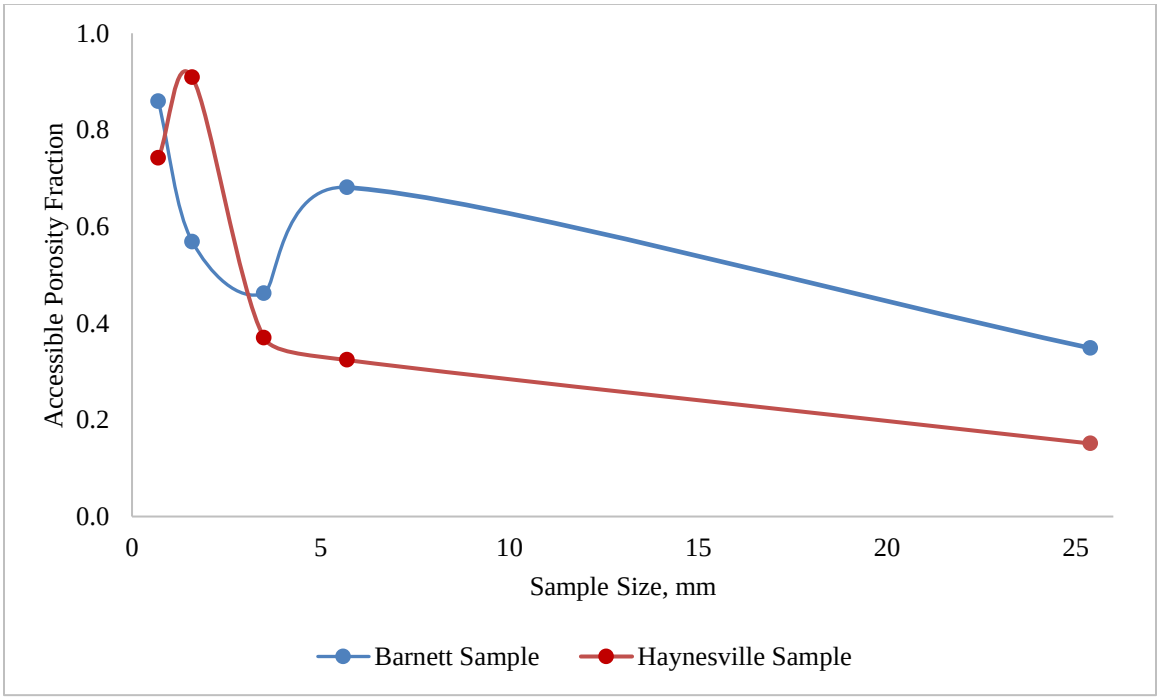


**Figure 3.3: Fraction of accessible porosity ($\phi_{MICP}/\phi_{LPP}$) as a function of sample size (without corrections)**

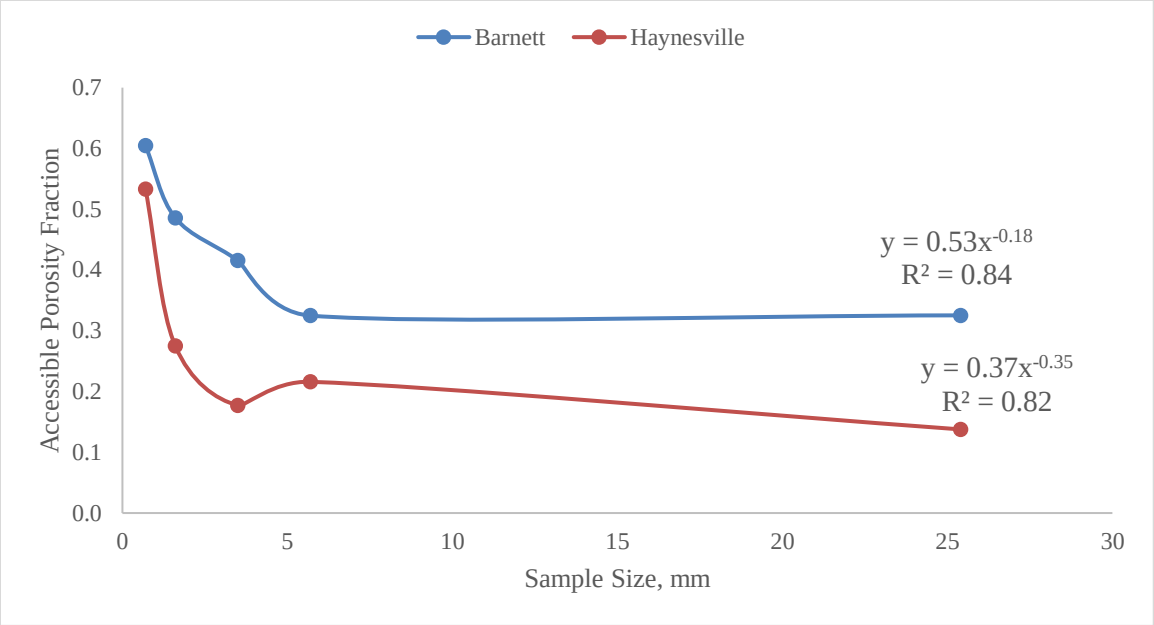


**Figure 3.4: Fraction of accessible porosity as a function of sample size after conformance and compression corrections**

Further, 45 core plug (1-inch) samples from each shale play with MICP and LPP measured porosity values are chosen and accessible pore fraction ($\phi_a/\phi_{LPP}$) are calculated as shown in **Figure 3.5a and 3.5b**. Results show that average accessible pore volume for Barnett samples is around 53%, which this value is around 43% for Haynesville samples. Additionally, results show that the lowest value in Barnett samples is 30% but this number can be as low as 5 % in Haynesville.

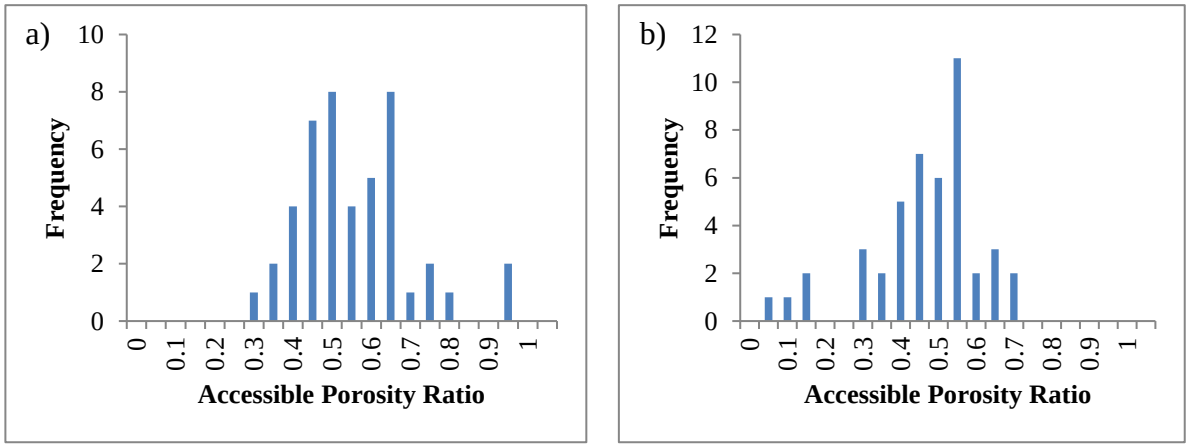


**Figure 3.5: Histogram of the MICP porosity fraction ($\phi_a/\phi_{LPP}$) from 45 samples in plug size for the a) Barnett and b) Haynesville**

It is worth mentioning that pore accessibility depends on the pore network as well as fluid saturation; thus, the estimated accessible pore fractions is likely different for various fluids. Moreover, since pores present both in inorganic part and the organic matter of shale matrix, the wettability can significantly affect pore connectivity (Tinni 2012). Which is why, with MICP test, only connectivity of the rock that partially saturated with mercury can be measured; pores smaller than 3 nm which mercury cannot intrude will not be evaluated using the methodology discussed here. Thus, while acknowledging the limitations of MICP test, current study can still provide important evaluation to understand pore connectivity in shale formations.

### *3.2.2 Permeability*

For further evaluation of matrix hydraulic connectivity, intrinsic permeability values for different sample sizes based on MICP data are calculated and analyzed. Swanson is one of the most widespread permeability estimation models used based on MICP data (Comisky et al., 2007). Swanson, (1981) used the apex of bulk volume mercury saturation, $(S_b)$ to capillary pressure ratio, $(S_b/p_{cap})_A$ to represent the critical point at which major connected pore volumes contributing to permeability have been intruded with mercury. Based on 319 samples studied, Swanson, (1981) suggested that permeability can be determined as a function of $(S_b/p_{cap})_A$:

$$k = 399\left[\frac{S_b}{p_{cap}}\right]_A^{1.691}, \tag{3.1}$$

**Table 3.2** and **Figure 3.6** summarizes results of predicted permeability values using MICP data for different sample sizes for both Barnett and Haynesville. Results indicate that permeability is also strong function of sample size, which with increasing size permeability values decrease. This is an anticipated result since permeability is a strong function of interconnected porosity and as discussed before accessible porosity values decrease with increasing sample size. Although

permeability values for Haynesville is slightly higher than Barnett for small sample size ranges, but at the same time decline rate with increasing sample size is much higher than Barnett. For core plug size samples, calculated permeability value for Barnett is 0.29 µd, where this number is around 0.011 µd for Haynesville. Permeability results at core-scale from both formations are similar to that measured by (Bhandari et al., 2015; Kang et al., 2011; Vermylen, 2011) for Barnett samples and by (Dewers et al., 2012; Tinni et al., 2012) for Haynesville samples

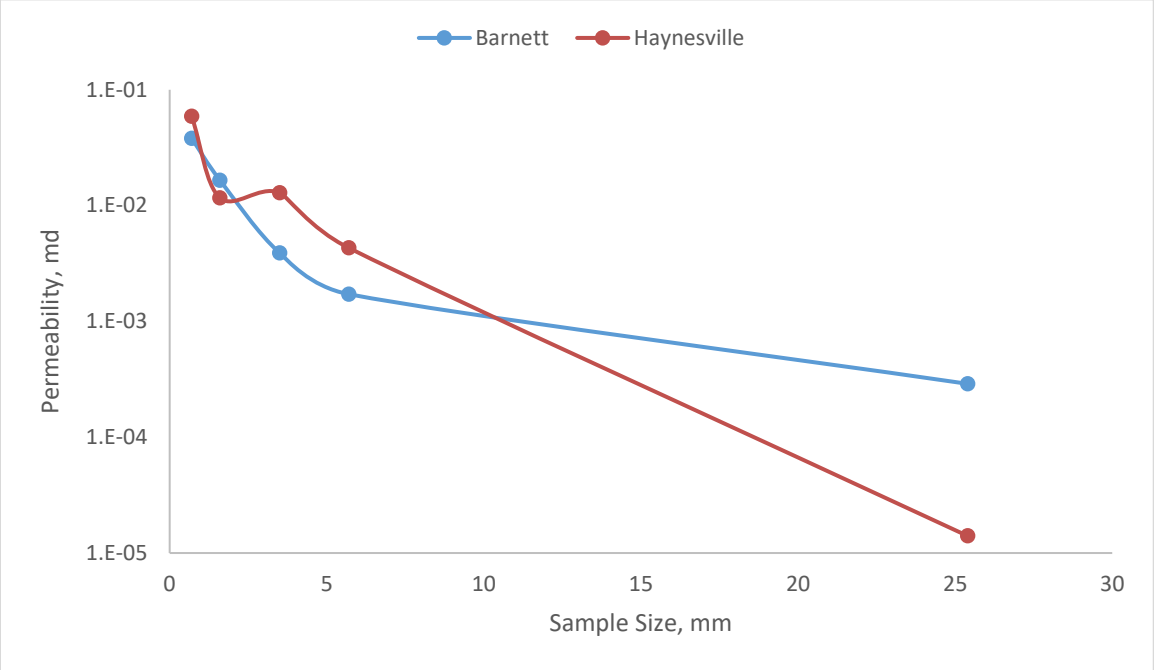


**Figure 3.6: Predicted permeability as a function of sample size**

**Table 3.2: Summary porosity and permeability values for different sample sizes**

| | ***Barnett Shale Sample*** | | ***Haynesville Shale Sample*** | |
|---|---|---|---|---|
| ***Sample Size*** | **MICP Porosity, %** | **K (Swanson), µd** | **MICP Porosity, %** | **K (Swanson), µd** |
| *0.7* | 3.62 | 38.1 | 2.96 | 58.9 |
| *1.6* | 2.91 | 16.6 | 1.53 | 11.7 |
| *3.5* | 2.48 | 3.90 | 0.98 | 12.9 |
| *5.7* | 1.94 | 1.72 | 1.20 | 4.31 |
| *25.4* | 1.95 | 0.29 | 0.76 | 0.0114 |

## 3.3 Connected Porosity and Hydraulic Connectivity – Percolation Theory

### *3.3.1 Accessible/Connected Porosity*

Percolation theory predicts that in a 3-D material with constant total porosity and low connectivity, the portion of porosity that is accessible will decrease with distance, $l$, from the exterior in proportion to $l^{-m}$, until distance exceeds some crossover distance, $\chi$ (Ewing et al., 2012, 2010; Ewing and Horton, 2002; Hu et al., 2015, 2012). Beyond this crossover distance, the accessible porosity either reaches to stable value if pore connectivity is above the critical percolation threshold, $p_c$ or gets zero if connectivity is below the threshold, which it means fluid will not be able to percolate from that rock sample. Rock samples with high connectivity may have $\chi$ on the order of a single pore and accessible porosity will be close to the total porosity, but as pore connectivity decreases, this crossover distance $\chi$ will increase and it becomes close to half the thickness of the sample, when connectivity is close to percolation threshold (Ewing et al., 2012, 2010; Ewing and Horton, 2002; Hu et al., 2015, 2012).

Accessible porosity changes with intragranular distance, $l$ to the grain's exterior and it can be formulized as (Ewing et al., 2010):

$$\phi(l,p)=\begin{cases}\phi_p l^{-m} & for\ l<x\\ \phi_a & for\ l\geq x\end{cases} \tag{3.2}$$

where $p$ represents the probability of accessible pore, $l$ is the sample size, $\chi$ is correlation length beyond which value of accessible pore becomes constant, and $m$ is power law function exponent. If experimental data is fitted to power law function (**Eq. 3.2**), exponent $m$ is 0.18 for Barnett and 0.35 for Haynesville, which indicates that accessible porosity in Haynesville decreases faster with increasing sample size when compared with Barnett results (**Figure 3.4**).

### *3.3.2 Hydraulic Conductivity and Coordination Number*

Two alternative CPA based permeability models discussed in Chapter 2 will be used to analyze pore connectivity as a function of sample size. Permeability model proposed by Daigle (2016) can be simplified if it is assumed that in clay-bearing rocks, $1-\phi p_c \approx 1$ (Revil, 2002), and also $\beta/\phi = 1$, then **Eq. 2.11** can be written as:

$$k = \frac{r_{\max}^2}{8}\phi^2\left(1-p_c\right)^{\frac{2}{3-D}+2}, \tag{3.3}$$

Moreover, critical percolation threshold, $p_c$ can be expressed in terms of coordination number as $p_c = 1.5/z$ (Hunt and Sahimi, 2017; Sahimi, 1995):

$$k = \frac{r_{\max}^2}{8}\phi^2\left(\frac{z-1.5}{z}\right)^{\frac{2}{3-D}+2} \tag{3.4}$$

Alternatively, new permeability model developed (**Eq. 2.32**) can be used:

$$k = \frac{r_m^2}{c}\phi\left[1-\left(\frac{1}{1+t}\right)^{3-D}\right]^t\left(\frac{z-1.5}{z}\right)^{\frac{2}{3-D}}, \tag{3.5}$$

To analyze impact of sample size on pore connectivity/average coordination number, permeability results obtained from MICP data with the Swanson method are evaluated based on **Eq. 3.4 and 3.5**. Maximum pore throat radius, $r_m$ is estimated as 2.24 μm and 1.96 μm for Barnett and Haynesville samples respectively based on first intrusion pressure of mercury. Furthermore, following Yu and Li, (2001), fractal dimension is estimated as a function of porosity, and pore throat radius as:

$$D = 3-\frac{\ln\left(\phi\right)}{\ln\left(r_{\min}/r_{\max}\right)} \tag{3.6}$$

Using **Eq. 3.6**, fractal dimension is estimated as 2.6 for both samples; finally, coordination number as a function of sample size is estimated using **Eq. 3.4 and 3.5** as shown in **Figure 3.7**.

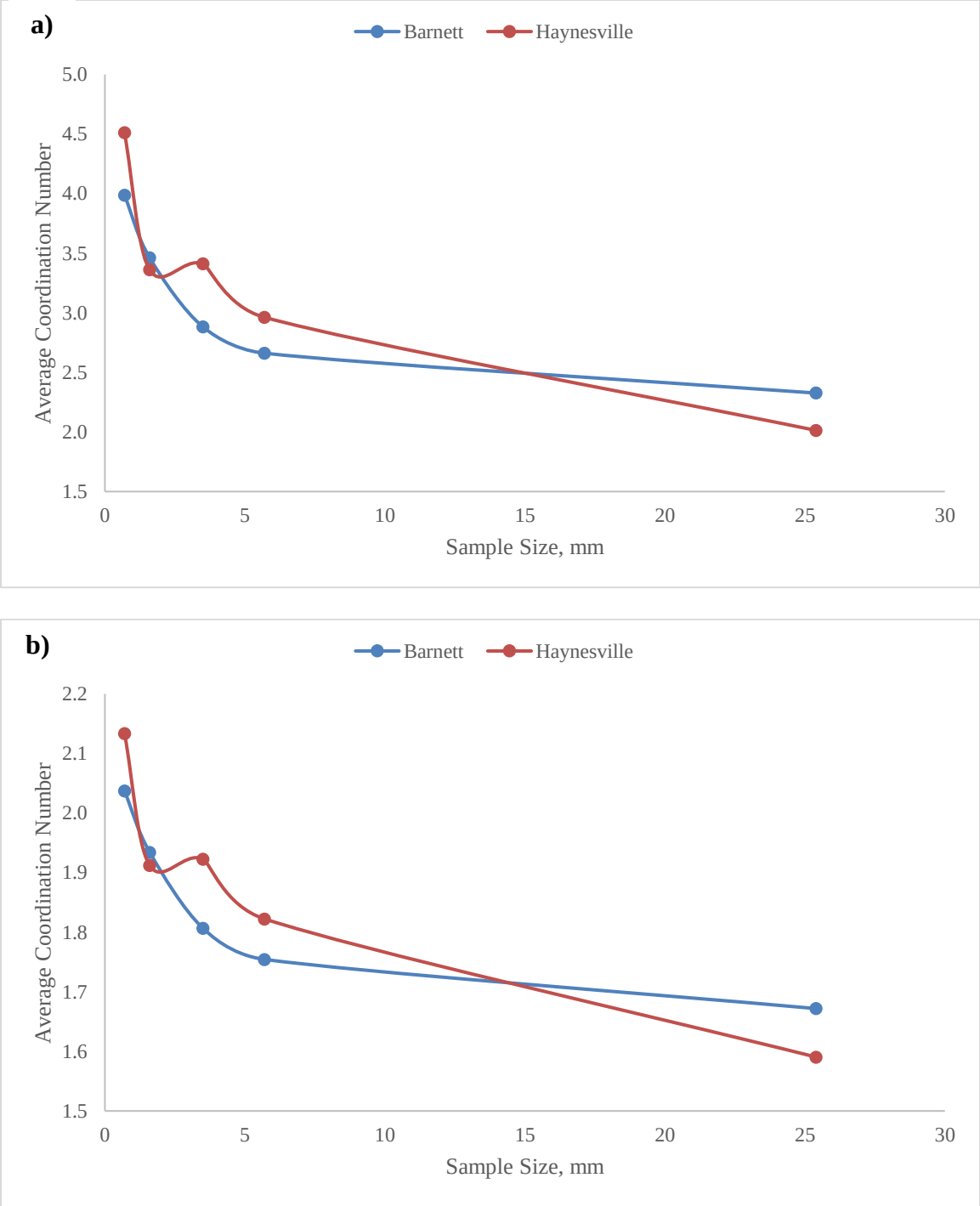


**Figure 3.7: Average coordination number as a function of sample size for the Barnett and Haynesville shale samples a) Daigle model b) Proposed model**

Results indicate that for smallest sample size if initial average coordination number is estimated as 4 for Barnett and 4.5 for Haynesville, then these values reduce to 2.3 and 2 when samples are

at plug size based on Daigle model. In case of proposed model used, coordination number is decreasing from their initial value of 2.04 and 2.13 to 1.67 and 1.57 for Barnett and Haynesville shale samples respectively. Although permeability reduction is two to three orders of magnitude with increasing sample size (**Table 3.2**), this can be explained with reduction in average coordination.

## 3.4 Conclusions

In this chapter, accessible/interconnected porosity and hydraulic connectivity as a function of sample size for Barnett and Haynesville shale formations are evaluated. Moreover, coordination number for both formations are estimated using percolation theory. The main contributions of this chapter are as follows:

- MICP measured accessible porosity values and matrix permeability strongly depends on the sample size; both of them decrease with increasing sample size.
- Accessible porosity and permeability reduction with sample size is more pronounced in Haynesville than Barnett for the samples studied here.
- The estimated average coordination number for both shale plays decreases with the sample size, which can be possible explanation of significant permeability reduction.

# Chapter 4 - Impact of Connectivity Loss on Permeability Reduction

## 4.1 Introduction

In this chapter, aligned with **Obj. 2**, a novel approach is proposed to describe how connectivity loss impacts intrinsic permeability of shale samples under effective stress. One of many challenges for tight formations is that the permeability and porosity change with effective stress is a very complex process. Various experimental studies have been conducted to show permeability variation with respect to effective stress in shale samples (Dong et al., 2010; Metwally and Sondergeld, 2011; Tinni et al., 2012) and results show a nonlinear reduction in permeability with increasing effective stress, where this reduction might be as much as two orders of magnitude. This severe reduction in permeability is often explained through micro-crack closure and pore volume reduction, whereas connectivity loss due to bond breakage between interconnected pores is neglected.

To describe the relationship between permeability reduction and porosity change under effective stress researchers have suggested several empirical models. Shi and Wang, (1986) suggested that the relationship between effective stress and rock permeability should follow a power law, which can be expressed as follow:

$$\frac{K}{K_o} = \left(\frac{P_e}{P_o}\right)^{-\varepsilon}, \tag{4.1}$$

where K denotes the permeability under the net effective stress $P_e$, $K_o$ represents the reference permeability under atmospheric pressure $P_o$ and $\varepsilon$ is a material constant.

On the other hand, David et al., (1994) and Evans et al., (1997) suggested an exponential relationship to model permeability change as a function of effective stress expressed as follow:

$$\frac{K}{K_o} = \exp\left[-\omega\left(P_e - P_o\right)\right], \tag{4.2}$$

ω is a material constant.

Later, Kwon et al., (2001) suggested modified version of Gangi, (1978) permeability (Cubic law) model which reduction in crack permeability of fractured rocks with increasing effective stress, $P_e$ can be described by cubic law function as:

$$\frac{K_f}{K_{f_o}} = \left[1 - \left(\frac{P_e}{P^*}\right)^q\right]^3, \tag{4.3}$$

where $K_f$ denotes the micro-crack permeability under the net effective stress $P_e$, $K_{f_o}$ represents the reference crack permeability at zero effective stress and parameters $q$ and $P^*$ are constants associated with geometry and pore surface topography. "Cubic law" model is one of the most used equation to explain permeability decrease caused because of micro crack closure, the flaw of the equation is also noticeable, which it gives negative $K$ when $P_e$ is larger than $P^*$.

Alternatively, Walsh, (1981) suggested to model fractured permeability reduction as:

$$\frac{K_f}{K_{f_o}} = \left[1 - \left(\frac{\sqrt{2}h}{a_o}\right)\ln\left(\frac{P_e}{P_o}\right)\right]^3, \tag{4.4}$$

where $h$ is the root mean square of the surface roughness and $a_o$ is the half width of fracture aperture. **Eq. 4.4** predicts that the plot of $\left(K_f/K_{f_o}\right)^{1/3}$ as function of $ln(P_e/P_o)$ will be straight line if the permeability reduction is due to crack closure. However, a deviation from the straight line will be observed when rock permeability is not controlled by fractures (Tinni et al., 2012).

Since, permeability is a function of porosity and pore structure, researchers have also studied permeability-porosity relationship under effective stress. David et al., (1994) proposed power law relationship to describe the permeability–porosity relationship induced by mechanical compaction:

$$\frac{K}{K_o} = \left(\frac{\phi}{\phi_o}\right)^{\alpha}, \tag{4.5}$$

where $\alpha$ is a material constant named the porosity sensitivity exponent. Based on Dong et al., (2010) experimental results, porosity sensitivity exponents for sandstone, range from 3 to 6, where these values ranged from 25 to 55 for the tested silty-shale samples. The porosity sensitivity exponent for the silty-shale is considerably higher than that of the sandstone, which clearly indicates that lightly decreased porosity causes dramatic decrease in permeability for shale formations. Kwon et al., (2004) suggested that this large and nonrecoverable decreases observed in permeability of shale samples are due to closure of critical pore links in network and permanent reductions in connected pore space, while the small recoverable changes in permeability represent the elastic response of the pore space.

In this chapter, pore connectivity and the impact of connectivity loss on permeability reduction is investigated under effective stress. Specifically, fractal and percolation theories are used to analyze the effects of pore shrinkage and connectivity loss. Main purpose of this study is to show that pore connectivity might be one of most important factors is shale formations and connectivity reduction under effective stress is significantly high when compared to conventional reservoirs.

### 4.2 Effect of Pore Compressibility and Connectivity Loss

As discussed before conventional KC type permeability models are not sophisticated enough to model complex pore connectivity in tight formations. Thus, percolation theory-based models are essentially developed to address issues associated with bundle of capillary tube hypothesis. Once again, two CPA-based permeability models (Daigle and proposed models) will be used to analyze pore connectivity reduction as a function of effective stress. As discussed before, permeability model proposed by Daigle (2016) can be simplified as:

$$k = \frac{r_m^2}{8}\phi^m \left(\frac{z-1.5}{z}\right)^{\frac{2}{3-D}+m} \tag{4.6}$$

Alternatively, proposed permeability model is expressed as:

$$k = \frac{r_m^2}{c}\phi\left[1-\left(\frac{1}{1+t}\right)^{3-D}\right]^t\left(\frac{z-1.5}{z}\right)^{\frac{2}{3-D}}, \tag{4.7}$$

Assuming pores to be cylindrical ($r_m^2/r_{m_o}^2 = \phi/\phi_o$), based on the permeability model described in **Eq. 4.7**, the effects of both pore shrinkage and bond breakage on permeability reduction can be analyzed as:

$$\overset{\textit{Permeability Reduction Rate}}{\frac{K}{K_o}} = \overset{\textit{Pore Volume Shrinkage}}{\left(\frac{\phi}{\phi_o}\right)^2} * \frac{\overbrace{\left(\frac{z-1.5}{z}\right)^{\frac{2}{3-D}}}^{\textit{Connectivity Loss}}}{\left(\frac{z_o-1.5}{z_o}\right)^{\frac{2}{3-D}}} \tag{4.8}$$

where first and second terms on the right side of **Eq. 4.8** express permeability reduction due to pore volume shrinkage/pore compressibility and connectivity loss, respectively. Alternatively, if Daigle model (**Eq. 4.6**) is used instead, then permeability reduction can be expressed as:

$$\frac{K}{K_o} = \left(\frac{\phi}{\phi_o}\right)^{m+1}\frac{\left(\frac{z-1.5}{z}\right)^{\frac{2}{3-D}+m}}{\left(\frac{z_o-1.5}{z_o}\right)^{\frac{2}{3-D}+m}}, \tag{4.9}$$

From **Eq. 4.8 and 4.9**, $z_o$ is initial coordination number and it can be estimated as a function of initial porosity (Bernabe et al., 2010; Doyen, 1988) as:

$$z_o = A + B\log(\phi), \tag{4.10}$$

where both A and B are constants. Bernabe et al., (2010) suggested that for a two-dimensional system A is 10.4 and B is equal to 6.25. It is worth to mention that, there are very limited studies to understand initial average coordination number in shale formations and it needs further

investigations. However, Ma et al., (2014) and Yang et al., (2015) suggested that coordination number in shale is in the range of 3.

Moreover, by comparing **Eq. 4.8** with Civan (2001) model (**Eq. 2.3**), interconnectivity reduction ($\Gamma/\Gamma_o$) can be expressed as:

$$\frac{\Gamma}{\Gamma_o}=\frac{\left(\frac{z-1.5}{z}\right)^{\frac{2}{3-D}}}{\left(\frac{z_o-1.5}{z_o}\right)^{\frac{2}{3-D}}}=\frac{\frac{K}{K_o}}{\left(\frac{\phi}{\phi_o}\right)^2} \tag{4.11}$$

In case where connectivity loss is negligible and thus coordination number does not vary with increasing pressure ($z/z_o = 1$), last term in **Eq. 4.8 and 4.9** will be equal to 1 and permeability reduction can be estimated as a function of pore volume shrinkage only:

$$\frac{K}{K_o}=\left(\frac{\phi}{\phi_o}\right)^2 \tag{4.12}$$

Please note that, if Daigle model (**Eq. 4.6**) is used, the exponent will become m+1 instead of 2.

### 4.3 Results

To evaluate impact of both pore compressibility and bond breakage on permeability reduction, experimental data for two sandstone and two shale samples are selected from literature (Dong et al., 2010). To measure porosity and intrinsic permeability Dong et al., (2010) conducted experiments by gradually increasing the confining pressure from 435 to 725 psia, then to 1450 psia, and finally up to 17,000 psia (in 1450 psia increments), while keeping pore pressure constant. **Table 4.1** and **Table 4.2** summarizes experimental data for sandstone and shale samples respectively.

**Table 4.1: Porosity and permeability data for sandstone samples under effective stress (Adopted from Dong et al., 2010)**

| *Sandstone # 1* | | | *Sandstone # 2* | | |
|---|---|---|---|---|---|
| **Net Stress, psi** | **Poros*ity, %*** | ***Permeability*, md** | **Net Stress, psi** | **Poros*ity, %*** | ***Permeability*, md** |
| 545 | 18.0 | 76.1 | 694 | 17.6 | 73.0 |
| 1250 | 17.4 | 66.3 | 1421 | 17.1 | 66.3 |
| 2734 | 16.8 | 59.3 | 2881 | 16.7 | 61.2 |
| 4180 | 16.5 | 55.8 | 4260 | 16.4 | 57.9 |
| 5665 | 16.3 | 53.3 | 5744 | 16.2 | 56.3 |
| 7091 | 16.2 | 52.6 | 7265 | 16.1 | 54.7 |
| 8556 | 16.1 | 50.3 | 8560 | 16.0 | 54.1 |
| 10040 | 16.0 | 48.8 | 10043 | 15.9 | 52.7 |
| 11505 | 15.9 | 46.7 | 11488 | 15.8 | 51.8 |
| 12951 | 15.8 | 44.6 | 12784 | 15.8 | 51.2 |
| 14397 | 15.7 | 43.3 | 14265 | 15.7 | 50.2 |
| 15881 | 15.7 | 41.4 | 15636 | 15.6 | 49.2 |
| 17346 | 15.6 | 40.2 | 17079 | 15.6 | 48.7 |

**Table 4.2: Porosity and permeability data for shale samples under effective stress (Adopted from Dong et al., 2010)**

| *Shale # 1* | | | *Shale # 2* | | |
|---|---|---|---|---|---|
| **Net Stress, psi** | **Poros*ity, %*** | ***Permeability*, µd** | **Net Stress, psi** | **Poros*ity, %*** | ***Permeability*, µd** |
| 388 | 9.1 | 1.28 | 1113 | 10.69 | 9.71 |
| 1236 | 8.9 | 0.36 | 1881 | 10.56 | 4.51 |
| 1904 | 8.8 | 0.28 | 2571 | 10.46 | 2.32 |
| 2684 | 8.7 | 0.25 | 4081 | 10.28 | 0.95 |
| 3408 | 8.7 | 0.23 | 5512 | 10.16 | 0.53 |
| 4112 | 8.6 | 0.21 | 7000 | 10.07 | 0.35 |
| 5579 | 8.5 | 0.17 | 8468 | 10.00 | 0.23 |
| 7046 | 8.4 | 0.13 | 9992 | 9.93 | 0.17 |
| 8473 | 8.4 | 0.12 | 11401 | 9.87 | 0.14 |
| 9883 | 8.3 | 0.09 | 12847 | 9.81 | 0.13 |
| 11387 | 8.3 | 0.08 | 14295 | 9.74 | 0.10 |
| 12871 | 8.2 | 0.07 | 15799 | 9.67 | 0.09 |
| 14337 | 8.1 | 0.06 | 17246 | 9.61 | 0.07 |
| 15726 | 8.1 | 0.06 | | | |
| 17249 | 8.1 | 0.05 | | | |

**Figure 4.1** illustrates porosity reduction/porosity ratio, $(\phi/\phi_o)$ under effective stress for both sandstone and shale samples. Results indicate that when effective stress reaches 17,000 psi,

porosity reduction in sandstone samples are close to 13%, and 11% whereas this value is around 9-10% for both shale samples. On the other hand, when permeability reduction rates are compared for the both samples, it can be observed that, permeability values for two shale samples are 99% and 96% less than their initial point when effective stress is increased to 17,250 psi; whereas for sandstone samples, these values are 47% and 33%. **(Figure 4.2).** These two observations clearly indicate the importance of bond breakage and connectivity loss in the shale samples.

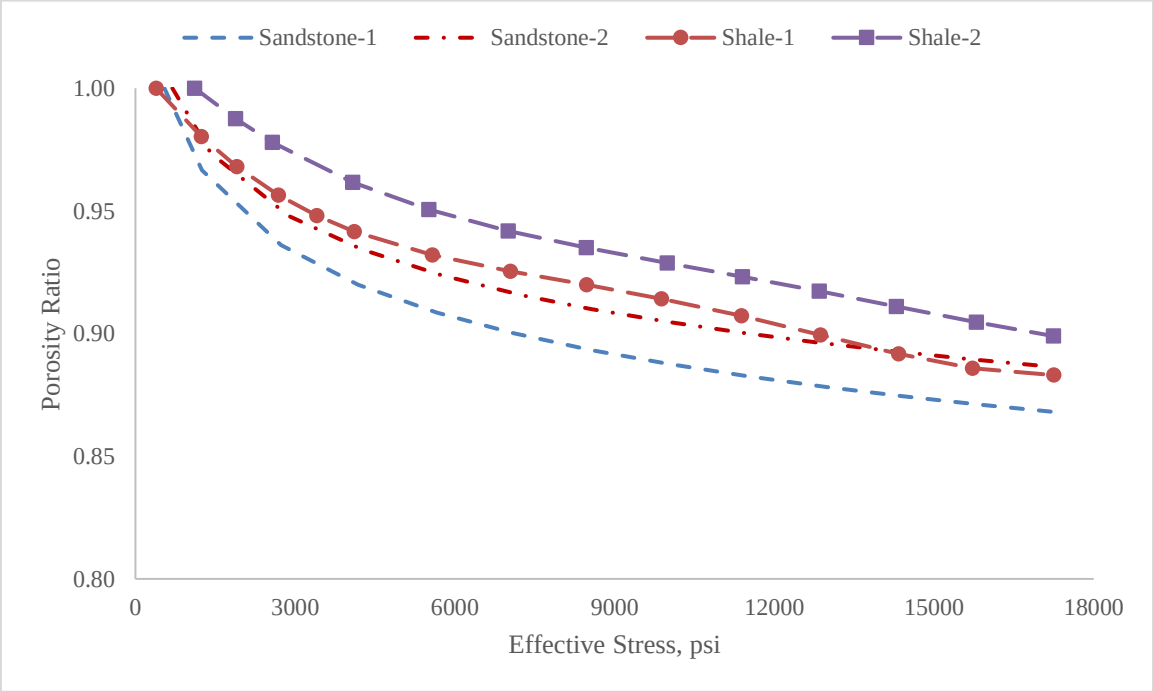


**Figure 4.1: Porosity as a function of effective stress (Dong et al. 2010)**

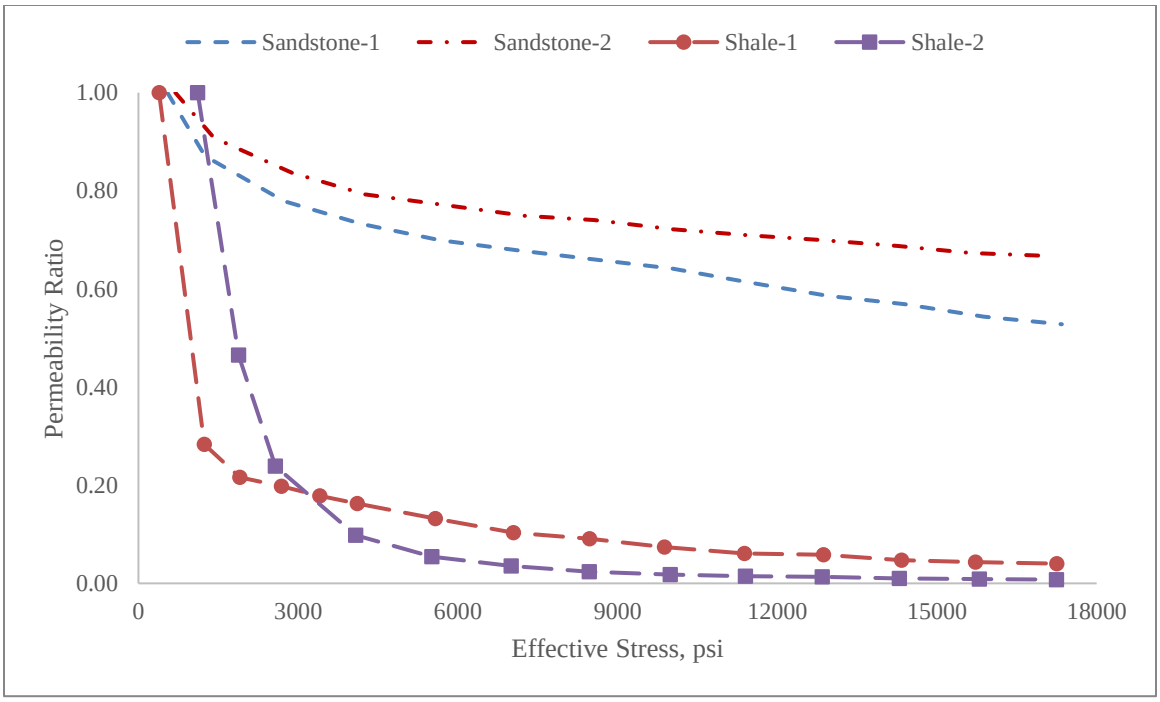


**Figure 4.2: Permeability as a function of effective stress (Dong et al. 2010)**

To evaluate connectivity loss under effective stress, interconnectivity ratio is estimated based on **Eq. 4.11** and coordination number reduction is calculated from **Eq. 4.8.** In all calculations, fractal dimension, D is assumed to be equal to 2.5 and formation factor exponent, $m$ is considered as a universal exponent equal to 2 (Clerc et al., 2000; Daigle, 2016; Stauffer and Aharony, 1994).

Based on proposed permeability model, results indicate that when effective stress exceeds 17,000 psi for sandstone samples, coordination number has reduced 19%: from its initial value of 5.72 to 4.62 for the first sample and 10% for the second sample: from 5.62 to 5.06. Interconnectivity reduction is 30% and 15% respectively as shown in **Figure 4.3** and **Table 4.3**. Thus, it can be concluded that for sandstone samples, permeability reduction is mainly dominated by pore volume shrinkage and impact of connectivity loss is insignificant (**Figure 4.4**).

Alternatively, if Daigle model (**Eq. 4.6**) is used, then coordination number reduction is only 7% and 1.5%, whereas interconnectivity reduction is around 19% and 4% for the first and second sandstone samples, respectively.

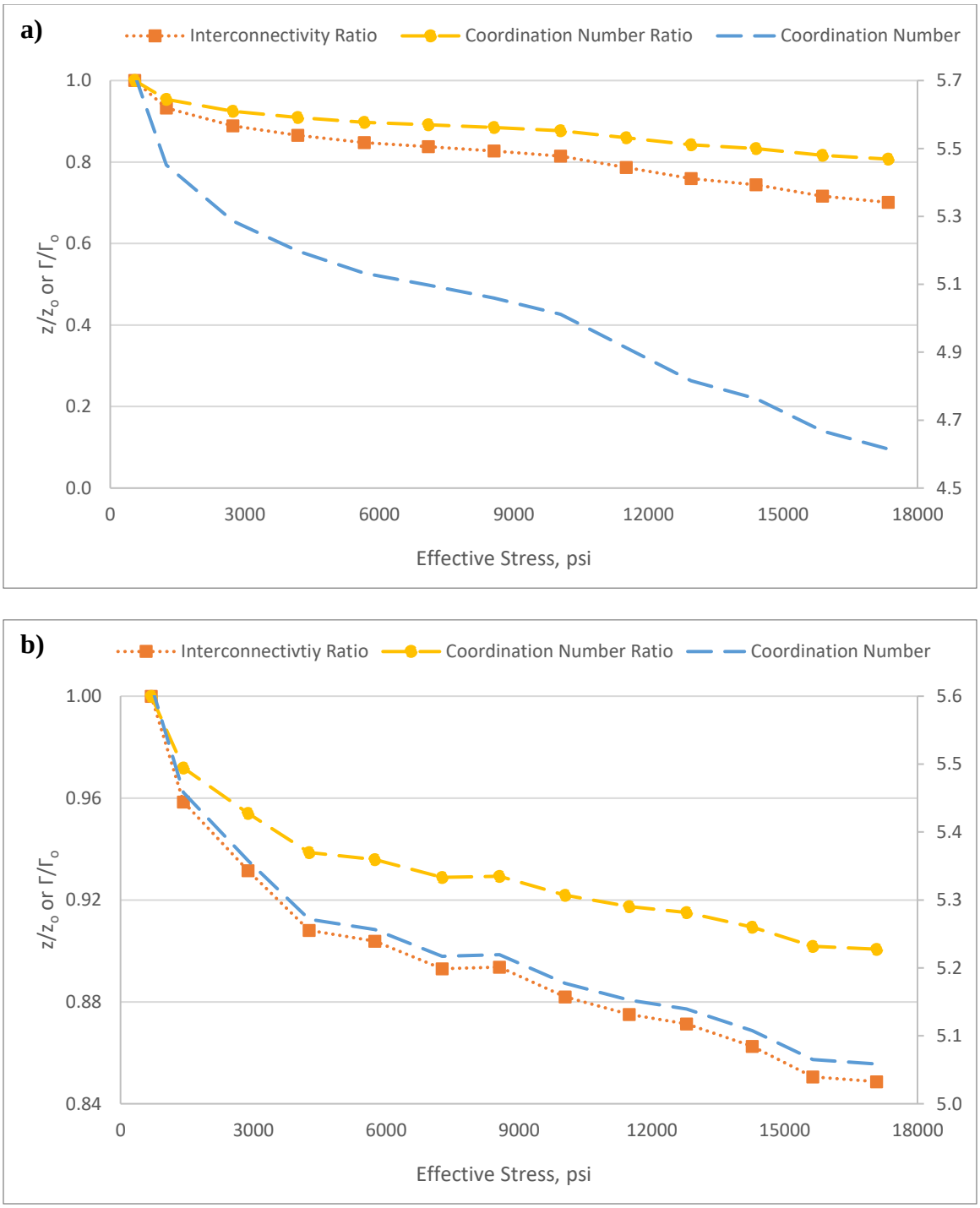


**Figure 4.3: Interconnectivity parameter and coordination number as a function of effective stress calculated from proposed model for a) sandstone #1 b) sandstone #2**

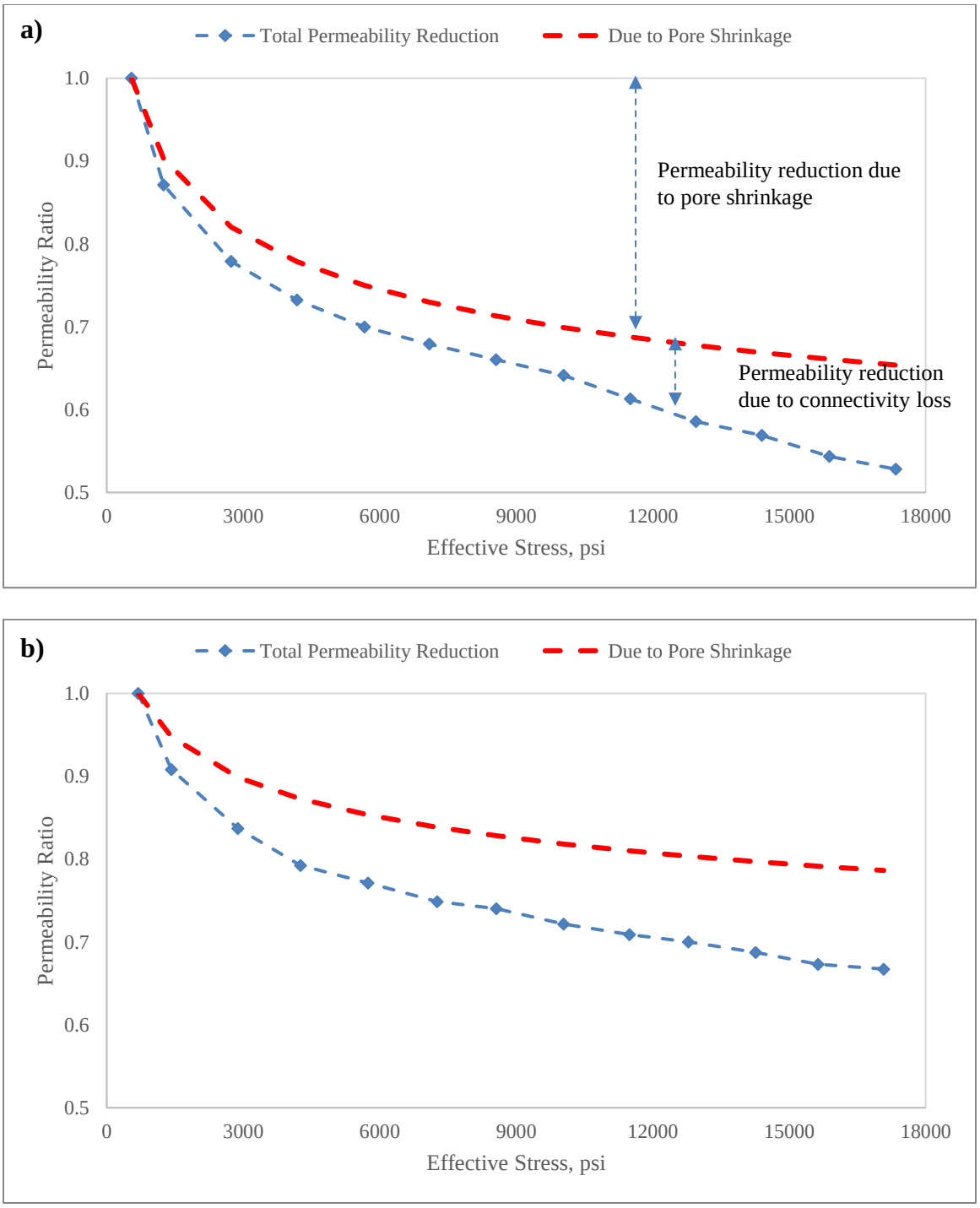


**Figure 4.4: Permeability reduction as a function of effective stress calculated from proposed model for a) sandstone #1 b) sandstone #2**

**Table 4.3: Calculated parameters for sandstone samples under effective stress**

| *Sandstone # 1* | | | *Sandstone # 2* | | |
|---|---|---|---|---|---|
| **Net Stress, psi** | **Interconnectivity Ratio $(\Gamma/\Gamma_o)$** | ***Coordination Number, z*** | **Net Stress, psi** | **Interconnectivity Ratio $(\Gamma/\Gamma_o)$** | ***Coordination Number, z*** |
| 545 | 1.00 | 5.72 | 694 | 1.00 | 5.62 |
| 1250 | 0.93 | 5.45 | 1421 | 0.96 | 5.46 |
| 2734 | 0.89 | 5.29 | 2881 | 0.93 | 5.36 |
| 4180 | 0.87 | 5.20 | 4260 | 0.91 | 5.27 |
| 5665 | 0.85 | 5.13 | 5744 | 0.90 | 5.26 |
| 7091 | 0.84 | 5.10 | 7265 | 0.89 | 5.22 |
| 8556 | 0.83 | 5.06 | 8560 | 0.89 | 5.22 |
| 10040 | 0.81 | 5.01 | 10043 | 0.88 | 5.18 |
| 11505 | 0.79 | 4.91 | 11488 | 0.88 | 5.15 |
| 12951 | 0.76 | 4.82 | 12784 | 0.87 | 5.14 |
| 14397 | 0.74 | 4.76 | 14265 | 0.86 | 5.11 |
| 15881 | 0.72 | 4.67 | 15636 | 0.85 | 5.06 |
| 17346 | 0.70 | 4.62 | 17079 | 0.85 | 5.06 |

On the other hand, for the shale sample, if permeability reduction $(K/K_o)$ is estimated only as a function of porosity ratio $(\phi/\phi_o)$, then porosity sensitivity exponent, $\alpha$ should be as high as 50, which indicates that slightly change in porosity results in drastic permeability decrease and clearly shows the impact of fracture closure and connectivity loss on permeability reduction. To identify and differentiate micro crack closure region, Walsh model (**Eq. 4.4**) is used as shown in **Figure 4.5**. As discussed before, if permeability reduction is dominated by fracture closure, then the plot of $(K/K_o)^{1/3}$ as function of $ln(P_e/P_o)$ will be straight line. A deviation from the straight line at later stage is attributed to pore volume shrinkage and connectivity loss (Tinni et al., 2012). Based on Walsh model (**Eq. 4.4**), results indicate that all micro-cracks are closed at 1236 psi for the first sample and at 2570 psi for the second sample and thus, impact of pore shrinkage and connectivity loss is estimated after these effective stresses.

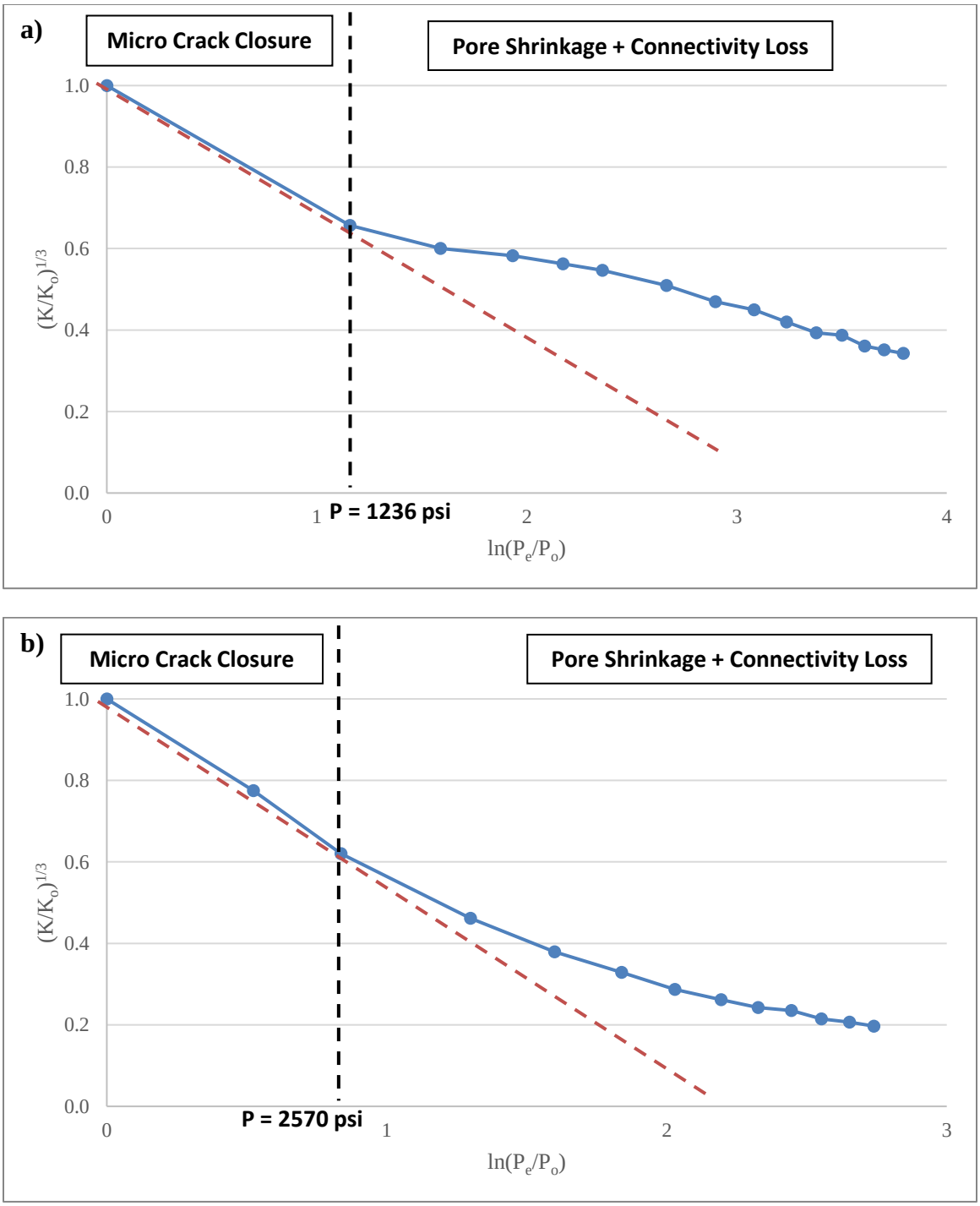


**Figure 4.5: Plot of $(K/K_o)^{1/3}$ as a function of $ln(P_e/P_o)$ for a) shale #1 b) shale #2**

After initial coordination numbers are estimated based on **Eq. 4.10**, interconnectivity ratio and coordination number reduction are calculated from **Eq. 4.8 and 4.9.** Results indicate that for the

shale samples, when effective stress exceeds 17,000 psi, coordination number has reduced 36%: from its initial value of 3.84 to 2.48 for the first sample and 51% for the second sample: from 4.29 to 2.1. Interconnectivity reduction is 83% and 96%, respectively as shown in **Figure 4.6** and **Table 4.4**. When impact of pore shrinkage and connectivity loss are compared for shale samples, it is clear that effect of pore bond breakage (coordination number reduction) is dominant as shown in **Figure 4.7**. If Daigle model is used alternatively, then coordination number reduction is around 22% and 38%, whereas interconnectivity reduction is estimated as 81% and 96% for shale samples. Thus, permeability reduction under effective stress for shale samples can be summarized as micro crack closure dominated at early stage and connectivity loss dominated at later stage.

**Table 4.4: Calculated parameters for shale samples under effective stress**

| ***Shale # 1*** | | | ***Shale # 2*** | | |
|---|---|---|---|---|---|
| **Net Stress, psi** | **Interconnectivity Ratio $(\Gamma/\Gamma_o)$** | ***Coordination Number, z*** | **Net Stress, psi** | **Interconnectivity Ratio $(\Gamma/\Gamma_o)$** | ***Coordination Number, z*** |
| 388 | | | 1113 | | |
| 1236 | 1.00 | 3.84 | 1881 | | |
| 1904 | 0.78 | 3.51 | 2571 | 1.00 | 4.29 |
| 2684 | 0.73 | 3.44 | 4081 | 0.43 | 3.16 |
| 3408 | 0.67 | 3.35 | 5512 | 0.24 | 2.76 |
| 4112 | 0.62 | 3.27 | 7000 | 0.16 | 2.55 |
| 5579 | 0.52 | 3.10 | 8468 | 0.11 | 2.39 |
| 7046 | 0.41 | 2.93 | 9992 | 0.08 | 2.31 |
| 8473 | 0.37 | 2.85 | 11401 | 0.07 | 2.24 |
| 9883 | 0.30 | 2.73 | 12847 | 0.06 | 2.22 |
| 11387 | 0.25 | 2.64 | 14295 | 0.05 | 2.15 |
| 12871 | 0.24 | 2.62 | 15799 | 0.04 | 2.13 |
| 14337 | 0.20 | 2.53 | 17246 | 0.04 | 2.10 |
| 15726 | 0.19 | 2.51 | | | |
| 17249 | 0.17 | 2.48 | | | |

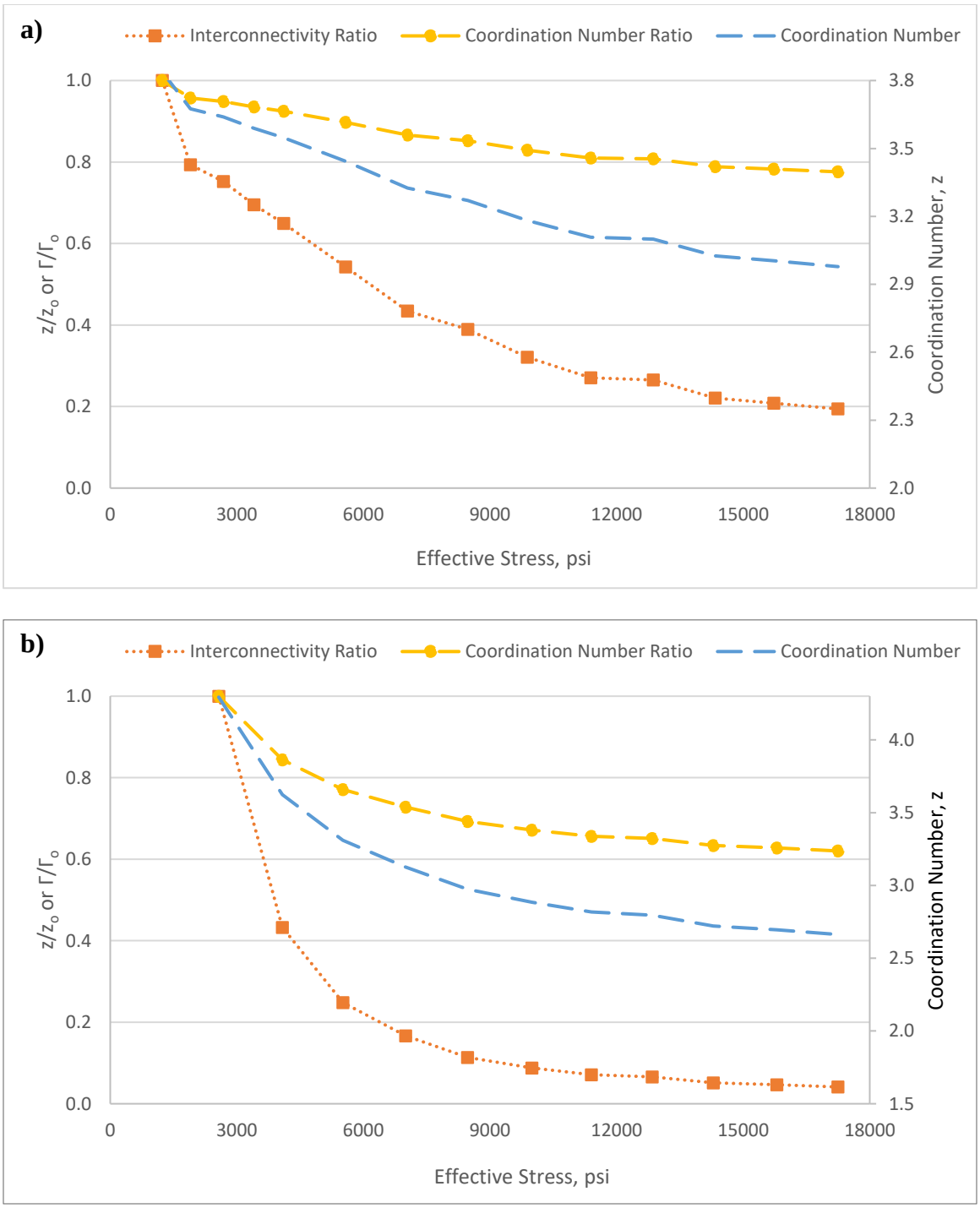


**Figure 4.6: Interconnectivity parameter and coordination number as a function of effective stress calculated from proposed model (after micro-crack closure corrected) for a) shale #1 b) shale #2**

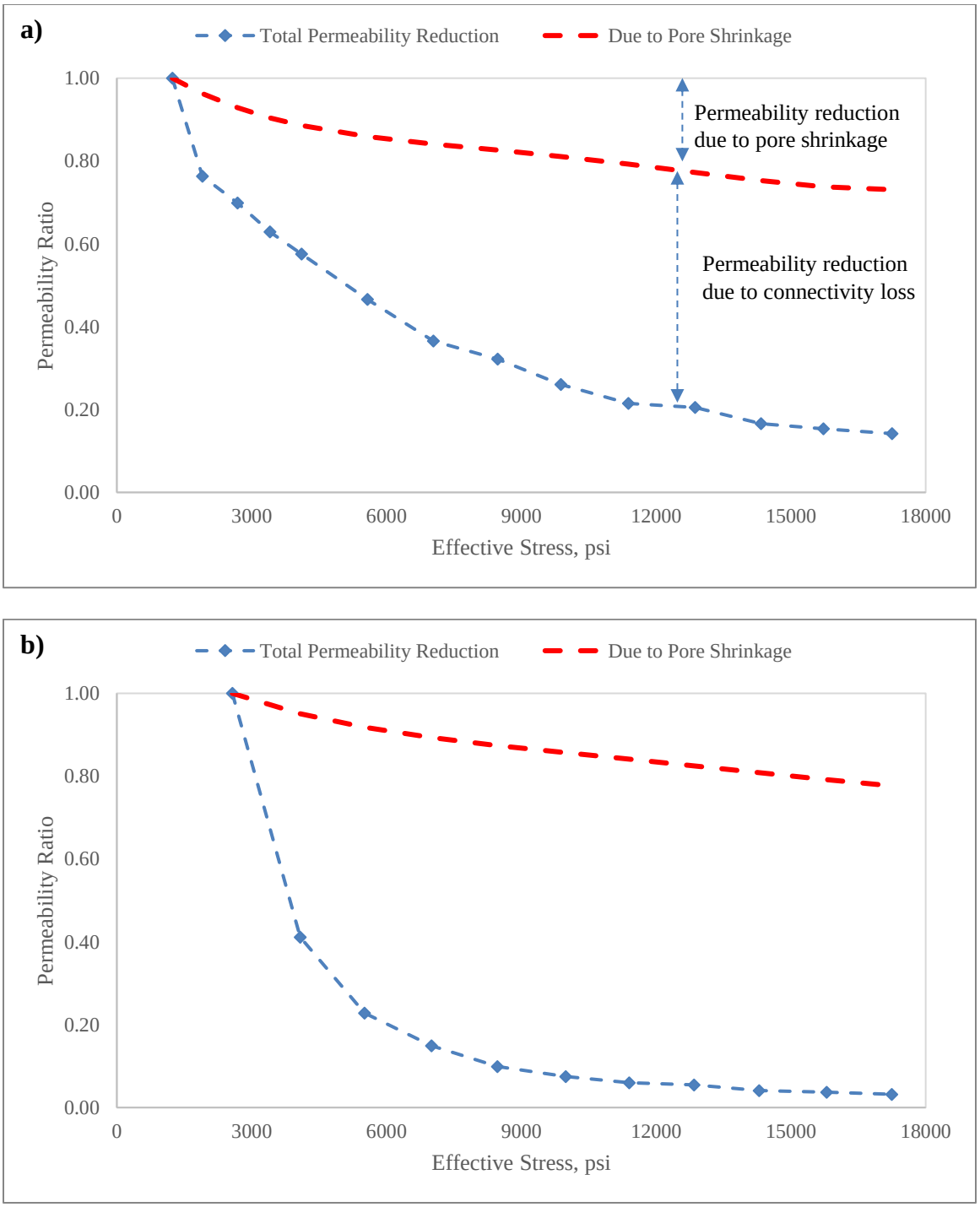


**Figure 4.7: Permeability reduction as a function of effective stress calculated from proposed model (after micro-crack closure corrected) for a) shale #1 b) shale #2**

Finally, for shale sample #1, effect of fractal dimension on calculated coordination number reduction is analyzed. As illustrated in **Figure 4.8** fractal dimension values are increased coordination number reduction decreases.

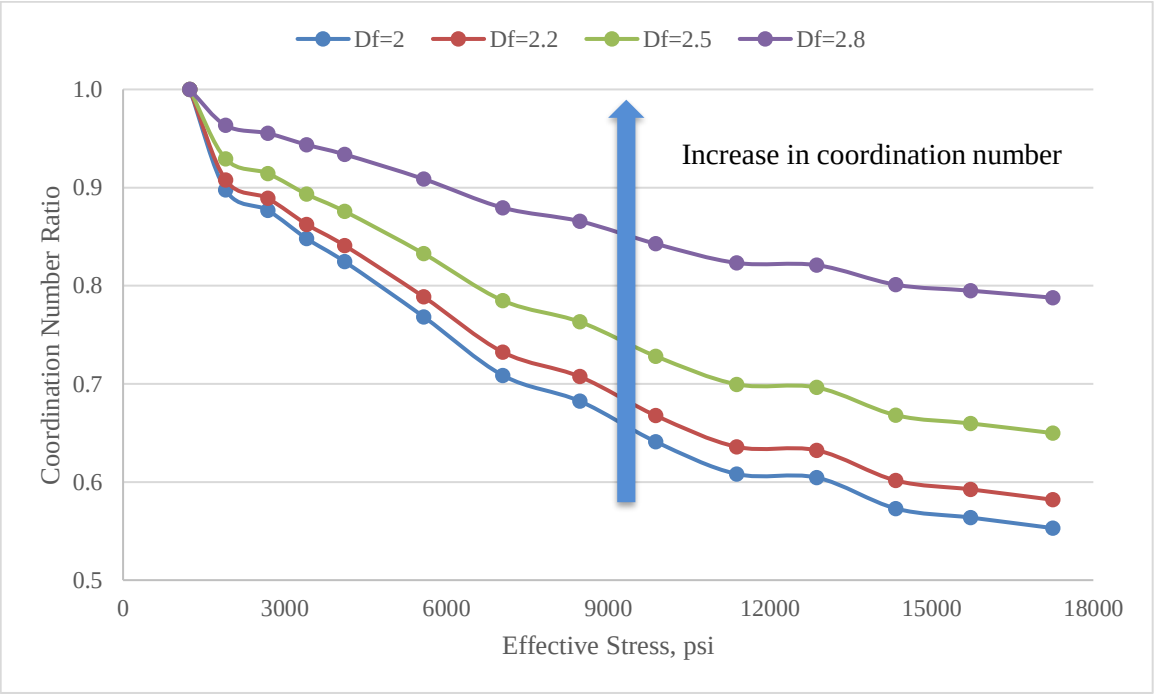


**Figure 4.8: Coordination number ratio as a function of effective stress for different fractal dimension numbers**

Finally, it is worth to mention that, since pore diameters in tight formations are in the order of nano meters, this will cause a violation of the Darcy's law. Depending on the pore size and gas properties, non-Darcy flow mechanisms such as slip-flow, molecular diffusion, and Knudsen diffusion can affect the matrix permeability. Thus, it is essential to distinguish and incorporate all important physical parameters accordingly to estimate permeability evolution under effective stress. During production, as pore pressure decreases, the effective stress will increase and that can potentially lead to intrinsic permeability reduction because of pore shrinkage and connectivity loss. At the same time, due to the effect of Non-Darcy flow regimes, apparent permeability will increase (**Figure 4.9**). Depending on the pore type, size, and topography as well as pore pressure, one of

the above effects may dominate matrix permeability. However, non-Darcy flow regimes and their effect on permeability is beyond the scope of the present chapter and is not discussed further here.

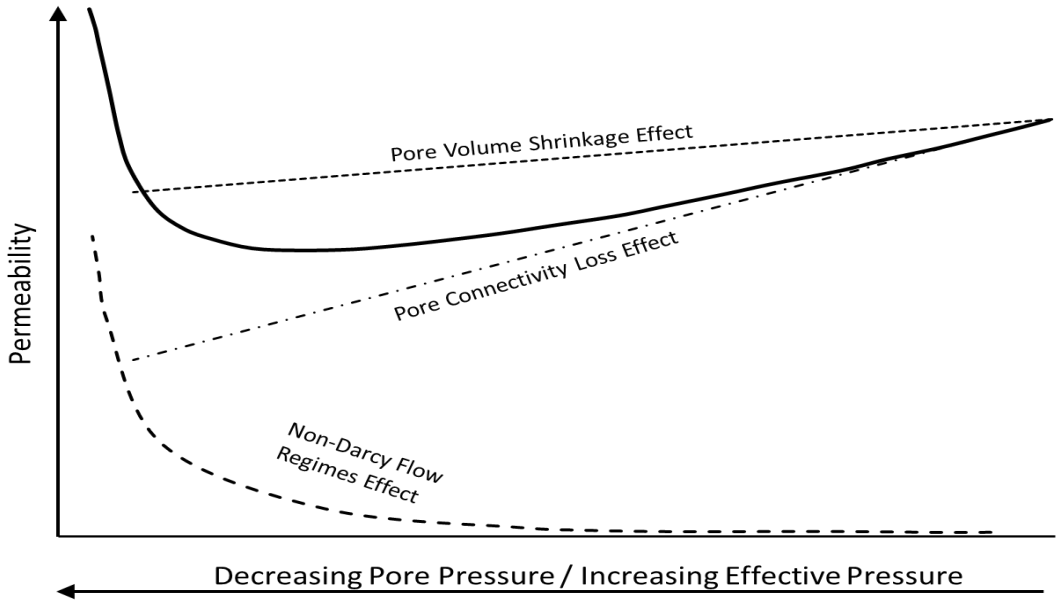


**Figure 4.9: Shale gas permeability considering the combined effects of Non-Darcy flow regimes, pore volume shrinkage and pore connectivity loss (solid line) (Davud Davudov and Moghanloo, 2018b).**

## 4.4 Conclusions

In this chapter, a new approach to model permeability reduction under effective stress in tight formations is developed. The impact of pore compressibility and bond breakage on permeability reduction was analyzed using the percolation theory-based permeability model. Major outcomes of this study are as follows:

- Permeability reduction in shale plays can be explained with a combination of micro-crack closure at early stage and pore shrinkage and connectivity loss at later stage. As observed in shale samples studied, if significant permeability reduction is accompanied by limited porosity change, then connectivity loss can be expressed as the main reason.

- While connectivity loss is slight in sandstone samples, it is identified as the main mechanism controlling permeability reduction in shale samples studied.
- When effective stress exceeds 17,000 psi, average coordination number has significantly reduced 36 and 51% resulting in 7- and 33-times reduction in permeability for two shale samples studied here.

# Chapter 5 – Permeability Based on SEM Images

## 5.1 Introduction

This chapter presents numerical simulation results of fluid flow through intrinsic 3D pore structure of an Eagle Ford shale sample obtained from stacked 2D SEM images to address **Obj. 3**. With increased computational capabilities, direct pore scale modeling has become feasible and reliable method to evaluate fluid flow and transport properties while preserving the complex structure of the constructed porous media. In this chapter three-dimensional (3D) pore structure of an Eagle Ford shale sample is constructed and compiled from two-dimensional (2D) image obtained with focused ion beam-scanning electron microscope (FIB-SEM) technique. The compiled 3D pore structure is further analyzed to determine static petrophysical properties as well as permeability measurements using numerical fluid flow simulations. One of the main objectives is to understand and evaluate impact of sample size on the calculated parameters and to understand the pore connectivity effect on fluid flow and permeability.

The studied Eagle Ford sample is composed of 600 stacked images with 2321 x 1986 pixels and the resolution of 10 nm/pixel in all three directions. The original gray-scale images are converted to binary (black and white) forms with an appropriate segmentation method as shown in **Figure 5.1**. All SEM images for Eagle Ford shale samples have been provided by Unconventional Shale Gas Consortium at the University of Oklahoma.

Before simulating fluid flow through pore space, basic static properties, such as pore size distribution, total porosity, and the connected porosity are evaluated using ImageJ®, an open-source image analysis software. Next, Lattice Boltzmann Method (LBM) is used to simulate fluid flow through the constructed 3D pore space to calculate permeability of studied sample. Finally,

the pore connectivity is quantified based on Euler-Poincare Characteristics (EPC) as a function of sample size. The workflow of this work is summarized in **Figure 5.2.**

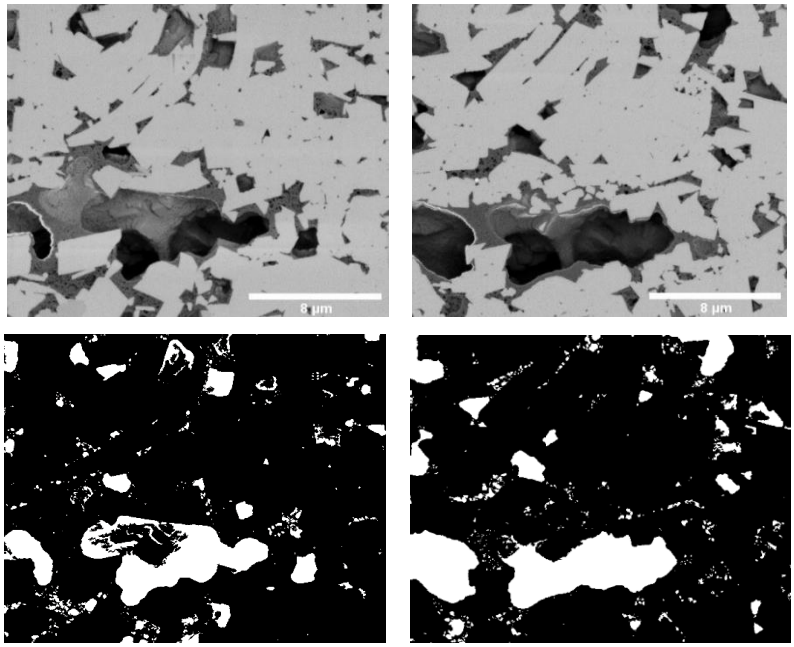


**Figure 5.1: Example of 2D grayscale and binary images from Eagle Ford sample**

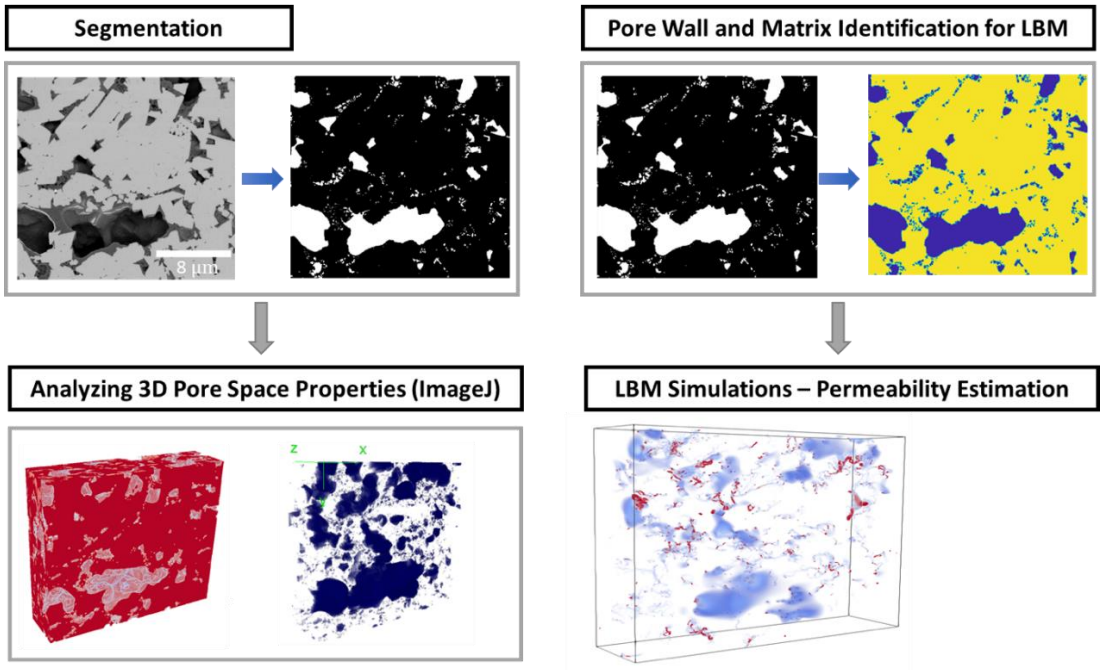


**Figure 5.2: Major workflow of this chapter**

## 5.2 Methodology

### *5.2.1 Direct Pore Scale Modelling – Lattice Boltzmann Method*

For fluid flow through complex systems, such as porous media, the LBM is often considered as one of the most efficient and accurate simulation methods. The most important advantage of LBM is its capability to be applied directly to the real complex pore space without any need for simplified and/or approximated pore structure models (Chi and Heidari, 2016; Succi, 2001; Sukop and Thorne, 2007). Fundamentally, the LBM considers a collection of particles as a unit cloud of particles and solves the discretized Boltzmann equation for these specified particle units as they evolve in space-time domain and interact on a regular lattice.

The LBM algorithm consists of two steps: Step 1: streaming (advection), in which particles moves to the closest node in the direction of their velocity, and Step 2: collision, at which particles interact with each other based on the defined collision rules at particular node, while conserving mass and momentum. Similar to the kinetic equation of the lattice gas cellular automata, discretized form of LBM is usually expressed as follow:

$$f_i(x + c_i\Delta t, t + \Delta t) - f_i(x,t) = \Omega_i(f(x,t)), \tag{5.1}$$

where $f_i(x,t)$ is the particle distribution function at location $x$ and time $t$, $\Omega_i$ is the collision operator, and $c_i$ is the local particle velocity, proportional to a constant lattice velocity: $c = \Delta x/\Delta t$ (Guiet, et al., 2011).

The collision operator in **Eq. 5.2** is often defined with the Bhatnagar-Gross-Krook (BGK) operator since it allows to solve the Boltzmann equation in a computationally efficient method. BGK is derived from linearization of the collision operator around the equilibrium state, neglecting the higher-order terms (Bhatnagar et al., 1954; Guiet et al., 2011):

$$\Omega_i = \frac{1}{\tau}(f_i(x,t) - f_i^{eq}(x,t)), \tag{5.2}$$

where τ is the relaxation time and $f_i^{eq}$ is the local equilibrium state. Relaxation time is directly related to the kinematic viscosity, ν as follow:

$$\tau = \frac{3\nu}{\Delta t \cdot c^2} + \frac{1}{2}, \tag{5.3}$$

It is clear from **Eq. 5.3** that for numerical stability, relaxation time should be higher than $1/2$. Moreover, it has been discussed in the literature that the best practice to maintain the numerical stability is to set relaxation time equal to 1.

The equilibrium distribution $f_i^{eq}$ from BGK operator corresponds to an ideal state derived from the second order approximation of a Maxwellian distribution function and expressed in terms of macroscopic flow parameters under low-Mach assumption to ensure fluid incompressibility (Guiet et al., 2011):

$$f_i^{eq}(\rho, \mathrm{u}) = \rho w_i \left(1 + \frac{3}{c^2} c_i \cdot u + \frac{9}{2c^4}(c_i \cdot u)^2 - \frac{3}{2c^2} u^2\right) \tag{5.4}$$

where $w_i$ is the weighting parameters specifically defined for each lattice scheme. Finally, macroscopic flow characteristics (mass and momentum) are calculated as follow:

$$\rho = \sum_i f_i(x,t) = \sum_i f_i^{eq}(x,t) \tag{5.5}$$

$$\rho u = \sum_i \frac{f_i(x,t)}{c^2} c_i = \sum_i \frac{f_i^{eq}(x,t)}{c^2} c_i \tag{5.6}$$

The set of **Eqns. 5.1-5.6** along with specific boundary conditions help us simulate fluid flow using the lattice Boltzmann framework. Very often, for simplicity $\Delta x/\Delta t = 1$ is chosen, since it enables us to work with *c* equal to 1 (Guiet et al., 2011). In this work, D3Q19 scheme is implemented for

LBM simulations which describes motion in 3D with 19 possible velocity distributions, as shown in **Figure 5.3**.

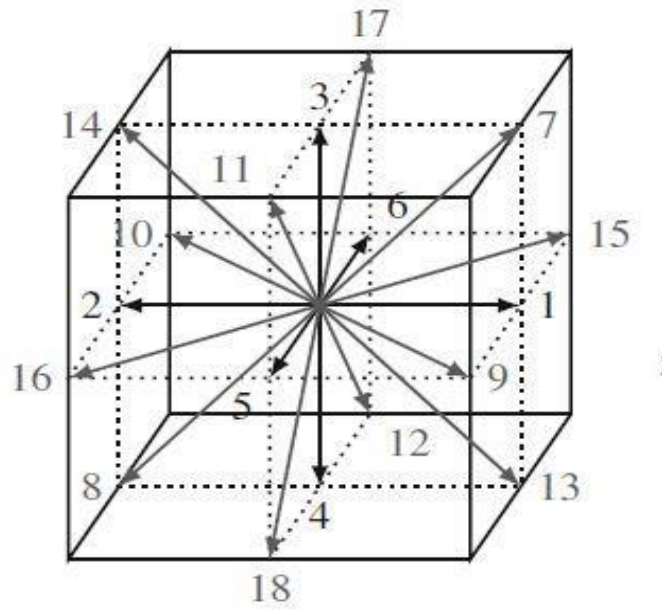


**Figure 5.3: Velocity discretization in D3Q19 lattice scheme**

**LBM Implementation with Palabos**: To calculate permeability for the selected shale sample, the open-source LBM library Palabos, written in C++ is used (Latt, 2009). Single phase, single component (SPSC) fluid flow simulations are modelled using the constructed 3D pore structures. To construct the pore structure, 2D binary images obtained from FIB-SEM have been binarized as 0 for pore space (dark blue), 1 for the wall of the pores (light blue) and 2 for the rest of the matrix (yellow) as shown in **Figure 5.4**. Accordingly, two types of boundary conditions were applied to rock gains (solid part of matrix); bounce-back (no-slip boundaries) and 'no dynamics' boundaries. As illustrated in **Figure 5.4**, if there is any pore space in the vicinity of solid part of the matrix (light blue color), then for those grid blocks bounce-back boundary condition is applied. It is a common practice to use bounce-back boundary condition for LBM simulation which corresponds to the no-slip boundary condition in fluid mechanics. The basic idea behind bounce-back boundary

condition is that after particles hit a solid wall node, they will be "bounced back" to their previous node in the pore space which they have moved from. On the other hand, for the grids that are located deep in the matrix with no immediate proximity to pore space (yellow), no dynamics boundary condition (no transport phenomenon) is considered to reduce the computational cost of simulation (Degruyter et al., 2010). Finally, the inlet and outlet boundaries are characterized by the constant pressure boundary conditions. Once the simulation reaches steady state, average velocity and further permeability, *k*, is calculated from Darcy equation.

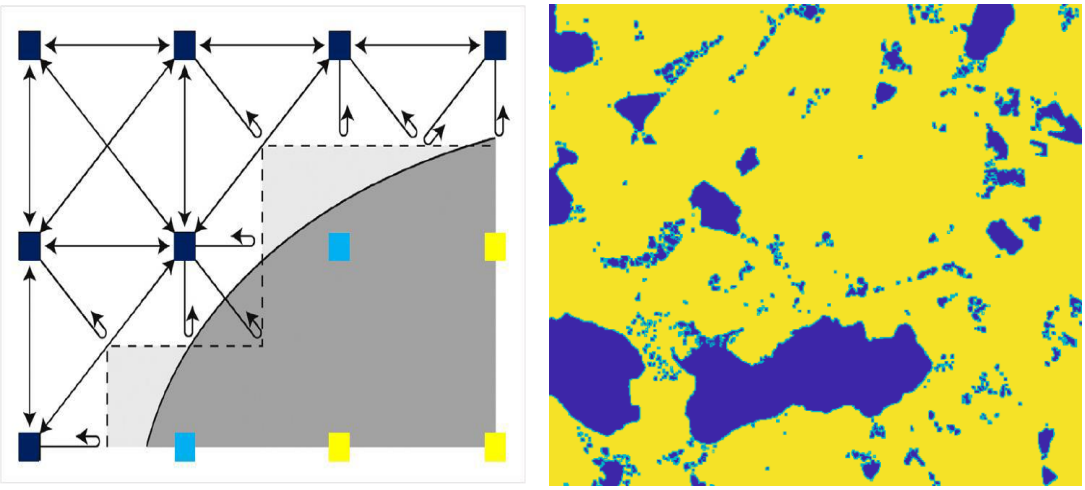

**Figure 5.4: Boundary conditions in the LBM (adapted from Bultreys et al., 2016)**

Even though Palabos simulations can be efficiently conducted in a parallel computing environment, still LBM modelling of fluid flow through complex pore space can be computationally expensive: 3D matrix with more than a 2.7 billion voxel (2321 x 1986 x 600) can equate to a matrix of around 52 billion data points since each voxel has 19 nodes in D3Q19 scheme (Kelly et al., 2016). Therefore, grid coarsening might be essential and time saving while admitting that some of the smaller pores on the order of the original resolution pixel will be lost during upscaling. Thus, since Palabos is equipped with a parallel computing environment, the fluid flow simulations were conducted, after grid coarsening process using a super-computer (OSCER) facility at University of Oklahoma.

Moreover, it is worth mentioning that there are be many other physical phenomena occurred at nanoscale pores which may impact fluid flow through those narrow pores (Kelly et al., 2016). However, for the purpose of this study, from SEM images with LBM simulations only intrinsic (*geometric)* permeability, which is a function of the geometric parameters of the constructed pore structure (porosity, pore size distribution, pore connectivity), is calculated. Thus, it can be expected that the calculated intrinsic permeability value may underestimate gas permeability for low pressure conditions since it does not consider slip flow and Knudsen diffusion effect at smaller pores.

### *5.2.2 Pore Connectivity – Euler Poincare characteristics*

Previous studies have suggested numerous ways to quantify pore connectivity in porous media. Although several other methods have been suggested to analyze pore connectivity and coordination number of 3D porous media, Euler Poincare characteristic (EPC) approach is considered as one of the reliable and simply model to characterize pore connectivity (Chi and Heidari, 2016; Jiang et al., 2011; Vogel, 2008; Vogel et al., 2010). With EPC exact number of the pores and throats cannot be calculated, instead the average coordination number of porous media can be implicitly estimated (Arns et al., 2001; Vogel et al., 2010). In this work, EPC approach is applied to quantify pore connectivity because of its simplicity to use on 3D pore structures. EPC is usually defined as number of object components, which is isolated pore structures in a 3D rock sample, N, minus the number of tunnels (redundant pore-system connections), C, plus the number of cavities (isolated solids within the pore space), H, which is zero in practice:

$$e_{3D} = N - C + H \tag{5.7}$$

**Figure 5.5** illustrates N, C and H for ideal solid objects and their respective calculated 3D EPC from **Eq. 5.7**; the higher the C value, the lower calculated EPC and the higher the connectivity will become.

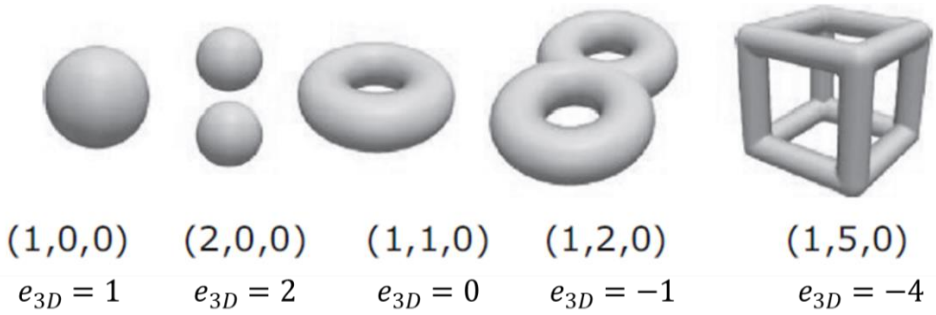


**Figure 5.5: Euler values for ideal solid objects (Wildenschild and Sheppard, 2013)**

For 3D system EPC can be estimated using parameters obtained from 2D slices as:

$$e_{3D} = \sum_{i=2}^{n} \frac{e_{2,i-1} + e_{2,i} - 2e_{2,i-1\cap i}}{2} \tag{5.8}$$

where $e_{2,i-1\cap i}$ represent 2D EPC calculated for overlapping of *i*th and (i-1)-th images. Chi and Heidari (2016) have suggested that, positive value of 3D EPC is an indication of poor pore connectivity, while negative value corresponds to the well-connected pore structure. The EPC as a function of sample size was estimated using ImageJ software ®.

## 5.3 Results

### *5.3.1 Static Properties*

Prior to fluid flow simulation and estimation of rock permeability, pore size distribution, 2D porosity, 3D total porosity, and connected porosity are computed as a function of sample size. Assuming cylindrical shape for the pores, the pore size distribution (PSD) are calculated for several images (Image #1, #50, #100, # 200, #300, #400, #500 and #600). As shown in **Figure 5.6**, it can

be observed that the number of pores decreases as pore size increases and for this particular sample more than 93% of the pores are less than 200 nm.

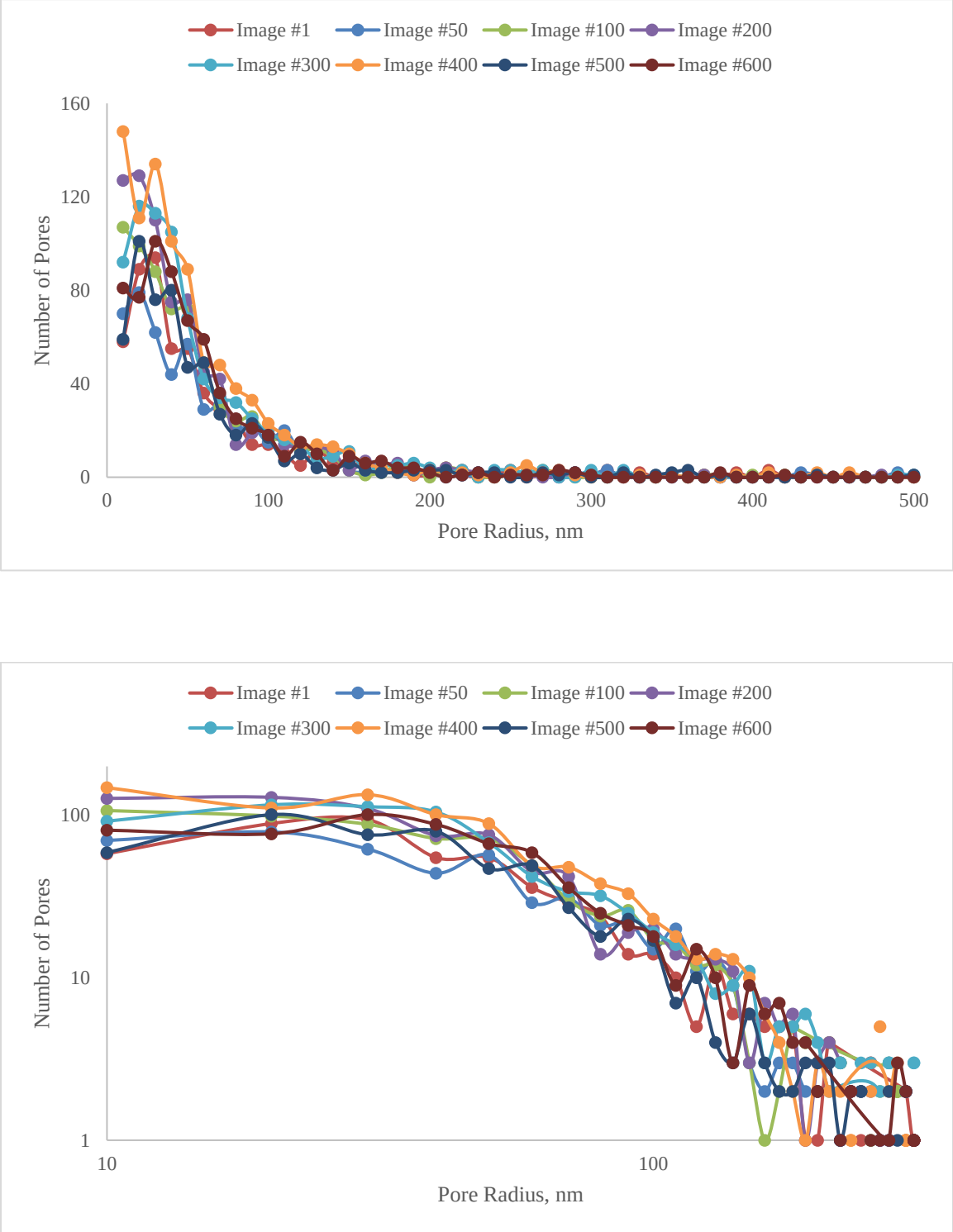


**Figure 5.6: Pore size distribution obtained from 2D slices for Eagle Ford sample**

Next, porosity values for the same 2D images are estimated and summarized in **Table 5.1**. Results indicate that, calculated porosity values are in the range of 12-17% for the first 300 images and it reduces significantly to the range of 6% for the last 200 images. More interestingly, although most of the pores (more than 93%) are less than 200 nm, the fraction of porosity with the pores smaller than 200 nm is only between 10% to 20%, while 80% to 90% percent of porosity is because of the contribution of pores larger than 200 nm. Thus, it can be suggested that while 7% of the pores with pore size bigger than 200 nm represents storage capacity, the rest of the 93% pores with less than 200 nm is significant for pore connectivity, and fluid transport.

**Table 5.1: Porosity obtained from 2D slices for Eagle Ford sample**

| ***Image #*** | ***1*** | ***50*** | ***100*** | ***200*** | ***300*** | ***400*** | ***500*** | ***600*** |
|---|---|---|---|---|---|---|---|---|
| *2D Porosity* | 0.128 | 0.149 | 0.162 | 0.159 | 0.147 | 0.112 | 0.063 | 0.064 |
| *Fraction of Pores (PSD < 200nm)* | 0.93 | 0.95 | 0.95 | 0.96 | 0.95 | 0.96 | 0.94 | 0.96 |
| *Fraction of Pores (PSD > 200nm)* | 0.07 | 0.05 | 0.05 | 0.04 | 0.05 | 0.04 | 0.06 | 0.04 |
| *Fraction of 2D Porosity (PSD < 200nm)* | 0.105 | 0.095 | 0.094 | 0.108 | 0.128 | 0.181 | 0.200 | 0.272 |
| *Fraction of 2D Porosity (PSD > 200nm)* | 0.895 | 0.905 | 0.906 | 0.892 | 0.872 | 0.819 | 0.800 | 0.728 |

Finally, total and connected porosity obtained from 3D pore structure is calculated as a function of sample size (stacked 3D images). As illustrated in **Figure 5.7**, results have shown that total porosity obtained from 3D images is around 15% when sample size is less than 4 μm and reduces slightly to the range of 12.5% when sample size is about 6 μm. This is expected because 2D porosity of images decreases with the size of samples that leads to smaller total porosity as shown in **Figure 5.7**. When connected porosity is evaluated, the estimated values are in the range of 11 to 14% for sample size of 2 μm and significantly decreases to the range of 6% when the sample size is 6 μm.

When 2D porosity, pore size distribution, 3D total and connected porosity are all compared, it can be concluded that the results are consistent; 3D total and connected porosity values decrease while the number of smaller pores increase as a function of sample size (**Figure 5.8**). Thus, it is logical to expect that there will be a significant permeability reduction with increasing the sample size that will be evaluated with LBM simulations and will be discussed in the next section.

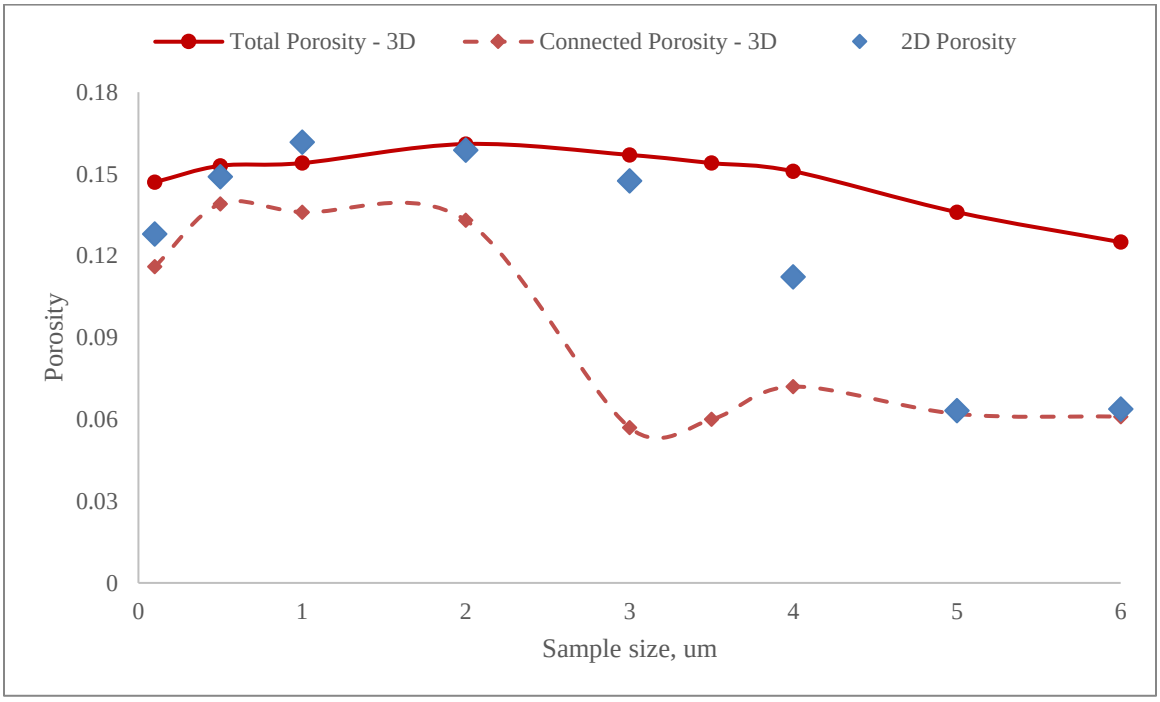


**Figure 5.7: 3D total and connected porosity for Eagle Ford sample as a function of sample size**

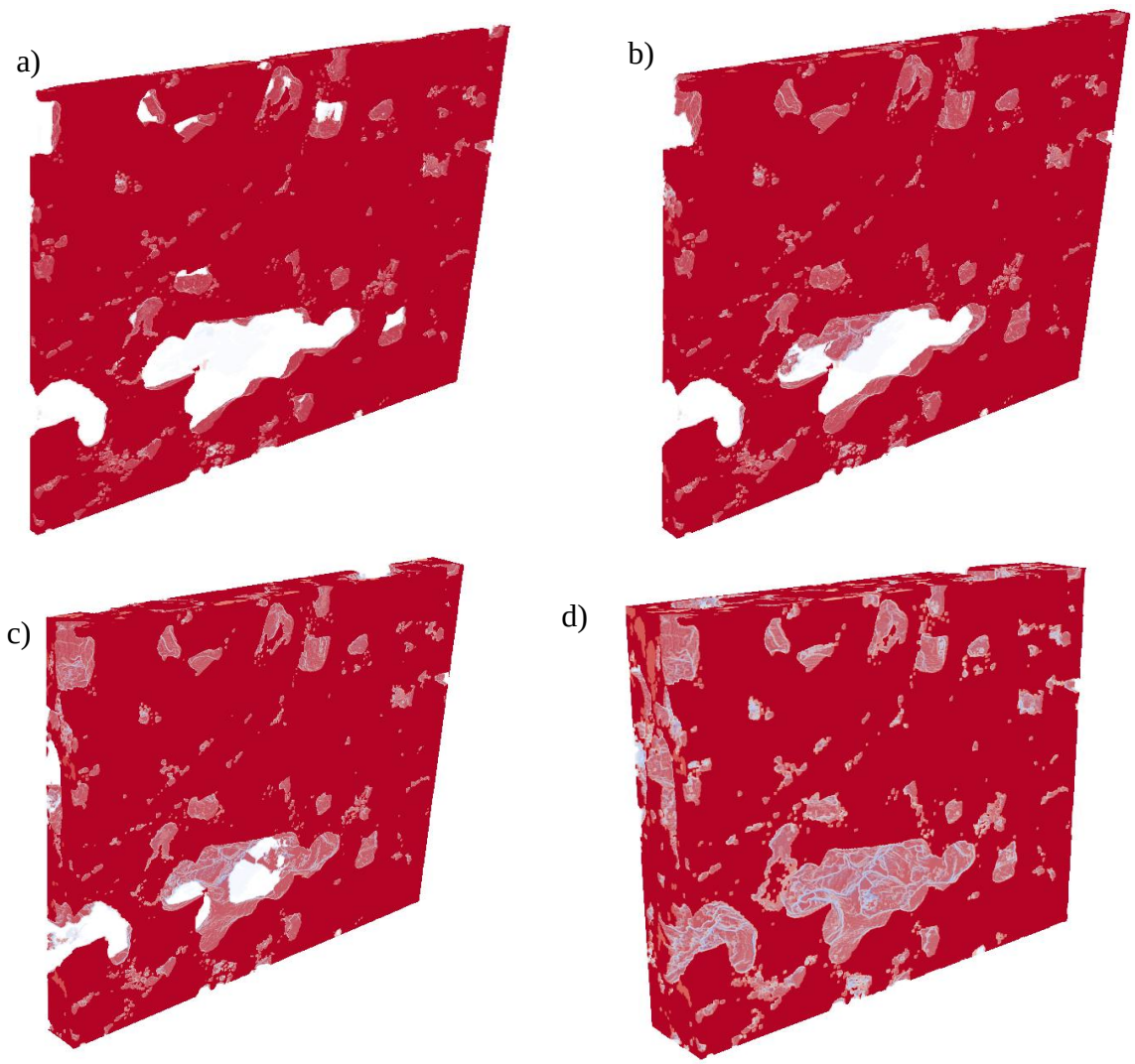


**Figure 5.8: 3D view of Eagle Ford shale sample for a) 1 μm b) 2 μm c) 3 μm d) 4 μm**

### *5.3.2 LBM Simulation Results*

As discussed in the previous sections, fluid flow and permeability is evaluated using LBM simulations to understand the interplay between pore connectivity loss and permeability reduction. Before further analysis and evaluation of the shale sample, first the accuracy of the LBM simulation is validated by comparing the simulation results with analytical solution for simple and ideal geometry representing bundle of tubes model. In the next step of verification, the simulation

results are compared with experimentally measured permeability values for Berea sandstone sample with micro-CT images obtained from literature (Dong 2007).

**Validation with bundle of tubes model**: Simple and ideal bundle of tubes model is created with 4 identical straight tubes with their radius of 10.7 pixels and total porosity of 40% as shown in **Figure 5.8a**. Analytically, permeability from straight tubes can be calculated as:

$$k = \frac{r^2}{8} \cdot \frac{n\pi r^2}{W^2} = \frac{r^2 \phi}{8} \tag{5.8}$$

where $r$ is the radius of tubes, $n$ is the number of tubes, and $W$ is the with of the system, which is 60 pixels in this example. Thus based on **Eq. 5.8**, the permeability is calcuted to be 5. 73 pixel$^2$ compared with LBM simulations result of 5.72 pixel$^2$, more than 99% accuaracy. Moreover, as expected, velocity magnitude is higher in the middle of the pores because of laminar flow and zero velcoity at the walls (no-slip baundary condition) assumptions as illustared in **Figure 5.9b**.

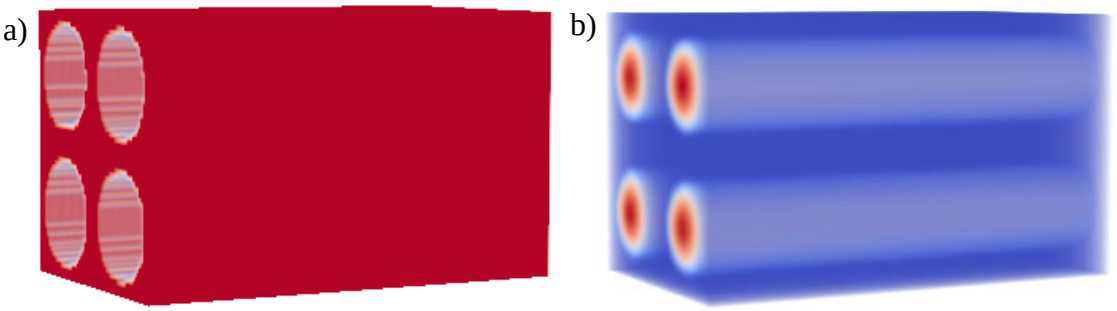


**Figure 5.9: LBM Simulation through bundle of tubes a) initial structure b) fluid velocity profile**

**Validation with Berea sandstone sample**: After validating with analytical solution for ideal system, further evaluation has been conducted for Berea sandstone sample with experimentally measured permeability values and micro-CT images obtained from the Petroleum Engineering and Rock Mechanics group at Imperial College London (Dong and Blunt, 2007). This particular sample has 19.6% porosity with 1286 md measured permeability and it is composed of 400 micro-

CT stack images with the size of 400 x 400 pixels and the resolution of 5.345 μm/pixel. The matrix and pore structure of this studied sample is shown in **Figure 5.10** which has been constructed for LBM simulations.

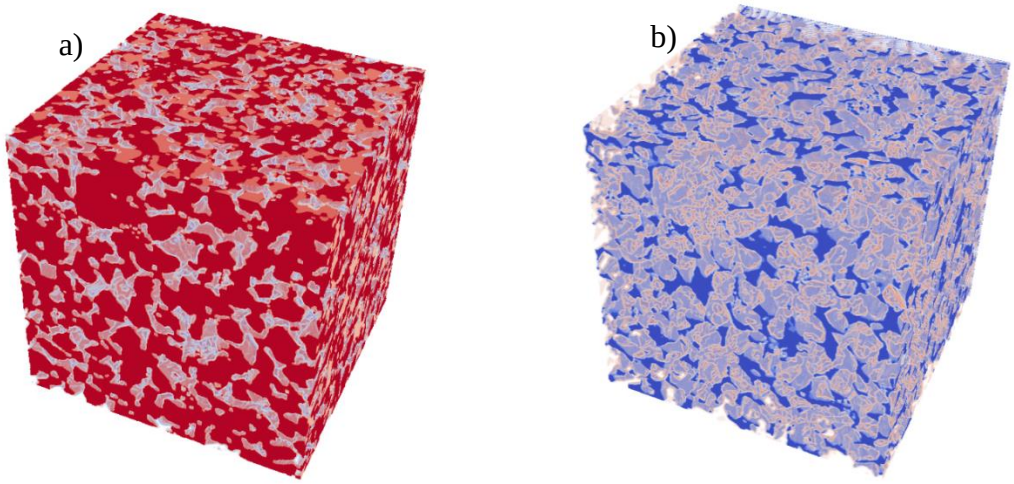


**Figure 5.10: 3D view of Berea sandstone a) matrix b) pore**

After conducting simulations, permeability results obtained from LBM has been converted from lattice units to physical units by multiplying with square of image resolution. Permeability calculated from LBM simulations is around 1342 md, comparable with experimentally measured of 1286 md. The relative velocity profile obtained from simulations is illustrated in **Figure 5.11.** It can be observed that the pores are extremely well connected, expected for this high porosity, high permeability sample. Moreover, the EPC parameter estimated for this sample is around -2000, which is indicator of a greater number of pore tunnels (C from **Eq. 5.7**) than number of pore structures (N from **Eq. 5.7**), representing a well-connected pore structure.

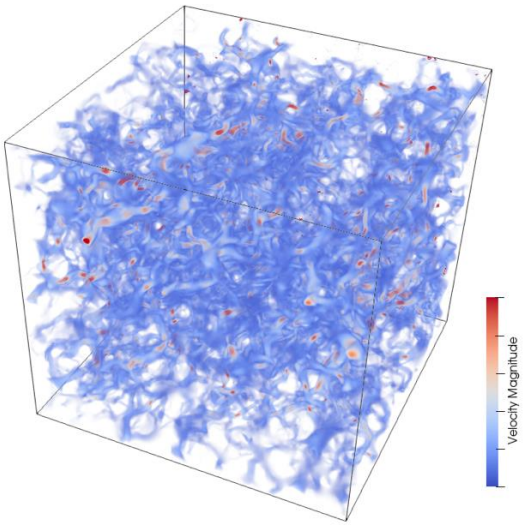


**Figure 5.11: Velocity magnitude through pore structure Berea sandstone**

**Results for Eagle Ford shale sample**: After validating with analytical solutions and experimental results, further simulations are conducted to estimate permeability for Eagle Ford shale sample. The matrix and pore structure of the whole sample (23.2x19.9x6 μm) is shown in **Figure 5.12**.

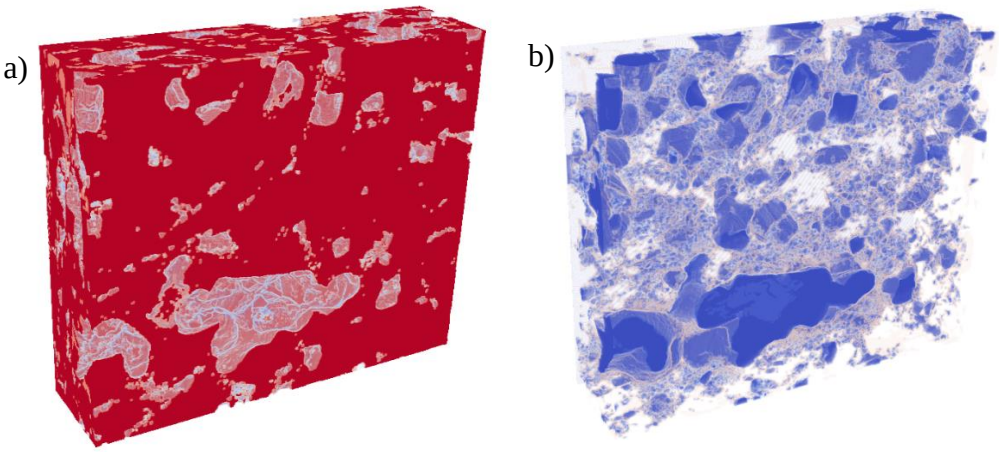


**Figure 5.12: 3D view of Eagle Ford shale sample a) matrix b) pore**

The calculated permeability from LBM simulations is around 1.17 μd, consistent with the literature (Driskill et al., 2013; Walls and Break, 2011) and also it is an expected result for this shale sample because of its comparable high porosity. The velocity profile obtained from LBM simulations is shown in **Figure 5.13**. As it can be observed, the connections between pores are very limited

resulting a very low permeability. Meantime, the EPC value calculated for the whole sample is around 9431, suggesting a very poor pore connectivity.

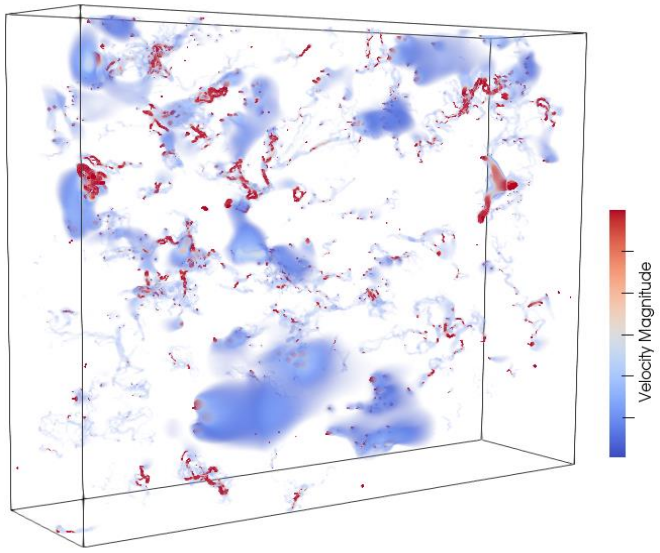


**Figure 5.13: Velocity magnitude through pore structure of Eagle Ford sample**

Next, permeability and pore connectivity are further analyzed as the sample size increases. As discussed before, for this sample although reduction in total porosity is not significant but the connected porosity significantly decreases as the sample size increases. Similarly, when permeability is estimated as sample size increases, the results indicate that there is substantial decline from 17.62 md when the sample size is only 1 μm (100 images) to 1.17 μd when the sample size is 6 μm, which corresponds to more than 15000 times reduction (**Figure 5.14).** It should be noted that this huge reduction is not only because of the pore connectivity effect, but also because of pore and/or pore throat sizes that contributes to fluid flow at different scales. As it can be seen from **Figure 5.7**, fluid can flow through the biggest pores in the system since they are well connected when sample size is below 3 μm, while these pores are restricted with much smaller pore throats when sample size is bigger than 4 μm. However, reducing pore (throat) size is not the only factor that affects permeability. Similarly, when pore connectivity defined with EPC is

calculated for each sample size, it is observed that all calculated values are consistent with the permeability results as sample size increases (**Figure 5.15**). All results have been summarized in **Table 5.2**.

Finally, when connected porosity fraction $(\phi_{conn}/\phi_{total})$, normalized connected porosity $(\phi_{conn}/\phi_{conn_max})$, permeability and EPC connectivity are analyzed together, a similar and consistent trend can be observed. Moreover, it can be suggested that, based on results from all parameters, REV for this particular sample is around 4 μm (**Figure 5.15)**.

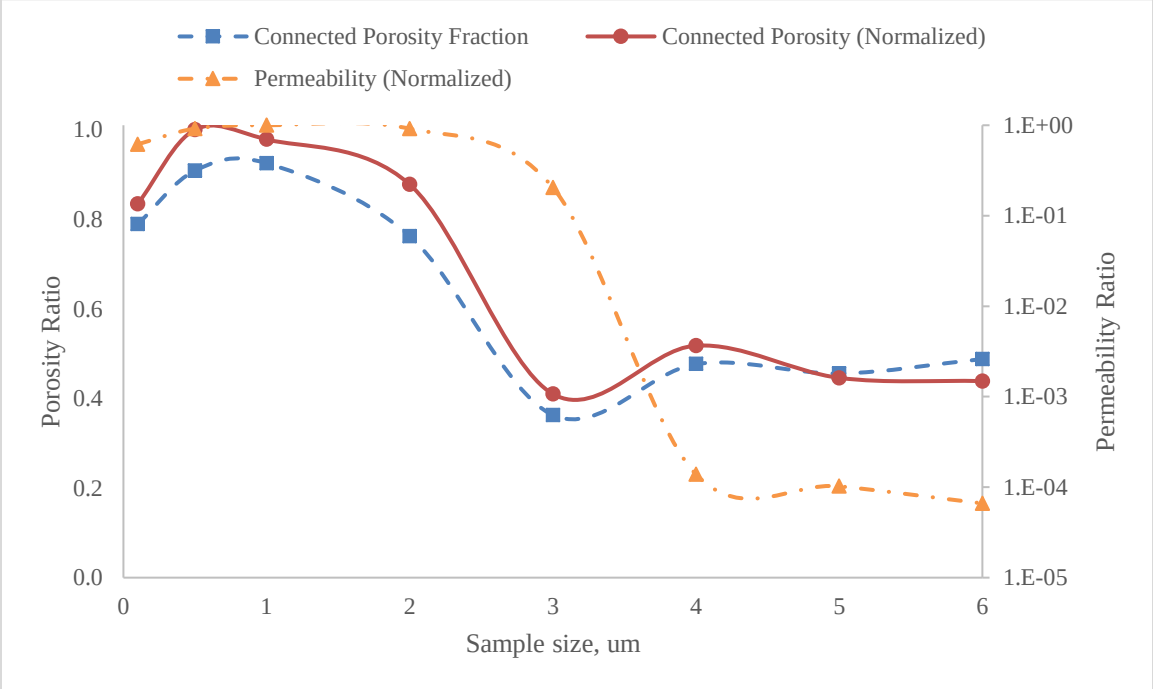


**Figure 5.14: Connected porosity and permeability as a function of sample size for shale sample**

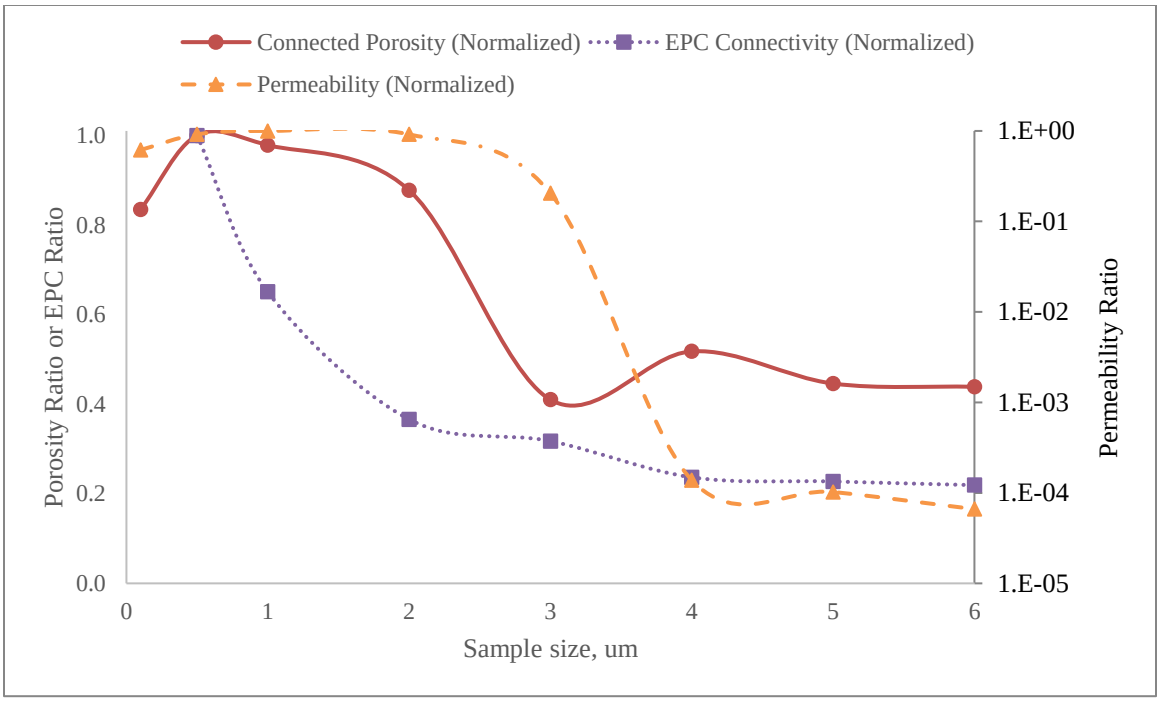


**Figure 5.15: Connected porosity, permeability, and EPC connectivity as a function of sample size for shale sample**

**Table 5.2: Summary of results for Eagle Ford sample as a function of sample size**

| *Sample Size, μm* | *Total Porosity* | *Connected Porosity* | $\phi_{con}/\phi_{con_max}$ | *K, μd* | $K/K_{max}$ | *EPC* | $EPC_{max}/EPC$ |
|---|---|---|---|---|---|---|---|
| *0.5* | 0.153 | 0.139 | 1.00 | 16155.2 | 0.92 | 2068 | 1.00 |
| *1* | 0.147 | 0.136 | 0.98 | 17618.1 | 1.00 | 3177 | 0.65 |
| *2* | 0.16 | 0.122 | 0.88 | 16134.0 | 0.92 | 5648 | 0.37 |
| *3* | 0.157 | 0.057 | 0.41 | 3604.2 | 0.21 | 6512 | 0.32 |
| *4* | 0.151 | 0.072 | 0.52 | 2.44 | 1.4E-4 | 8735 | 0.24 |
| *5* | 0.136 | 0.062 | 0.45 | 1.80 | 1.0E-4 | 9091 | 0.23 |
| *6* | 0.125 | 0.061 | 0.44 | 1.17 | 6.6E-5 | 9431 | 0.22 |

## 5.4 Conclusions

In this chapter, 3D pore structure of an Eagle Ford shale sample constructed by stacking 600 SEM images is analyzed to understand the impact of pore connectivity on permeability reduction as a function sample size. First, static pore structure parameters are studied and then LBM simulations

are conducted to model steady state, laminar fluid flow through constructed 3D pore space. The main conclusions can be summarized as follows:

- Total porosity of studied Eagle ford shale sample is around 12.5 % which reduces slightly with increasing sample size. On the other hand, the connected porosity of the system decreases more than 50% when sample size is around 6 μm.
- Permeability calculated from LBM simulations is around 1.17 μd for whole sample; moreover, the calculated permeability value is also a strong function of sample size; i.e. 15000 times reduction when sample size is at 6 μm.
- Finally, pore connectivity estimated from EPC is negative for sandstone sample which is an indicator of high pore connectivity and positive for all shale sample sizes which is an indicator of poor pore connectivity. Moreover, consistent with the connected porosity and permeability results, pore connectivity significantly decreases with increasing sample size.

# Chapter 6 – Accessible Porosity based on MICP

## 6.1 Introduction

This chapter addresses **Obj. 4** where a novel approach is proposed to correct accessible porosity values calculated using mercury injection capillary pressure (MICP) for shale samples. MICP is one of the most widely used experimental techniques. One of the major advantages of MICP test us that they give direct information about pore throats which is the key parameter for connectivity/conductivity (King et al., 2015). Traditionally, volume of mercury recorded during MICP test is corrected to consider for conformance. Conformance is the amount of mercury needed to envelope the external shape of a sample before intrusion happens and it is a function of sample shape irregularities and sample size.

In addition to conformance correction, following Bailey (2009) and Comisky et al., (2011) has suggested to consider intrusion correction (pore compression correction). They suggested to determine volume of mercury recorded during compression stage (until intrusion/entry pressure) and subtract that amount from total volume. However, simply subtracting volume of mercury measured during compression stage is not an accurate way, because in this mode: 1) grain compression is not considered, 2) during compression stage both accessible and inaccessible pores are compressed simultaneously, which in correction only inaccessible pore compression should be considered, and 3) inaccessible pore compression should be considered not only during compression stage but until the final pressure (Davudov et al., 2018a).

Recently, Peng et al., (2017) has suggested to considered conformance correction and grain compressibility effect on accurate estimation of porosity from MICP data. However, in this study also, contribution of inaccessible pore compressibility has not been considered. Though it is also crucial to correct for compression of inaccessible pores, since inaccessible pore volume

compaction has been observed and reported around the unfilled regions of samples (Giesche, 2006; Yao and Liu, 2012). The fraction of inaccessible/unfilled pores will strongly depend on the rock pore network and as well as fluid type; unsaturated part of the rock will be affected because of the pore throats smaller than 3 nm which mercury cannot intrude.

Therefore, three distinct corrections are suggested which are essential for accurate estimation of accessible porosity from MICP data: (1) conformance, (2) grain compression, (3) inaccessible pore compression. In this chapter mathematical model is developed to predict pore volume compressibility and accessible porosity from MICP data and next results for Barnett, and Haynesville samples are compared and evaluated.

## 6.2 Mathematical Model

In this section, a new model is proposed to estimate pore and grain compressibility from MICP data and correct calculated accessible porosity while considering above-mentioned corrections.

### *6.2.1 Pore Compressibility Calculation*

Bailey (2009) have suggested that Due to the extremely limited pore connectivity and sub-micron pore radii, during MICP test, shale samples will observe three different stages; conformance, compression, and intrusion; pore volume compressibility can be determined based on mercury volume recorded during compression stage.

When pressure reaches to conformance pressure ($P_{cf}$), the volume of mercury recorded is due to core sample conformance that needs to be corrected for accurate pore volume calculations. For pressure values larger than conformance pressure yet smaller than critical intrusion/entry pressure ($\mathrm{P_{int}}$), pressure value is not sufficient for mercury to intrude into samples. However, in this stage pores and grains are compressed owing to effective pressure and mercury volume recorded at this stage is the sum of the volume change due to pore and grain shrinkage.

Mercury intrusion to accessible pores starts to happen after pressure gets to $P_{int}$, since intrusion is the point at which the capillary pressure exceeds the critical entry value. At intrusion pressure and beyond, mercury begins filling the rock pore volume and when pressure reaches to final pressure ($P_f$), all accessible pores with pore throats larger than 3 nm have been intruded.

Thus, compression of inaccessible pores has not been considered in Bailey's model and furthermore, grain compressibility is assumed to be negligible. However, Dang et al., (2017) proposed that grain compressibility in shale formations cannot be ignored suggesting that during compression stage only bulk compressibility can be estimated.

Recently, Lan et al., (2017) proposed a new dual compressibility model to estimate pore compressibility from MICP data. The model suggests a division of the pore space of the sample based on MICP entry pressure, and then incorporation of the inaccessible pores into the grain volume of the material; pore volume is separated as accessible pore and inaccessible part of the rock and their compressibility values are calculated as two different and independent entities.

In this study, a new model is proposed, which is modified version of Lan et al., (2017) models. Dissimilar to Bailey's model, in this model, during compression stage accessible pores, inaccessible pores and grain are compressed simultaneously; i.e., as suggested by Dang et al., (2017), bulk compressibility can be calculated from this stage. Moreover, single pore compressibility value is considered for both accessible and inaccessible pores, while also grain compressibility is included in calculations. For a thourough comparison of different methods, please refer to Lan et al., (2017) and Davudov et al., (2018b).

When pressure reaches critical threshold the mercury intrusion starts, and accessible pores are filled with mercury, yet inaccessible pores and grain still get compressed until final pressure **(Figure 6.1)**.

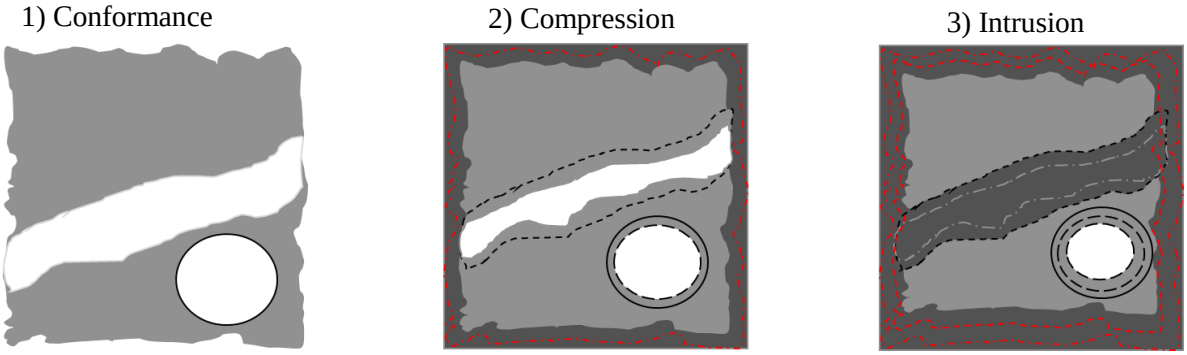


**Figure 6.1: Three stages during MICP experiment.**

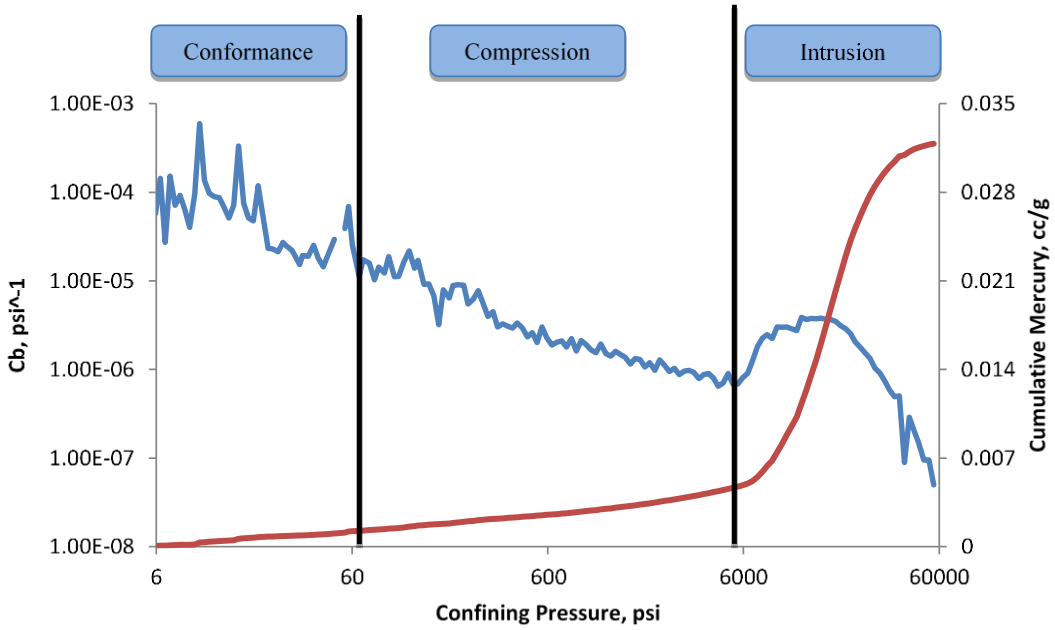


**Figure 6.2: MICP curve divided into 3 stages. Blue curve is calculated bulk compressibility while red curve corresponds to cumulative mercury volume (Lan et al., 2017).**

As suggested by Bailey (2009) compressibility of tight formations can be expressed as a power law function with respect to pressure, thus, compression stage can be determined as linear line from log-log plot of incremental mercury volume change with respect to pressure. Any deviation from linear line is either due to conformance on low pressure portion or due to intrusion at high pressure region. **Figure 6.2** displays various stages that a shale sample undergoes during MICP test.

Based on the above discussions, bulk compressibility is estimated using data acquired during compression stage and decomposed to separately calculate both grain and pore compressibility values. The main assumptions of this model are as follow:

- There is no mercury intrusion into pores until injection pressure exceeds entry pressure.
- Both pore and grain compressibility can be expressed as power law function with respect to confining pressure.
- Porosity measured with crushed sample low-pressure pycnometer method is considered as absolute total porosity.

The bulk volume of the rock sample can be expressed as the sum of grain and total pores including both accessible pore, and inaccessible pore:

$$V_b = V_p + V_g \tag{6.1}$$

where $V_b$ represents bulk volume, $V_p$ is the volume of total pores, and $V_g$ is the volume of grain. Relationship between compressibility terms with respect to confining pressure can be expressed as follow (Zimmerman et al., 1986):

$$C_b = \phi_{LPP} C_p + C_g \tag{6.2}$$

where $C_b, C_p$ and $C_g$ represent compressibility of the bulk, pore and grain respectively, and $\phi_{LPP}$ is total porosity including both accessible and inaccessible pores. If it is assumed that compressibility can be expressed as a power law function with respect to pressure, **Eq. 6.2** can be rewritten as:

$$k_{\mathrm{b}} P^m = \phi_{LPP} k_{\mathrm{p}} \mathrm{P}^m + k_{\mathrm{g}} P^m \tag{6.3}$$

where $k_{\mathrm{b}}$, $k_{\mathrm{p}}$, and $k_{\mathrm{g}}$ are the coefficients in the power law function for bulk, pore, and grain respectively. It is further assumed that the exponent of power law function, $m$, is same for bulk,

pore, and grain compressibility values. For more discussion about exponent, $m$, please read Davudov et al., (2018b).

As discussed earlier, linear trend from log-log plot of incremental mercury volume change vs. pressure (**Figure 6.2**) is used to identify compression stage and calculate bulk compressibility. Thus $k_{\mathrm{b}}$ and m can be determined. However, to estimate other two unknowns ($k_{\mathrm{p}}$, and $k_{\mathrm{g}}$) two equations are needed, which **Eq. 6.3** can be considered as the first equation.

Additionally, when injection pressure reaches to intrusion pressure (end of compression stage), all accessible pore, inaccessible pore and grain are compressed without any mercury intrusion into pores. At this stage volume of mercury recorded is due to only conformance and sample compression and it can be expressed as:

$$V_{Hg}\,(P_{int}) = \left[V_{pi} - V_p\,(P_{int})\right] + \left[V_{gi} - V_g(P_{int})\right] + V_{\mathrm{cf}} \tag{6.4}$$

where $V_{pi}$ is pore volume at initial stage, $V_{gi}$ is grain volume at initial stage, $V_{Hg}$ is the volume of mercury recorded at specific pressure, and $V_{cf}$ is volume of mercury needed to envelope the external surface of the sample (conformance correction). Volume of pores or grain at given pressure can be calculated based on compressibility equation as:

$$\int_{P_i}^{P} -\frac{dV}{V} = \int_{P_i}^{P} C\,dP = \int_{P_i}^{P} kP^m dP \tag{6.5}$$

After integrating **Eq. 6.5**, volume of the pores at specific pressure can be written as:

$$V(\mathrm{P}) = \frac{V}{\exp\left(\frac{k}{m+1}\left(P^{m+1} - P_i^{m+1}\right)\right)} \tag{6.6}$$

By combining **Eq. 6.4** with **Eq. 6.6,** volume of mercury recorded at intrusion pressure (end of compression stage) can be rewritten as:

$$V_{Hg}\,(P_{int}) = V_{pi} - \frac{V_{pi}}{\exp\left[\frac{k_{\mathrm{p}}}{m+1}(P_{int}^{m+1} - P_i^{m+1})\right]} + V_{gi} - \frac{V_{gi}}{\exp\left[\frac{k_{\mathrm{g}}}{m+1}(P_{int}^{m+1} - P_i^{m+1})\right]} + V_{\mathrm{cf}} \tag{6.7}$$

**Eq. 6.3** and **6.7** are solved simultaneously to calculate both pore and grain compressibility values separately. Note that, it is often found that conformance pressure is close to initial pressure (atmospheric pressure), thus it is reasonable to assume that $\frac{k_{\mathrm{p}}}{m+1}(P_{cf}^{m+1} - P_i^{m+1})$ approximates zero.

### *6.2.2 Accessible Pore Calculation*

Based on the proposed compressibility model for accurate estimation of accessible pore volume from MICP test, three different corrections are needed: conformance, grain compressibility and inaccessible pore compressibility. For conformance correction, the volume of mercury recorded at conformance pressure, $P_{\mathrm{conf}}$ is simply subtracted from total volume measured. After conformance correction, accessible pore volume needs to be further corrected due to compression of grain and inaccessible pore:

$$V_a = V_{Hg}\,(P_f) - V_{cf} - [V_{ina}\,(P_i) - V_{ina}\,(P_f)] - [V_g\,(P_i) - V_g\,(P_f)], \tag{6.8}$$

where $V_a$ is volume of accessible pores, and $V_{ina}$ is volume of inaccessible pores. Setting accessible porosity, $\frac{V_a}{V_b}$ as $\phi_a$, and inaccessible porosity $\frac{V_{ina}}{V_b}$ as $(\phi_{LPP} - \phi_a)$ then **Eq. 6.8** can be rewritten to express corrected accessible porosity calculated as:

$$\phi_a V_{bi} = V_{Hg}(P_f) - \underbrace{V_{cf}}_{\textit{Conformance Correction}} - \underbrace{\left[(\phi_{LPP} - \phi_a)V_{bi}\left(1 - \frac{1}{\exp\left(\frac{k_p}{m+1}\left(P_f^{m+1} - P_i^{m+1}\right)\right)}\right)\right]}_{\textit{Inaccessible Pore Compression}} - \underbrace{\left[(1-\phi_{LPP})V_{bi}\left(1 - \frac{1}{\exp\left(\frac{k_g}{m+1}\left(P_f^{m+1} - P_i^{m+1}\right)\right)}\right)\right]}_{\textit{Grain Compression}} \tag{6.9}$$

**Eq. 6.9** can be solved to calculate accessible porosity, $\phi_a$ which includes corrections due to conformance, grain compression, and inaccessible pore compression.

## 6.3 Results and Discussion

In this study, samples from Barnett, and Haynesville plays (11 each) are selected for accessible porosity calculations. All MICP measurements for shale samples have been conducted by Unconventional Shale Gas Consortium at University of Oklahoma. Barnett and Haynesville shale plays have their own characteristics when it comes into pore distribution; the porosity in the Barnett is dominantly within the organic matter (Curtis et al., 2012b; Davudov et al., 2016) where the porosity in the Haynesville shale is most prevalent in the inorganic part (Chalmers et al., 2012; Curtis et al., 2012a). Porosity values denoted as $\boldsymbol{\phi_{Hg}}$ represents calculated values from MICP test before any corrections i.e., total measured volume of mercury is assumed to be due to pore filling. Additionally, $\boldsymbol{\phi_{cf}}$, $\boldsymbol{\phi_g}$, $\boldsymbol{\phi_a}$ expresses porosity values calculated from MICP data with conformance correction only, both conformance and grain compression corrections and with all three corrections (conformance, grain compression and inaccessible pore compression), respectively.

### *6.3.1 Pore Compressibility Results*

Pore compressibility values, expressed in terms of pressure as $C_p = k_p P^m$, are calculated and analyzed for all samples studied. Average value of $k_p$ is 0.0021, and 0.0014 and average value of m is -0.75, and -0.69 for Barnett, and Haynesville samples, respectively. As shown in **Figure 6.3** results indicate that pore compressibility values are higher than anticipated values in the range of 1E-5 1/psi for shale samples at lower pressure. When pressure reaches to 6000 psi, pore compressibility reduces to the range of 1E-6 1/psi in most of the cases. Pore compressibility values for 11 Barnett samples show relatively close outcomes; likewise, results obtained from Haynesville samples with two exceptions are similar and comparable to those of Barnett as well (**Figure 6.3**).

Additionally, grain compressibility expressed in terms of confining pressure as, $C_g = k_g P^m$, is illustrated in **Figure 6.4**. Average value of $k_g$ is 7.2E-5, and 6.0E-5 for Barnett and Haynesville formations, respectively. Results show that at initial pressure grain compressibility is mostly in the range of 1E-6 1/psi, where it drops to the range of 1E-8 1/psi at higher pressure. **Table 6.1** summarizes all parameters of power law functions for both compressibility terms.

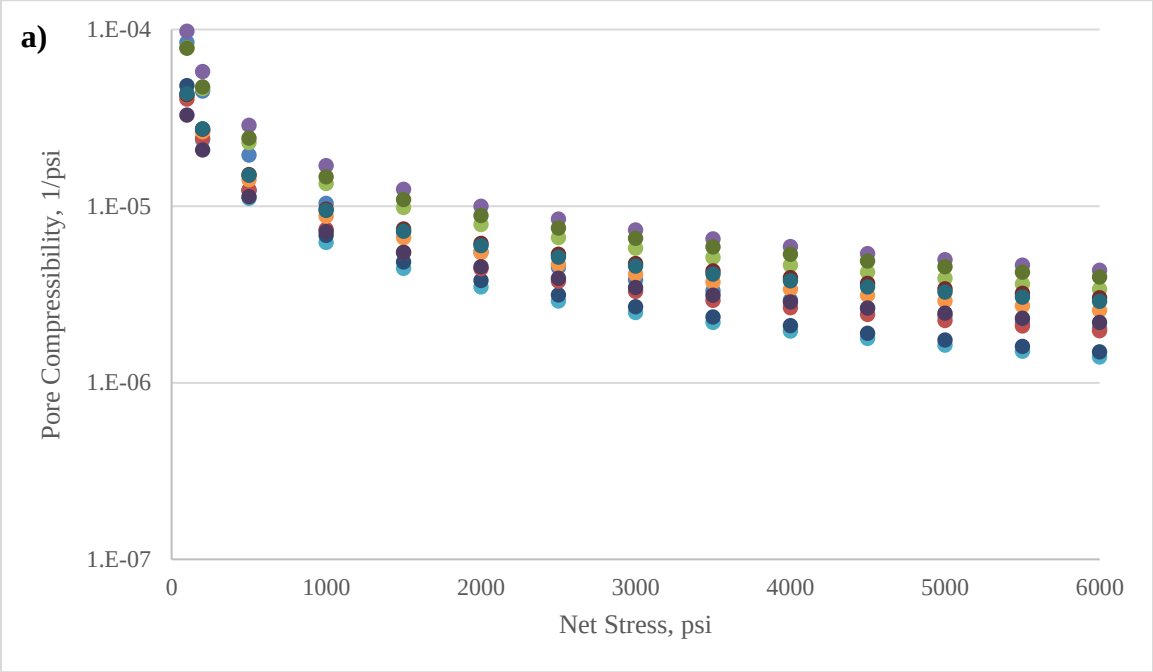

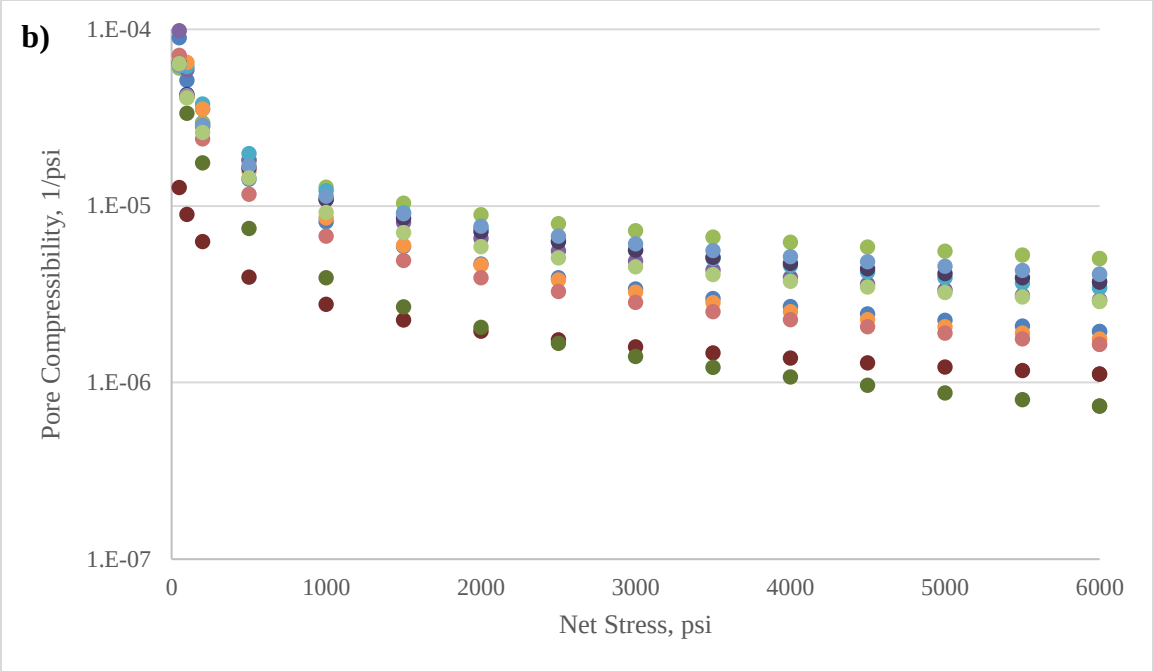


**Figure 6.3: Pore compressibility for a) Barnett b) Haynesville**

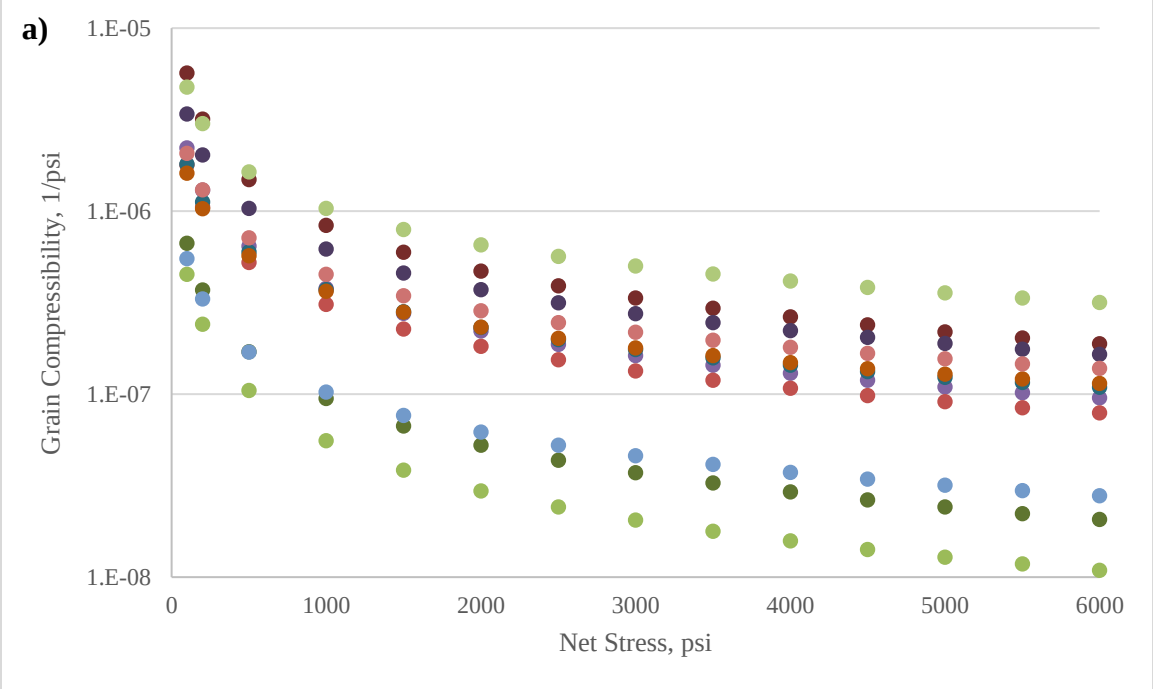

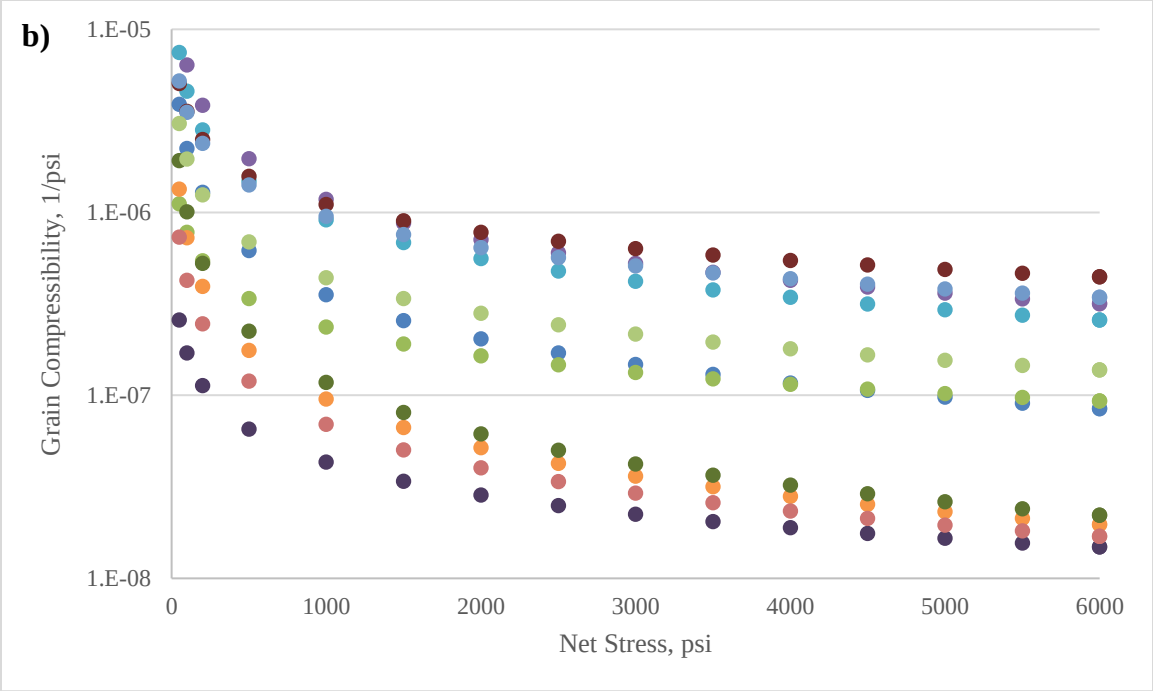


**Figure 6.4: Grain compressibility for a) Barnett b) Haynesville**

**Table 6.1: Parameters of power law fit function of pore and grain compressibility**

| | *Barnett* | | | *Haynesville* | | |
|---|---|---|---|---|---|---|
| ***Sample #*** | **m** | $k_p$ | $k_g$ | **m** | $k_p$ | $k_g$ |
| *1* | -0.91 | 5.6E-03 | 3.0E-05 | -0.80 | 2.05E-03 | 8.90E-05 |
| *2* | -0.77 | 2.7E-03 | 7.7E-05 | -0.52 | 4.58E-04 | 8.46E-06 |
| *3* | -0.76 | 3.3E-03 | 6.0E-05 | -0.73 | 1.74E-03 | 1.88E-04 |
| *4* | -0.83 | 1.9E-03 | 2.6E-04 | -0.70 | 1.57E-03 | 1.17E-04 |
| *5* | -0.85 | 2.4E-03 | 3.3E-05 | -0.88 | 3.77E-03 | 4.21E-05 |
| *6* | -0.74 | 1.2E-03 | 1.0E-04 | -0.51 | 9.28E-05 | 3.70E-05 |
| *7* | -0.69 | 1.0E-03 | 4.2E-05 | -0.93 | 2.44E-03 | 7.34E-05 |
| *8* | -0.65 | 8.3E-04 | 3.2E-05 | -0.60 | 6.69E-04 | 2.67E-06 |
| *9* | -0.73 | 2.2E-03 | 1.6E-05 | -0.57 | 5.77E-04 | 4.83E-05 |
| *10* | -0.66 | 6.9E-04 | 4.4E-05 | -0.79 | 1.55E-03 | 1.59E-05 |
| *11* | -0.66 | 9.1E-04 | 1.0E-04 | -0.65 | 8.05E-04 | 3.85E-05 |

### *6.3.2 Comparison with Ultrasonic Velocity Measurements*

Assuming isotropic core samples, bulk compressibility values can alternatively be estimated using measured shear velocity, $V_s$, compressional velocity and sample bulk density as (Dang et al., 2017; Davudov et al., 2018b):

$$C_b = \frac{1}{\rho\left(V_p^2 - \frac{4}{3}V_s^2\right)} \tag{6.10}$$

Bulk compressibility values obtained from MICP data is compared with the values calculated from velocity measurements for 4 samples as shown in **Figure 6.5**. Moreover, for two samples, both horizontal and vertical velocity measurements are conducted. Results indicate that bulk compressibility calculated from MICP data is overestimated at lower pressure range and slightly underestimated for higher pressure range when compared with values obtained from sonic measurements. This comparison can clearly be seen from **Figure 6.6**. The major reason for overestimation might be due to "no mercury intrusion into pores" assumption and results may differ based on methodology of first entry pressure determination. Further studies need to be conducted for accurate estimation of entry pressure during MICP test.

When bulk compressibility calculated from horizontal and vertical sonic data are compared, as expected values obtained from horizontal measurements (parallel to bedding) is significantly lower than that of vertical measurements (vertical to bedding), especially at lower pressure ranges.

a)

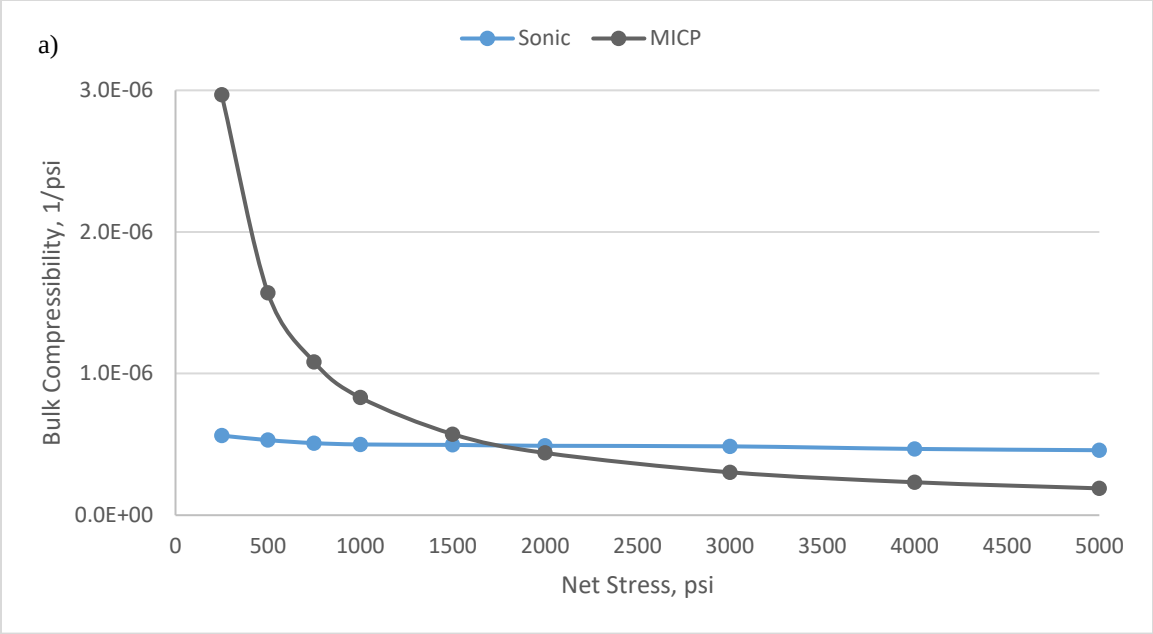
Sonic
MICP
3.0E-06
2.0E-06
1.0E-06
0.0E+00
Bulk Compressibility, 1/psi
0
500
1000
1500
2000
2500
3000
3500
4000
4500
5000
Net Stress, psi

b)

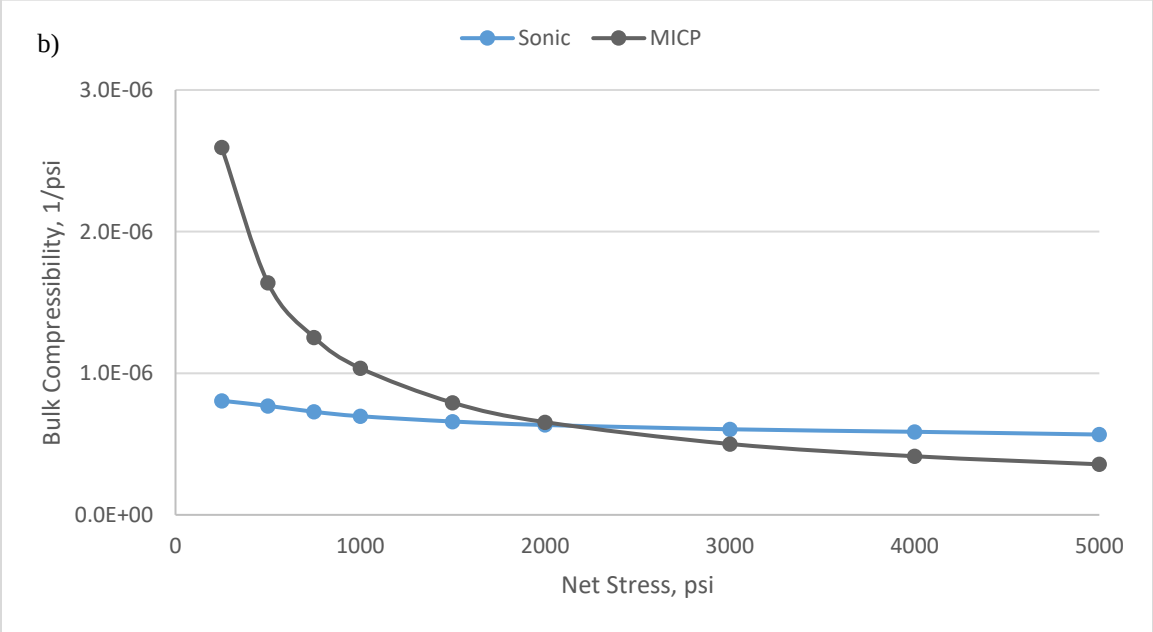
Sonic
MICP
3.0E-06
2.0E-06
1.0E-06
0.0E+00
Bulk Compressibility, 1/psi
0
1000
2000
3000
4000
5000
Net Stress, psi

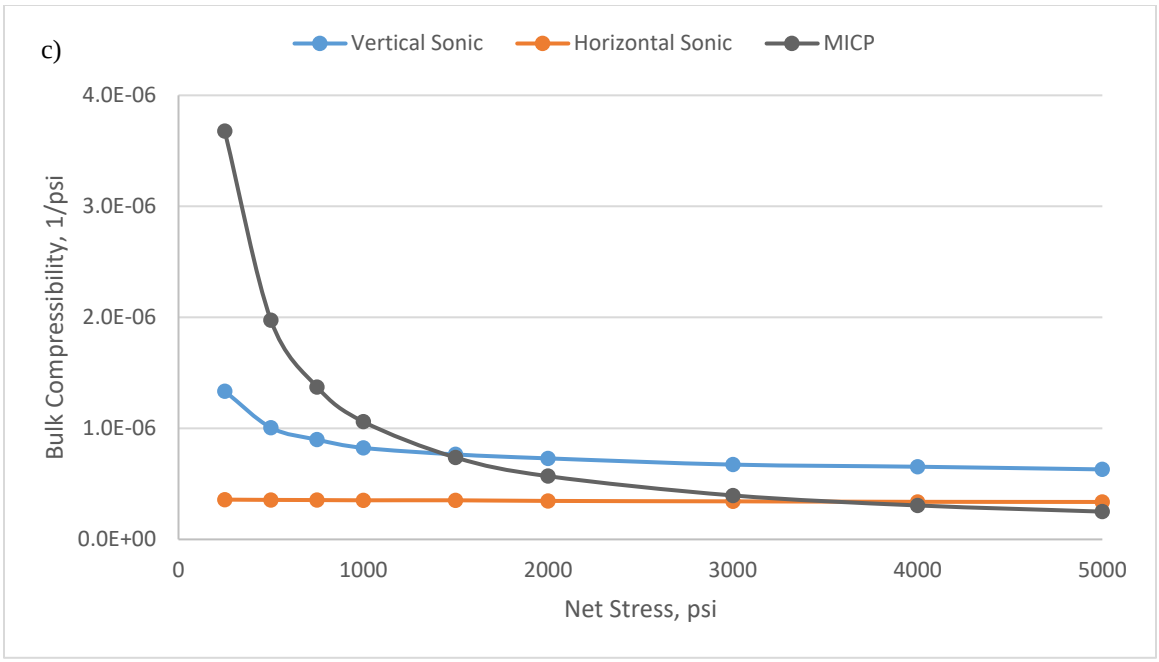


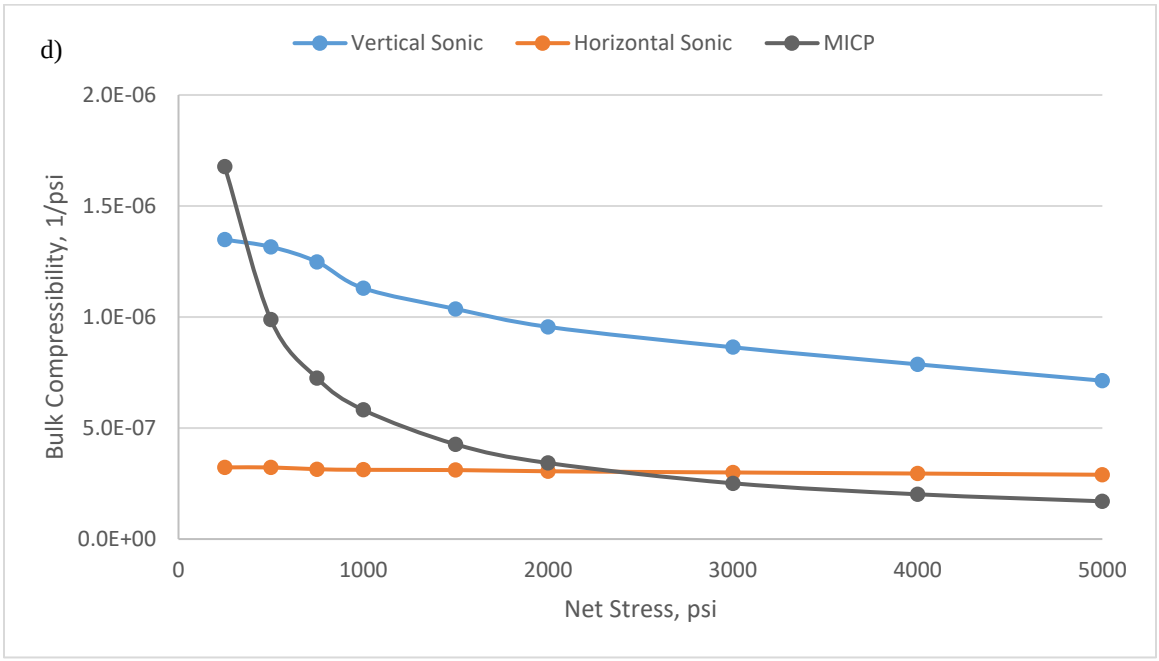


**Figure 6.5: Comparison of bulk compressibility calculated from MICP and velocity measurements for Haynesville samples a) H-2 b) H-3 c) H-4 d) H-5**

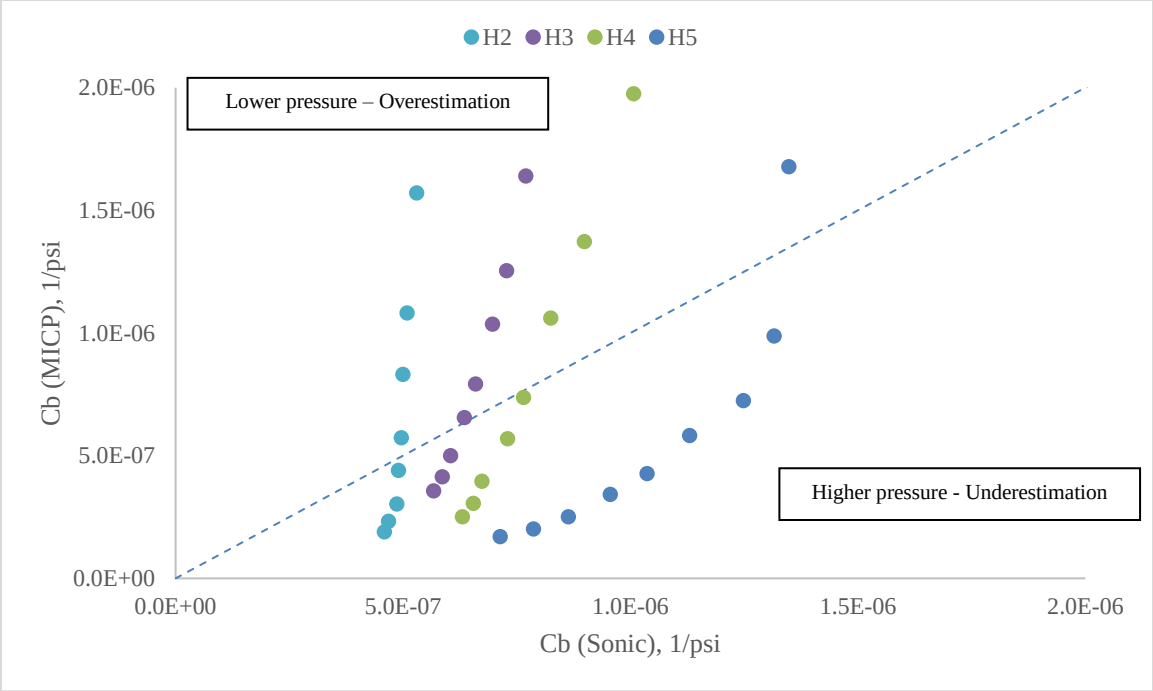


**Figure 6.6: Comparison of bulk compressibility calculated from MICP and velocity measurements**

*6.3.4 Accessible porosity*

Based on proposed model (**Eq. 6.9**) accessible porosity values are calculated and compared for both formations. **Figure 6.7** illustrates comparison of accessible porosity for 11 Barnett samples. Expectedly, accessible porosity, $\phi_a$ is less than total porosity, $\phi_{LPP}$ values measured from crush sample low-pressure pycnometer (LPP) method (**Figure 6.7a)**; also, it can be observed that the ratio of accessible pores to total porosity ($\phi_a/\phi_{LPP}$) increases with an increase in total porosity (**Figure 6.7b)**. This indicates that for Barnett samples, accessible pore fraction is positively related to total porosity. Moreover, results show that if corrections are not considered, porosity values calculated from MICP, $\phi_{Hg}$ will be overestimated (**Figure 6.7c)**. This difference occurs owing to implementation of all three corrections including conformance, grain compressibility, and inaccessible pore compressibility. The results for Barnett samples are summarized in **Table 6.2**.

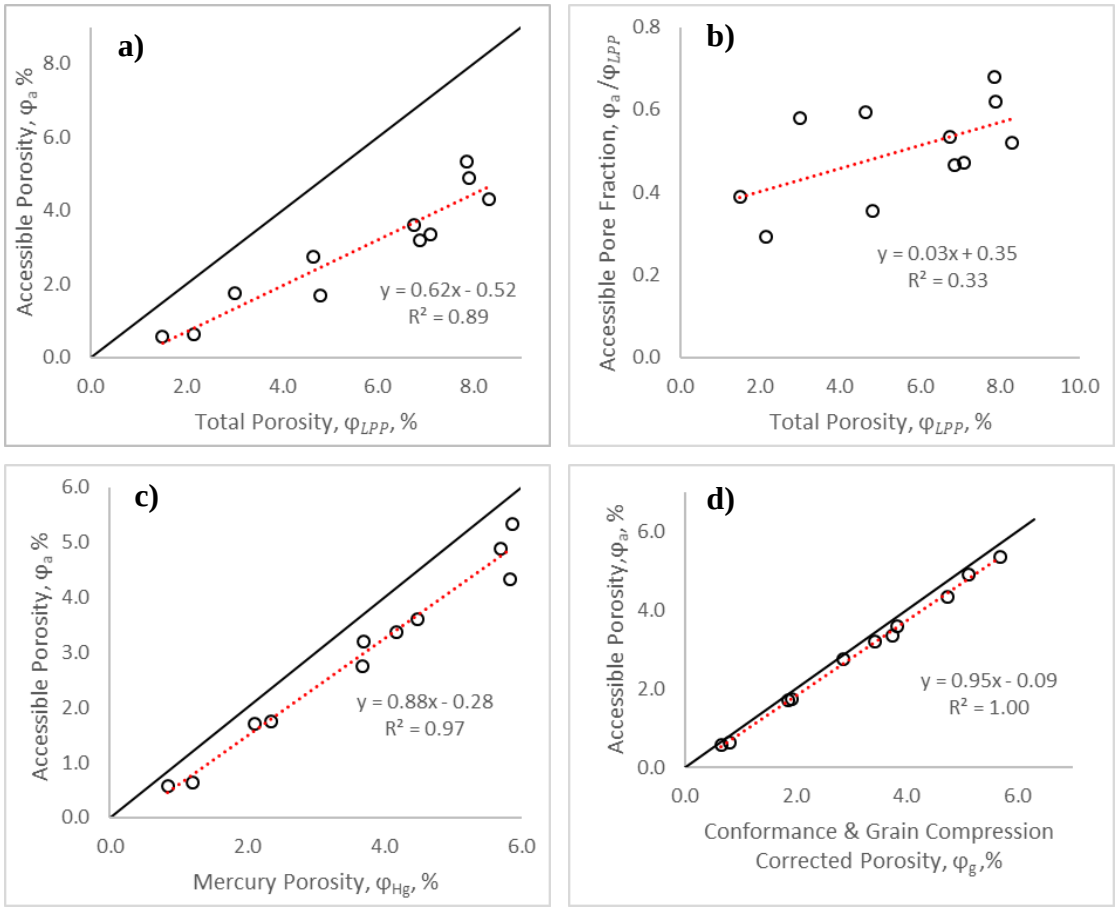


**Figure 6.7: Results for 11 Barnett samples a) Accessible porosity vs total porosity b) Accessible pore fraction vs total porosity c) Accessible porosity vs MICP porosity without any corrections d) Accessible porosity vs conformance and grain compression corrected MICP porosity**

When outcomes are analyzed for Haynesville samples, the results are similar to that of Barnett samples, accessible porosity increases with an increase in total porosity, although the increasing slope is relatively low (**Figure 6.8a)**. However, surprisingly, results indicate that fraction of accessible porosity ($\phi_a/\phi_{LPP}$) decreases with an increase in total porosity as it is shown in **Figure 6.8b,** although relationship is comparably weak. This inverse relation might seem surprising, however if ratio of mercury porosity (without any corrections) to total porosity ($\phi_{Hg}/\phi_{LPP}$) is plotted it also shows a negative relationship with total porosity. Thus, it can be speculated that,

this inverse relationship is characteristics of Haynesville formation, which can be related to porosity type (inorganic) and porosity shape (slit). On the other hand, accessible porosity values are strongly and directly related to results from MICP without any correction, $\phi_{Hg}$ and with conformance and grain compression correction, $\phi_g$ (**Figure 6.8c-d).** Once again, any deviation from unit slope is due to compressibility effect as discussed before.

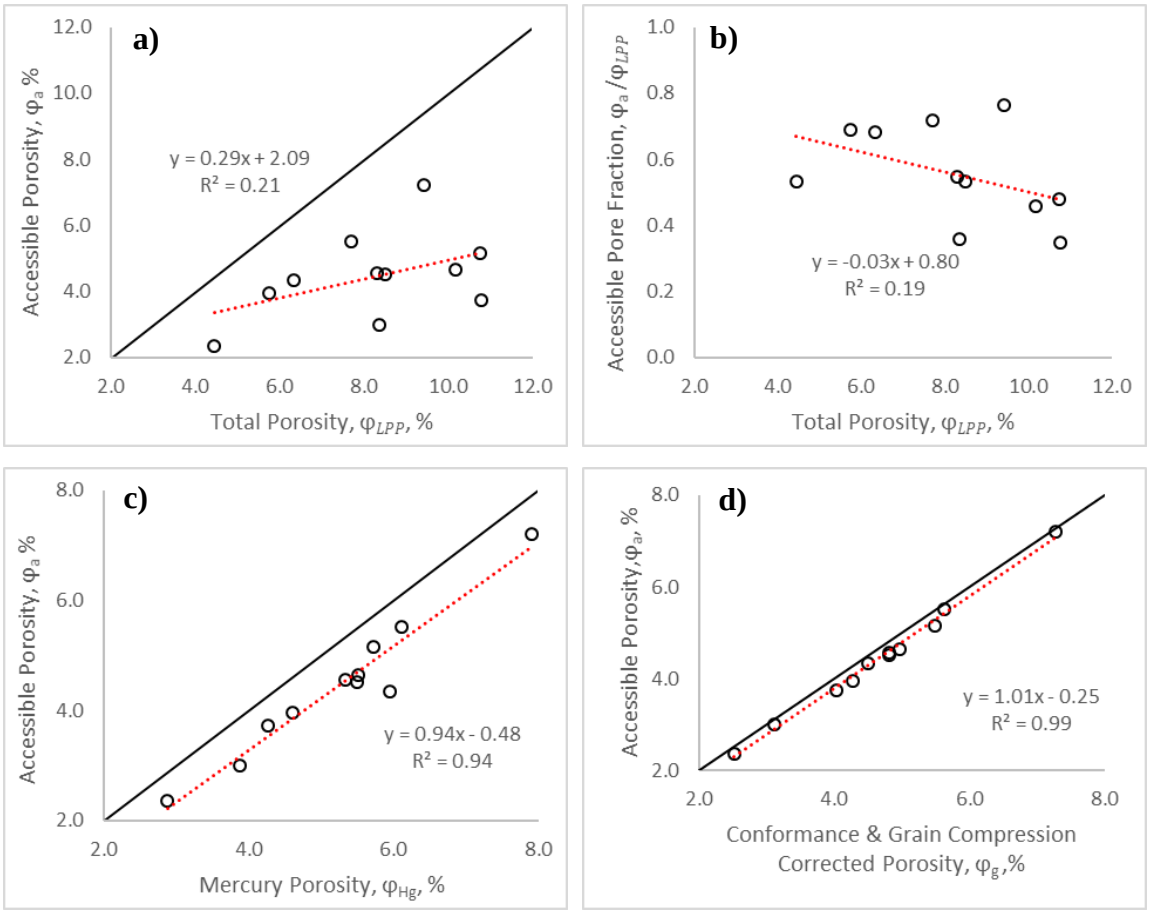


**Figure 6.8: Results for 11 Haynesville samples a) Accessible porosity vs total porosity b) Accessible pore fraction vs total porosity c) Accessible porosity vs MICP porosity without any corrections d) Accessible porosity vs intrusion corrected MICP porosity**

**Figure 6.9** summarizes and illustrates the contribution of each correction on the calculated porosity fraction values ($\phi/\phi_{Hg}$). In general, conformance correction has the least effect while

inaccessible pore compression correction is the one with highest impact. This influence can be observed more distinguished in the case of Barnett samples. When effect of grain compression is investigated it can be concluded that it is as dominant as inaccessible pore compression correction and, in most cases, it can significantly alter results, which is why the compression correction should also be included in the porosity calculations.

It is worth mentioning that pore accessibility is dynamic and depends on the pore network as well as fluid saturation; thus, the estimated accessible porosity values are likely to be different for various fluids. Which is why, with MICP test, only connectivity of the rock that partially saturated with mercury can be measured; pores smaller than 3 nm which mercury cannot intrude will not be evaluated using the methodology discussed here.

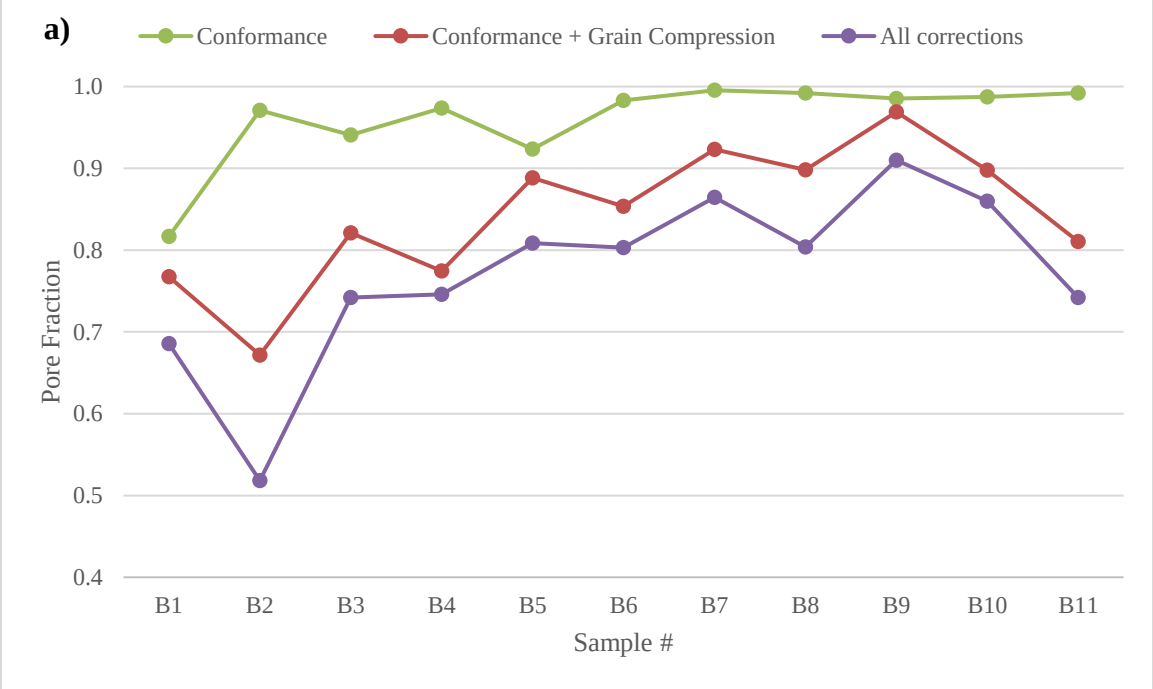

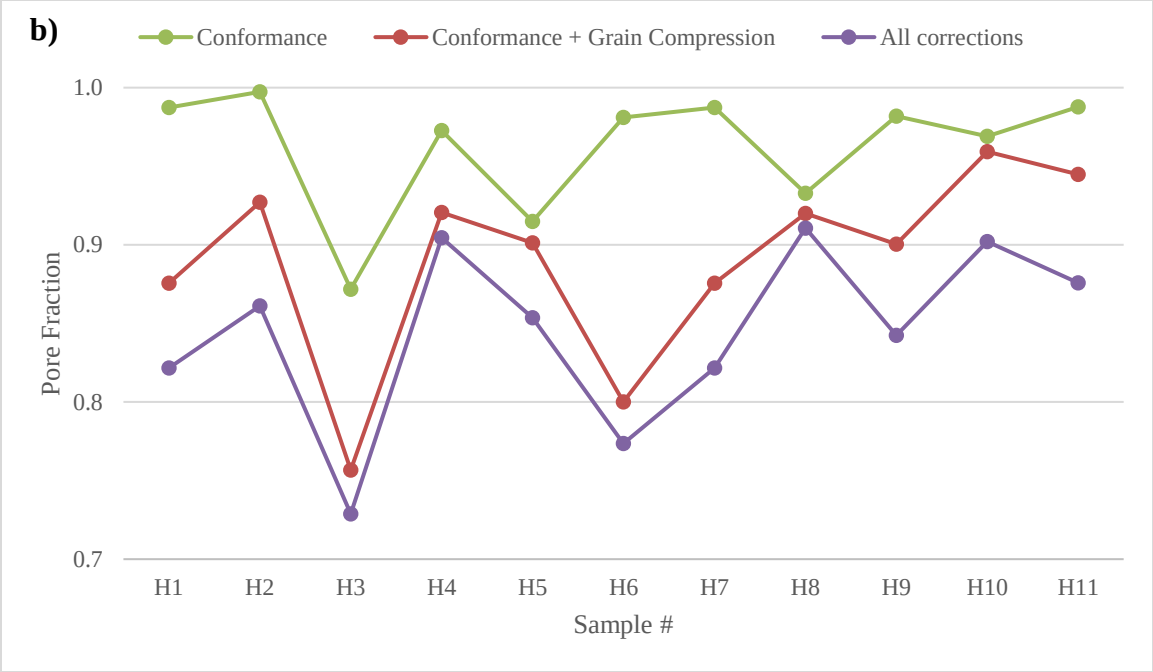


**Figure 6.9: Contribution of each correction factor on calculated accessible porosity a) Barnett b) Haynesville**

## 6.4 Applications

Correcting MICP data will have additional impacts on calculation of saturation curve and pore size distribution. Since suggested corrections reduce volume of mercury that is actually associated with pore volume filling, it does not come as surprise that it will have substantial effect on results.

While not being part of the calculation for compressibility, it is important to establish a general form of volume balance for injected mercury. Total mercury volume at any given pressure is the summation of enveloping mercury volume (conformance), accessible pore intrusion and compression of accessible pores, inaccessible pores and grain.

$$V_{Hg}(\mathrm{P}) = S_i(P)V_{ai} + \left[\left(1 - S_i(P)\right)V_{ai} - \frac{\left(1 - S_i(P)\right)V_{ai}}{\exp\left[\frac{k_\mathrm{p}}{m+1}\left(P^{m+1} - P_i^{m+1}\right)\right]}\right] + \left[V_{inai} - \frac{V_{inai}}{\exp\left[\frac{k_\mathrm{p}}{m+1}\left(P^{m+1} - P_i^{m+1}\right)\right]}\right] +$$

$$+ \left[V_{gi} - \frac{V_{gi}}{\exp\left[\frac{k_g}{m+1}\left(P^{m+1} - P_i^{m+1}\right)\right]}\right] + V_{\mathrm{cf}} \qquad (6.11)$$

where $S_i$ denotes the fraction of accessible pores intruded by mercury. The first four terms on the right-hand side of **Eq. 6.11** represent volume contribution from accessible pore intrusion, accessible pore compression, inaccessible pore compression and grain compression, respectively. Please note that, $S_i$ remains zero until intrusion pressure (during compression stage), which **Eq. 6.11** will converge to **Eq. 6.7** and at final pressure, $S_i$ becomes 1 and **Eq. 6.11** will converge to **Eq. 6.9.** The volume contribution of intrusion, compression in accessible pores, inaccessible pores, and grains during MICP test calculated using **Eq. 6.11** is illustrated in **Figure 6.10** for one of the samples (B11).

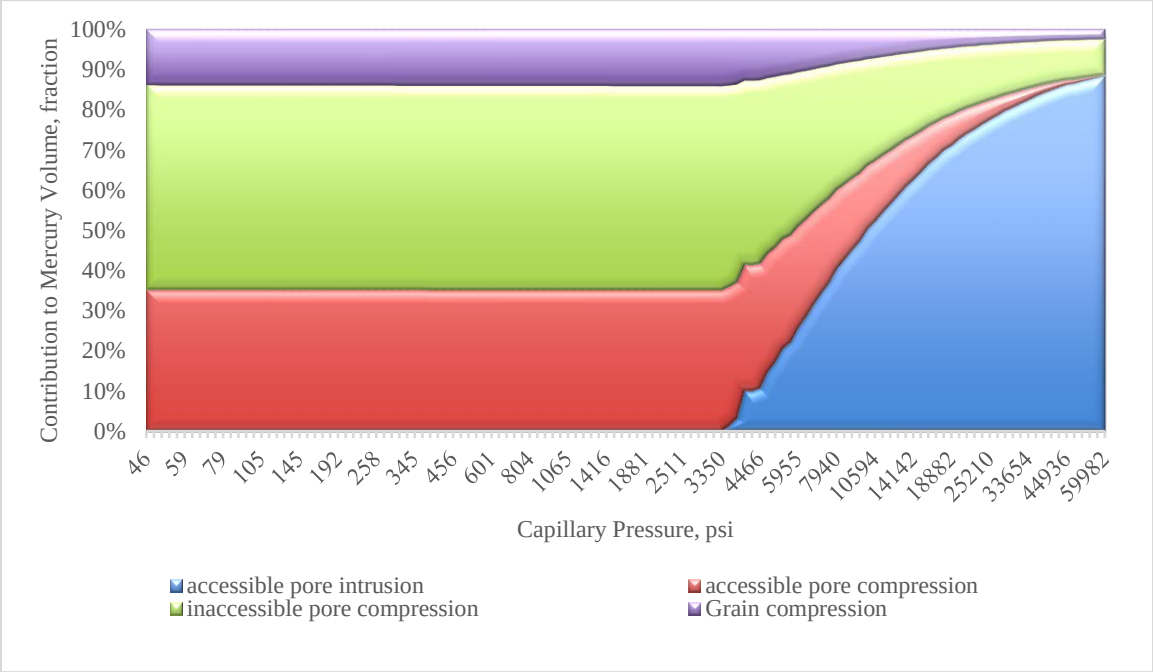


**Figure 6.10: Volume contribution from intrusion and compaction (Sample B11)**

It is important to deduce how much each correction will affect the final interpretation of the MICP curve. As an example of cumulative saturation curve including effects of corrections for sample B1 is shown in **Figure 6.11**, which indicates that results can significantly change when corrections are considered in the calculations. As a result, this will also have an effect on pore size distribution

as shown in **Figure 6.12** suggesting that pore size shifts toward smaller pores when corrections are considered.

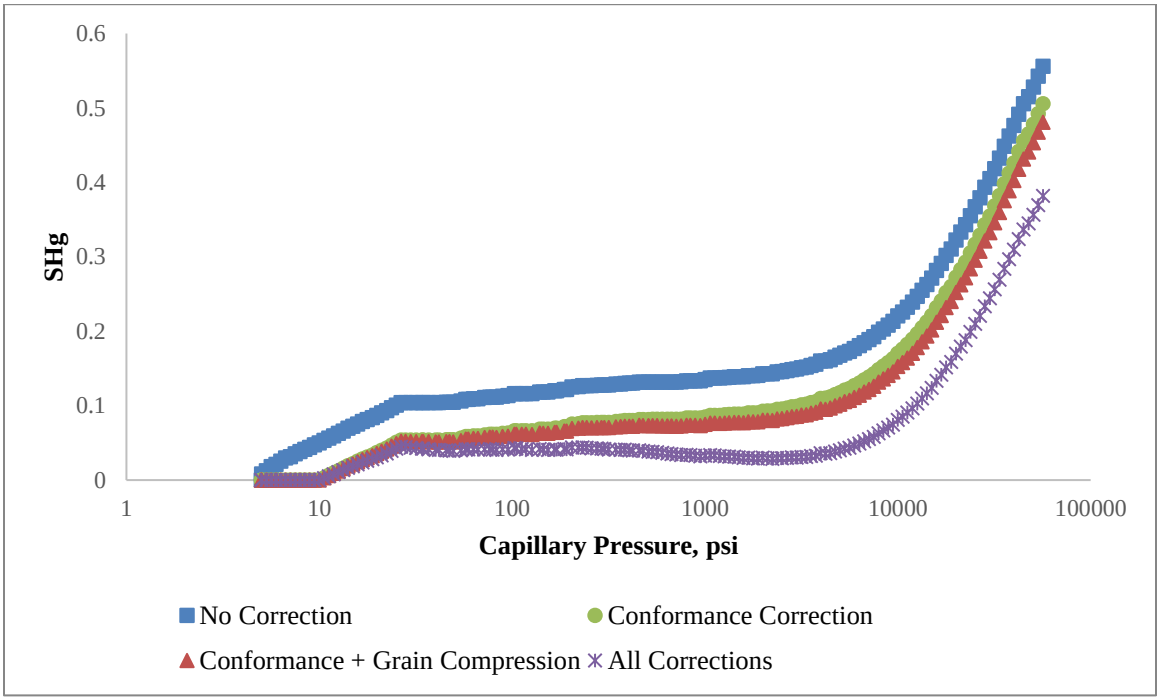


**Figure 6.11: Mercury saturation curve from MICP data (Sample B1)**

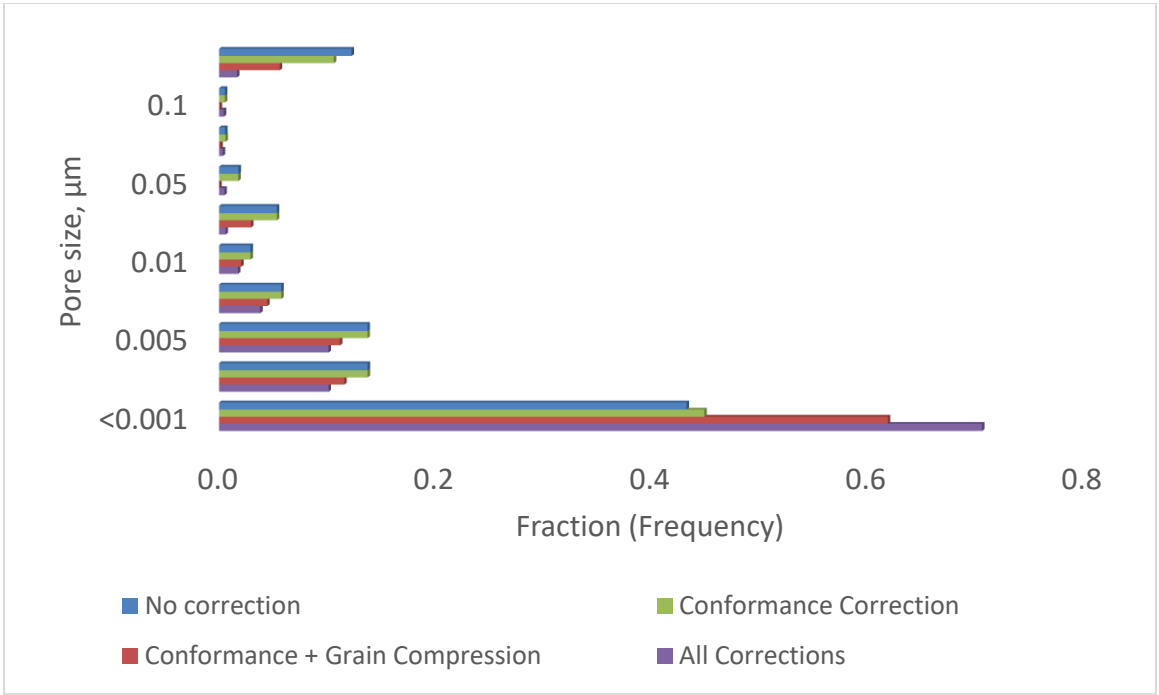


**Figure 6.12: Pore size distribution calculated from MICP data (Sample B1)**

## 6.5 Conclusions

In this chapter accessible porosity is calculated from MICP data for Barnett and Haynesville samples while including effect of pore compressibility. Results suggest that the new system of corrections for conformance, intrusion (pore compressibility during compression stage), and inaccessible pore compressibility after intrusion should be considered to avoid significant reserve overestimation. The main contributions of this chapter are as follows:

- Mathematical model is developed to estimate pore compressibility from MICP.
- Accessible/fluid saturated porosity was calculated considering conformance, grain compressibility and inaccessible pore compressibility corrections.
- Petrophysical properties such as accessible porosity, saturation curve and pore size distribution may change significantly (unfavorably from an operator point of view) according to the proposed model.

# Chapter 7 – Relative Permeability Model Based on Percolation Theory

## 7.1 Introduction

In this chapter, the **Obj. 5** is addressed, where percolation theory has been applied to expresses relative permeability for two phase flow system. Relative permeability, which is a function of fluid saturation, wettability, pore structure, and connectivity is a critical parameter for modeling of multiphase flow in porous media. Although experimental work is a common method to measure relative permeability, alternatively analytical models have been also developed. Based on bundle of tubes model, Corey, (1954) proposed empirical relative permeability model that later was extended by Brooks and Corey, (1964) using capillary pressure data. Similarly, percolation theory-based relative permeability models has been also studied, extensively (Daigle et al., 2015; Ghanbarian-Alavijeh and Hunt, 2012; Ojha et al., 2017c). Using the percolation theory and assuming a power law fit to pore size distribution, critical porosity can be expressed as:

$$\phi_c = \phi p_c = \int_{r_c}^{r_m} sf(r)r^3 dr = s\frac{D}{r_o^{-D} - r_m^{-D}}\frac{r_m^{3-D} - r_c^{3-D}}{3-D}, \tag{7.1}$$

Rearranging **Eq. 7.1**, critical pore size, $r_c$ can be written as:

$$r_c = r_m\left(1 - \frac{\phi}{\beta}p_c\right)^{\frac{1}{3-D}}, \tag{7.2}$$

Similarly, for undersaturated condition **Eq. 7.1 and 7.2** can be expressed as:

$$\phi_c = \phi p_c = \int_{r_{c(s)}}^{r} sf(r)r^3 dr = s\frac{D}{r_o^{-D} - r_m^{-D}}\frac{r^{3-D} - r_c^{3-D}(s)}{3-D}, \tag{7.3}$$

and

$$r_c(S) = r_m\left(\left(\frac{r}{r_m}\right)^{3-D} - \frac{\phi}{\beta}p_c\right)^{\frac{1}{3-D}}, \tag{7.4}$$

It should be noted that one of the major assumptions in **Eq. 7.4** is that, critical porosity and critical percolation threshold is not function of saturation; critical percolation threshold remain for both

saturated and undersaturated conditions, whereas critical pore throat radius, $r_c$, is changing as a function of saturation:

$$p_c = \frac{r_{\max}^{3-D} - r_c^{3-D}}{r_{\max}^{3-D} - r_{\min}^{3-D}} = \frac{r^{3-D} - r_c^{3-D}(S)}{r_{\max}^{3-D} - r_{\min}^{3-D}} \tag{7.5}$$

Next, relative permeability is estimated as the third power of critical pore throat radius ratio obtained from **Eq. 7.2 and 7.4**:

$$k_{rw} = \frac{r_c^3(S)}{r_c^3} = \left( \frac{\left(\frac{r}{r_m}\right)^{3-D} - \frac{\phi}{\beta} p_c}{1 - \frac{\phi}{\beta} p_c} \right)^{\frac{3}{3-D}}, \tag{7.6}$$

**Eq. 7.6** can be further re-expressed as:

$$k_{rw} = \left( \frac{\frac{\beta}{\phi} - 1 + S_w - S_c}{\frac{\beta}{\phi} - S_c} \right)^{\frac{3}{3-D}}, \tag{7.7}$$

Since relative permeability should yield to zero when $S_w \rightarrow S_c$, Ghanbarian and Hunt (2012) suggested to add crossover saturation ($S_d$) and modified **Eq. 7.7** as:

$$k_{rw} = \begin{cases} \left( \frac{S_w - S_c}{S_d - S_c} \right)^m \left( \frac{\frac{\beta}{\phi} - 1 + S_d - S_c}{\frac{\beta}{\phi} - S_c} \right)^{\frac{3}{3-D}}, & S_c < S_w < S_d \\ \left( \frac{\frac{\beta}{\phi} - 1 + S_d - S_c}{\frac{\beta}{\phi} - S_c} \right)^{\frac{3}{3-D}}, & S_d < S_w < 1 \end{cases} \tag{7.8}$$

In case $\beta/\phi \approx 1$, **Eq. 7.8** can be simplified as:

$$k_{rw} = \begin{cases} \left( \frac{S_w - S_c}{S_d - S_c} \right)^m \left( \frac{S_d - S_c}{1 - S_c} \right)^{\frac{3}{3-D}}, & S_c < S_w < S_d \\ \left( \frac{S_w - S_c}{1 - S_c} \right)^{\frac{3}{3-D}}, & S_d < S_w < 1 \end{cases} \tag{7.9}$$

The power $m$ from **Eq. 7.9** has been reported as 1 or 2. Later, Ohja et al. (2017) extended this model for bimodal fractal pore size distribution cases.

Relative permeability of non-wetting phase was expressed as:

$$k_{rnw} = \begin{cases} \dfrac{(S - S_c)^2}{(S_x - S_c)(1 - S_c)}, & S_c < S_{nw} < S_x \\ \dfrac{(S - S_c)}{(1 - S_c)}, & S_x < S_{nw} < 1 \end{cases} \tag{7.10}$$

where $S_x = S_c + \frac{\phi}{z}$ with z representing coordination number.

Relative permeability models developed based on percolation theory (**Eq. 7.8 and 7.10**) are evaluated for 2 sets of experimental data obtained from Bennion and Bachu, (2008). They have conducted series of $CO_2$ brine drainage and imbibition tests for two shale samples from Alberta. To determine parameters needed for the model, MICP test data is used. However, residual saturations are not calculated from equations; instead, experimentally measured values are used. Results for sample #1 and sample #2 are illustrated in **Figure 7.1 & 7.2** respectively. As it can be observed for sample #1, experimental data and percolation theory-based models fits considerably well for both wetting and non-wetting phases. However, for sample #2 results does not match as good as the first sample; nevertheless, it should be noted that these percolation theory-based relative permeability models have numerous assumptions that will be discussed in the next section and limit their practical applications. For more discussion about application of these models, readers can refer to Ojha et al., (2018, 2017b); they have studied several shale samples in light of various kerogen maturity, and kerogen content.

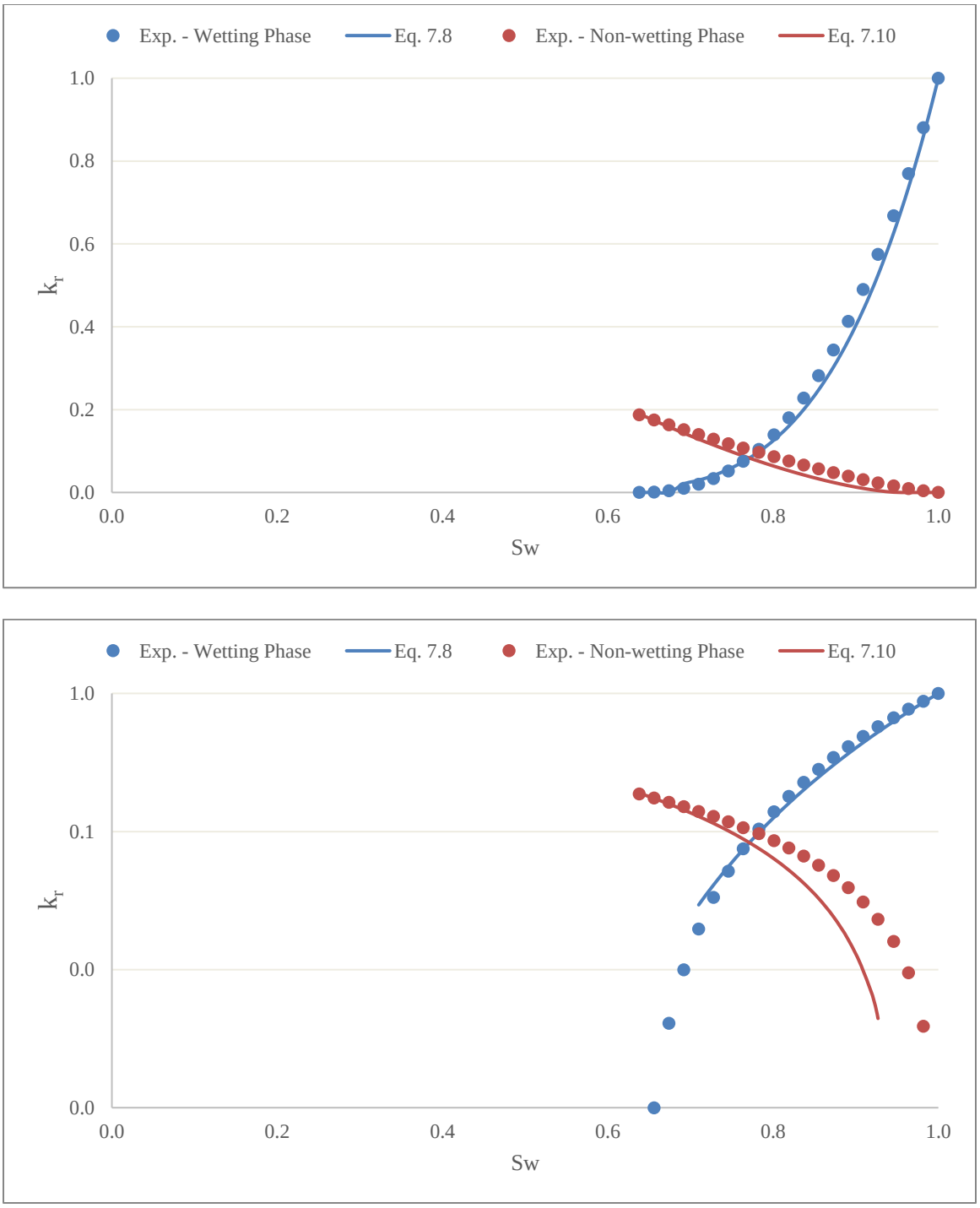


**Figure 7.1: Relative permeability results for shale sample #1 (Calmar)**

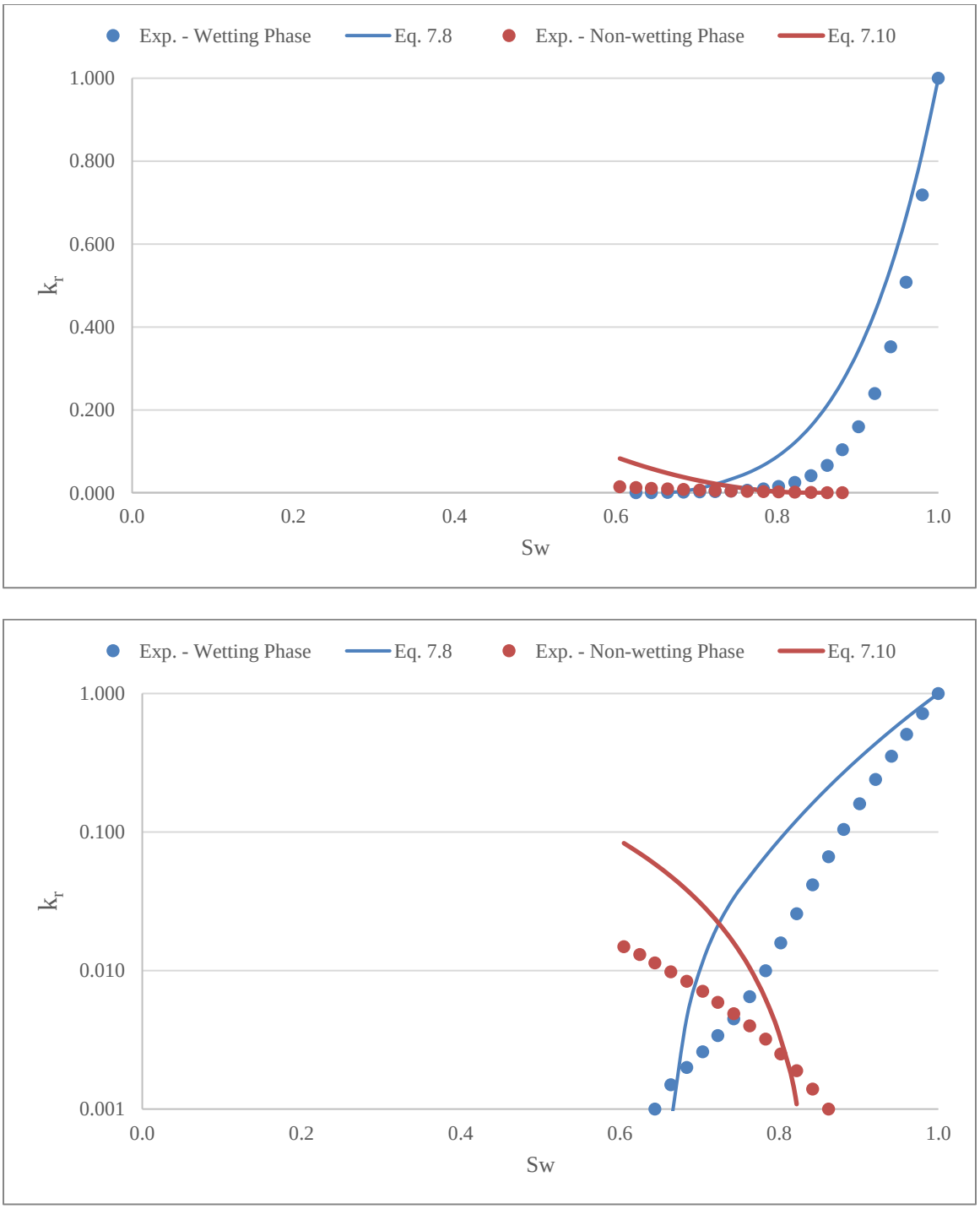


**Figure 7.2: Relative permeability results for shale sample #2 (Colorado)**

### 7.2 Relative Permeability Model - Phase Connectivity

Although relative permeability models described by **Eq. 7.8** and **7.10** have been previously applied to porous media, they suffer from several limitations. One of the major assumptions of these models is that they consider relative permeability for wetting phase to be function of $r_c^3(S)/r_c^3$. However, relative permeability would be much more accurate if it is calculated as the ratio of undersaturated and saturated permeability as:

$$k_r = \frac{r_c^2(S)}{r_c^2}\frac{\sigma_b(S)}{\sigma_b}, \tag{7.11}$$

Another key and probably the most crucial assumption of these models is that, critical percolation threshold, $p_c$ is considered to be equivalent for both saturated and undersaturated pore systems (**Eq. 7.5**). However, numerous studies based on experimental data have shown that, in two phase flow system instead of pore connectivity, phase connectivity should be considered (Alpak et al., 2018; Berg et al., 2016; Blunt, 2017; Herring et al., 2018, 2015, 2013; Liu et al., 2017).

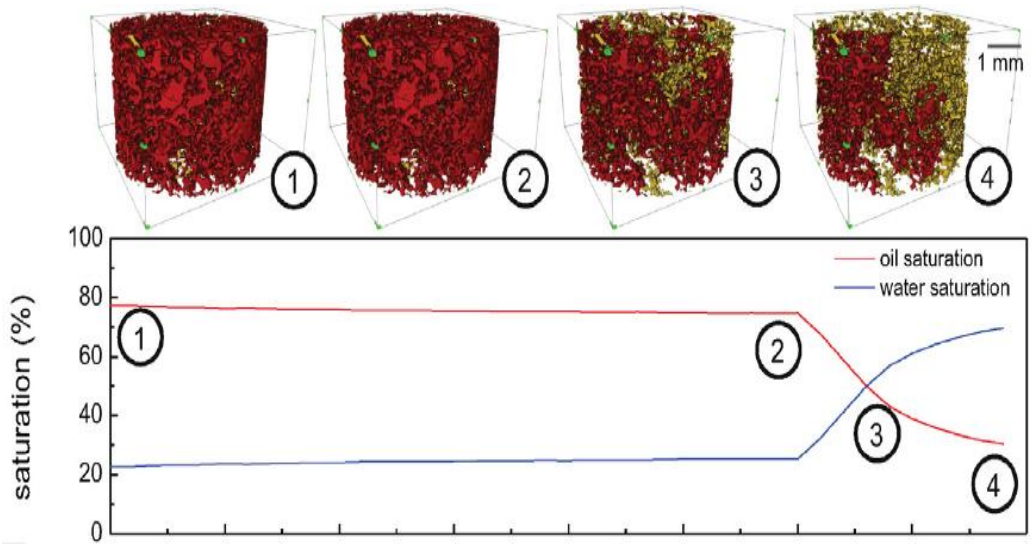


**Figure 7.3: Illustration of phase connectivity as a function of saturation (Berg et al. 2016)**

As shown in **Figure 7.3**, phase connectivity is increasing with increasing saturation; thus, connectivity described with percolation threshold, $p_c$ is strong function of fluid saturation and

time. Considering dynamic phase connectivity/percolation threshold altering with fluid saturation and time, and further combining **Eq. 7.11** with permeability model developed based on percolation theory **(Eq. 2.32)**, relative permeability model can be rewritten as:

$$k_r = \frac{\frac{r_m^2}{c}\phi S\left[1-\left(\frac{1}{1+t}\right)^{3-D}\right]^t (1-p_c(S))^{\frac{2}{3-D}}}{\frac{r_m^2}{c}\phi\left[1-\left(\frac{1}{1+t}\right)^{3-D}\right]^t (1-p_c(s=1))^{\frac{2}{3-D}}} \tag{7.12}$$

which can be further simplified considering the same maximum pore throat radius and fractal dimension for both undersaturated and saturated porous media:

$$k_r = S\left(\frac{1-p_c(S)}{1-p_c(s=1)}\right)^{\frac{2}{3-D}} \tag{7.13}$$

Alternatively, substituting from Daigle (2016) permeability model (**Eq. 2.12**), relative permeability relation can be expressed as:

$$k_r = S^2\left(\frac{1-p_c(S)}{1-p_c(s=1)}\right)^{\frac{2}{3-D}+2} \tag{7.14}$$

To validate the new proposed model (**Eq. 7.13**), two sets of experimental data from the literature (strongly water-wet sintered glass (Robuglass) and Bentheimer sandstone) are used (Liu et al., 2017); in their study, fluid spatial distribution of the samples has been imaged and analyzed using the Euler Poincare Characteristics (EPC). Finally, relative permeability is estimated for each sample using Lattice Boltzmann Method (LBM). They have observed that, non-wetting phase relative permeability is strong function of Euler characteristics of saturated phase, which they have correlated as a power law function. Following Blunt (2017), EPC can be expressed in terms of coordination number as:

$$e_{3D} = N - C = n_p - n_t = n_p(1 - z/2) \tag{7.15}$$

where N is the number of isolated pore structures in a 3D rock sample, C is the number of tunnels (redundant pore-system connections), $n_p$ is the number of pore bodies, $n_t$ is the number of pore throats, and $z$ is the average coordination number. Expressing percolation threshold as a function of coordination number as $p_c = 1.5/z$ (Sahimi 1995), **Eq. 7.15** can be rearranged as:

$$1 - p_c = \frac{0.25n_p - e_{3D}}{n_p - e_{3D}} \tag{7.16}$$

Using EPC and relative permeability values reported by Liu et al., (2017), **Eq. 7.13** and the effect of phase connectivity are studied here. First, the normalized average coordination number of the saturating phase as a function of fluid saturation is evaluated. As shown in **Figure 7.4**, there is a strong relationship between phase connectivity described by coordination number and phase saturation, as expected.

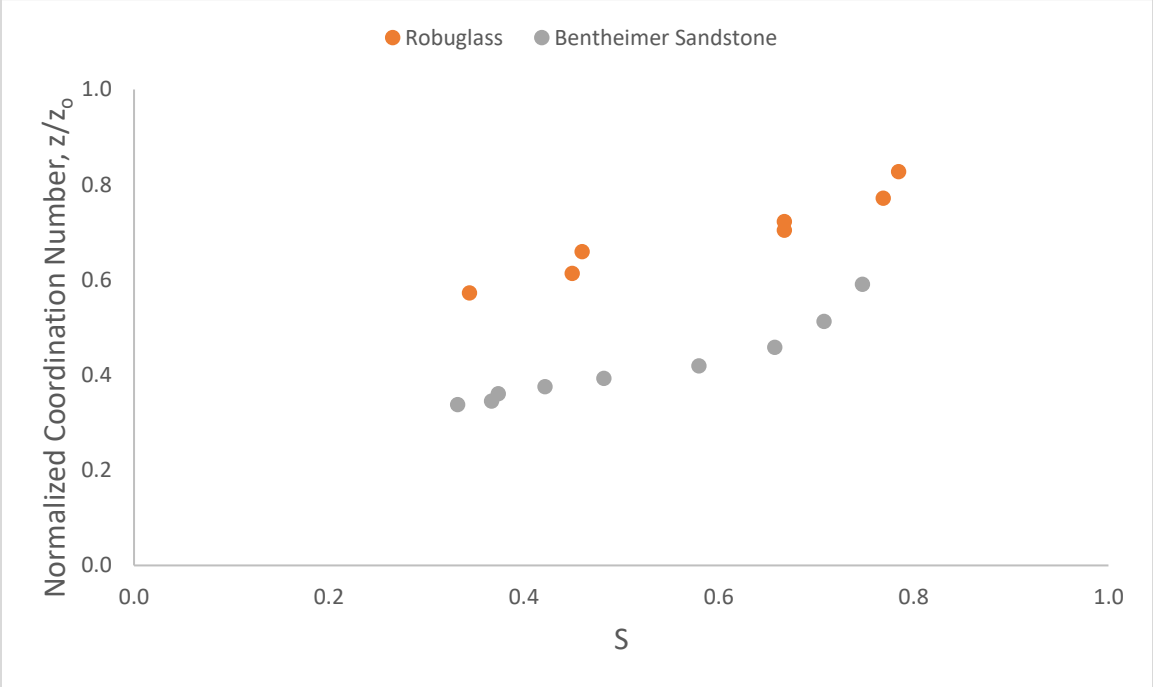


**Figure 7.4: Coordination number of the saturating phase as a function of saturation**

Next, ratio of relative permeability to saturation, $k_r/S$ is plotted as a function of $(1 - p_c)$ as shown in **Figure 7.5**. The relations observed in **Figure 7.5** is consistent with Eq. **7.13**, strong power law

relationship $a(1-p_c(s))^b$. Please note that, the exponent from power law function, $b$ corresponds to $\frac{2}{3-D}$, where constant term, $a$ corresponds to $\frac{1}{(1-p_c(s=1))^{\frac{2}{3-D}}}$.

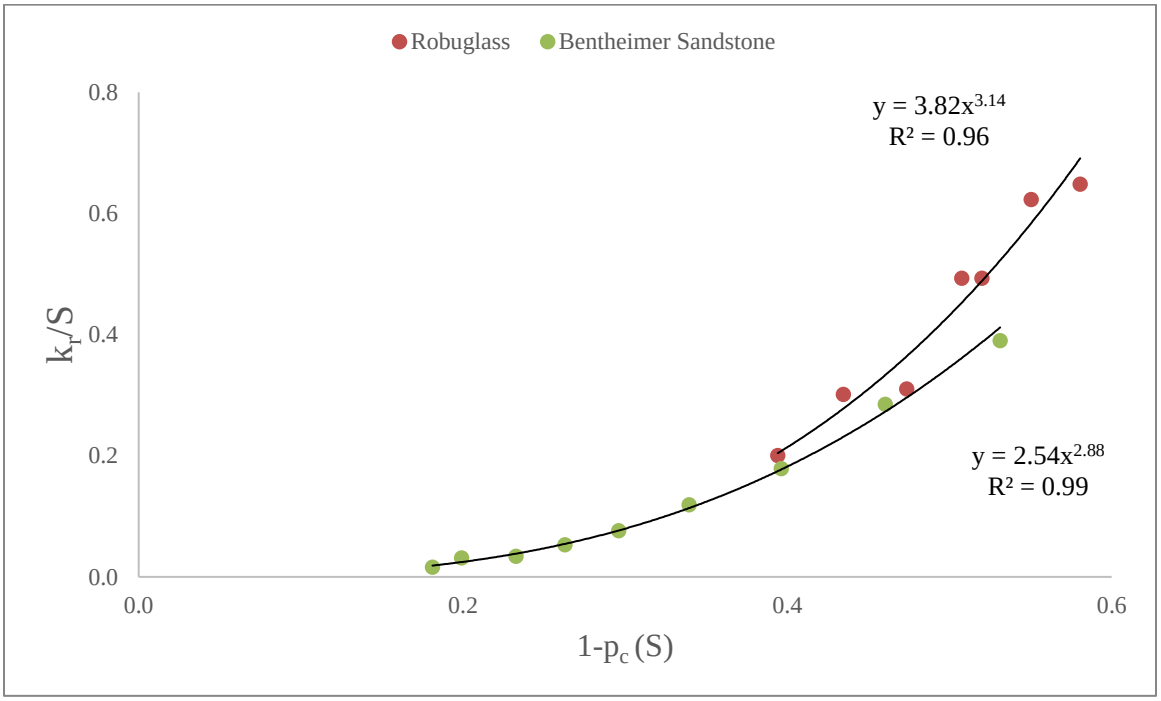


**Figure 7.5: Relative permeability estimated from Eq. 7.14**

### *7.2.1 Residual Saturation*

Another challenging assumption in the previously developed models is that residual saturation has been related to critical percolation threshold, $p_c$ of pore structure. Thus, those models predict that both wetting phase and non-wetting phases have the same residual saturations. Which is why to match the relative permeability data from shale samples (**Figure 7.1** & **7.2**), experimentally measured residual saturation are used instead of analytically determined values.

However, it has been discussed in the literature that, residual saturation for wetting phase is due to the thin film of that phase covering the pore surface. For non-wetting phase, the condition at which

snap-off will occur can be expressed based on the ratio of the threshold capillary pressures for snap-off, $P_c^{snap}$ and piston-like advance, $P_c^{piston}$ (Blunt 2017):

$$P_{cR}^{I} = \frac{P_c^{snap}}{P_c^{piston}} = \frac{r_p}{r_t}\frac{\left(1-\tan\theta_A \tan\beta\right)}{C_I} \tag{7.17}$$

where $r_p$ is pore body radius, $r_t$ is pore throat radius, $\theta_R$ is advancing contact angle, $\beta$ is the corner half-angle, and $C_I$ is coefficient depending on pore geometry and contact angle being between 1 and 2. Based on **Eq. 7.17**, Blunt (2017) suggested that, there are mainly four parameters that control the trapping of non-wetting phase. Two parameters favoring the snap-off are the smaller corner half-angle and stronger wetting condition (smaller $tan\theta_R$ and $tan\beta$).

Another important parameter is pore body to throat aspect ratio, $r_p/r_t$, which needs to be more than 2 to allow occurrence of trapping. To understand impact of aspect ratio on residual saturation, Tran (2017) have analyzed the pore size distribution obtained from SEM images and MICP test data, where former represents pore body and the latter corresponds to pore throat size. Next, he investigated the relationship between the ratio of pore body obtained from SEM images to pore throat from MICP to the amount of mercury trapped inside the samples after MICP unloading (the intrusion/extrusion difference), which a strong correlation has been observed (**Figure 7.6**). The results obtained from Tran (2017) study is consistent with the experimental observations from Wardlaw and McKellar, (1981) and Chatzis et al., (1983). In both studies, the most dominant factor on the amount of trapping is the pore to throat aspect ratio and the effect of connectivity on residual saturations is secondary.

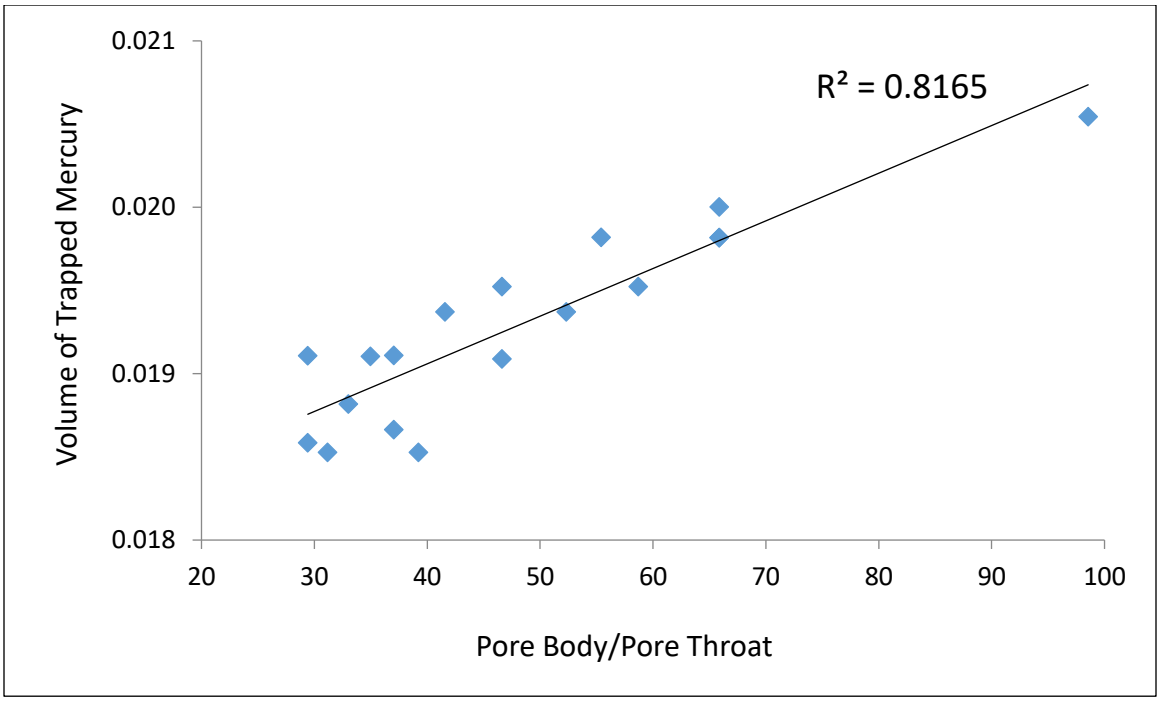


**Figure 7.6: Difference between mercury intrusion and extrusion versus pore body to throat ratio shows a directly proportional relationship (Adopted from Tran 2017).**

Finally, although it has been implicitly expressed in **Eq. 7.17**, another important factor to affect non-wetting phase trapping is the pore connectivity (Blunt 2017). Numerous other studies have also shown that increased phase connectivity reduces the amount of residual saturation as shown in **Figure 7.7.** Based on studies obtained from Herring et al. (2015), strong reduction in normalized residual saturation $(S_r/S_i)$ with an increase in phase connectivity (Euler Poincare Characteristics) can be observed.

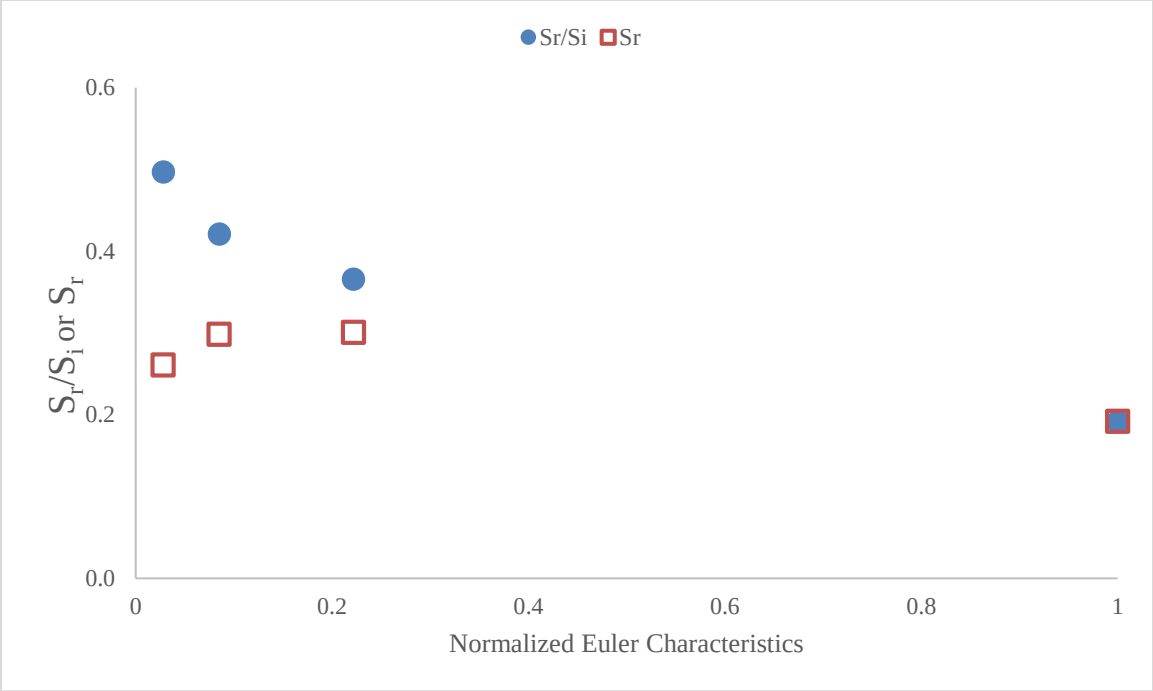


**Figure 7.7: Residual saturation as a function of phase connectivity (modified from Herring et al. 2015)**

## 7.3 Conclusions

In this chapter, percolation theory has been utilized to develop relative permeability to model multiphase flow in porous media. Unlike previously developed models, in the proposed model, dynamic phase connectivity changing with fluid saturation and time has been considered. The new model was validated using experimental data obtained from the literature. Moreover, the major factors affecting non-wetting phase trapping (smaller corner half-angle, stronger wetting condition, pore body to throat ratio, and pore connectivity) were also discussed.

# Chapter 8 – Conclusions and Future Recommendations

This chapter entails the main conclusions and contributions of this dissertation and discusses the recommendations for future research.

## 8.1 Major Contributions and Conclusions

- Analytic permeability model is developed based on critical path analysis (CPA) which is explicitly function of pore connectivity. After redefining critical pore throat, radius, and electrical conductivity from Katz & Thompson model, the new permeability model is expressed as a function of maximum pore radius, porosity, fractal dimension, and average coordination number. When compared with experimental data for tight sandstone and shale sample, proposed model can accurately predict permeability, especially for tight sandstone. In case of shale, higher observed error can be due to miscalculation of critical pore throat radius from MICP test data and/or due to higher estimation of experimentally measured permeability values because of micro-crack effect.
- Accessible porosity and hydraulic connectivity as a function of sample size for Barnett and Haynesville shale formations are evaluated based on MICP data. It has been observed that MICP measured accessible porosity values and matrix permeability decreases significantly with increasing sample size, where this reduction can be explained with pore connectivity/average coordination number reduction.
- Based on CPA-based permeability model explicitly function of pore connectivity impact of connectivity loss under effective stress has been analyzed for shale samples. Orders of magnitude permeability reduction observed under effective stress is explained with micro-crack closure at early stage and pore shrinkage and connectivity loss due to bond breakage at later stage. Based on two samples studied average coordination number has reduced 36% and 51% when effective stress is around17,000 psi.

- A complementary study was conducted to analyze impact of pore connectivity on permeability for the Eagle Ford shale sample. Permeability of 3D pore structure constructed using SEM images is estimated simulating fluid flow using LBM. Additionally, pore connectivity is quantified based on Euler-Poincare Characteristics as a function of sample size. Results indicate that, permeability is around 1.17 μd sample size is at 6 μm, where this value is more than 16 md when sample size is 1 μm; 15000 times reduction is observed. Moreover, the pore connectivity determined through EPC method is consistent with LBM results.
- Accessible/fluid saturated porosity values calculated using mercury injection capillary pressure (MICP) are evaluated for Barnett and Haynesville shale samples. A general approach is proposed to accurately estimate the accessible porosity of shale sample from MICP data considering conformance, grain compressibility, and inaccessible pore compressibility corrections. Accessible porosity calculated for both formations have been analyzed and compared to understand the impacts of pore structure and topology on the connectivity.
- A two-phase relative permeability model based on percolation theory is proposed and impact of the phase connectivity on relative permeability curves is investigated. Validating with experimental data, it has been concluded that, dynamic phase connectivity/percolation threshold should be considered to accurately estimate relative permeability. Moreover, pore connectivity is one of major factors determining the amount non-wetting phase saturation.

## 8.2 Recommendations for Future Work

The proposed future research topics based on the outcomes of this dissertation are listed as follows:

- As extensively discussed in Chapter 2, although CPA-based permeability models have significant advantages including an explicit expression for the pore connectivity, there are some

limitations associated with these models, especially for shale samples. The discrepancy between calculated and experimentally measured values in this dissertation, might be either due to higher estimation of experimental results because of micro-crack effect or miscalculation of critical pore throat radius, $r_c$ obtained from MICP. These limitations associated with shale formations can be extensively investigated with a larger dataset. Since LBM simulations can provide intrinsic permeability values without micro-crack effect, permeability values measured experimentally can be compared with LBM simulation results to understand impact of micro-cracks on permeability measurements. Moreover, LBM simulations results can be compared with MICP based analytic models for the same samples to evaluate accuracy of CPA-based models.

- Moreover, impact of connectivity loss can be evaluated depending on formation and pore type. It can be expected that in slit shape pores connectivity loss will be more pronounced.
- One of the limitations associated with LBM simulations is that, the results obtained from simulations strongly depend upon image resolution and thresholding technique. The effect of resolution and thresholding can be further investigated for more shale samples.
- Percolation theory based relative permeability model can be applied to shale samples after obtaining saturation dependent image stacks. The challenging part of this approach is that, different SEM image stacks for the same sample should be obtained for numerous saturations and then used to calculate saturation-dependent effective permeability through LBM simulations; although this is a comprehensive combined experimental and computational work.

# References


Alpak, F.O., Berg, S., Zacharoudiou, I., 2018. Prediction of fluid topology and relative permeability in imbibition in sandstone rock by direct numerical simulation. Adv. Water Resour. 122, 49–59. https://doi.org/10.1016/J.ADVWATRES.2018.09.001

Arns, C.H., Knackstedt, M.A., Pinczewski, W. V., Mecke, K.R., 2001. Euler-Poincaré characteristics of classes of disordered media. Phys. Rev. E - Stat. Nonlinear, Soft Matter Phys. https://doi.org/10.1103/PhysRevE.63.031112

Bailey, S., 2009. Closure And Compressibility Corrections To Capillary Pressure Data In Shales, in: Presentation given at the CWLS Fall Workshop.

Bennion, B., Bachu, S., 2008. Drainage and Imbibition Relative Permeability Relationships for Supercritical CO2/Brine and H2S/Brine Systems in Intergranular Sandstone, Carbonate, Shale, and Anhydrite Rocks. SPE Reserv. Eval. Eng. https://doi.org/10.2118/99326-PA

Berg, S., Rücker, M., Ott, H., Georgiadis, A., van der Linde, H., Enzmann, F., Kersten, M., Armstrong, R.T., de With, S., Becker, J., Wiegmann, A., 2016. Connected pathway relative permeability from pore-scale imaging of imbibition. Adv. Water Resour. https://doi.org/10.1016/j.advwatres.2016.01.010

Bernabé, Y., Bruderer, C., 1998. Effect of the variance of pore size distribution on the transport properties of heterogeneous networks. J. Geophys. Res. https://doi.org/10.1029/97JB02486

Bernabe, Y., Li, M., Maineult, A., 2010. Permeability and pore connectivity: A new model based on network simulations. J. Geophys. Res. Solid Earth.

Bhandari, A.R., Flemings, P.B., Polito, P.J., Cronin, M.B., Bryant, S.L., 2015. Anisotropy and Stress Dependence of Permeability in the Barnett Shale. Transp. Porous Media 108, 393–411.

Bhatnagar, P.L., Gross, E.P., Krook, M., 1954. A model for collision processes in gases. I. Small amplitude processes in charged and neutral one-component systems. Phys. Rev.

Blunt, M.J., 2017. Multiphase Flow in Permeable Media. Cambridge University Press, Cambridge. https://doi.org/10.1017/9781316145098

Brooks, R.H., Corey, A.T., 1964. Hydraulic properties of porous media, Hydrology Papers.

Bultreys, T., De Boever, W., Cnudde, V., 2016. Imaging and image-based fluid transport modeling at the pore scale in geological materials: A practical introduction to the current state-of-the-art. Earth-Sci. Rev. https://doi.org/10.1016/j.earscirev.2016.02.001

Bustin, R.M., Bustin, A.M.M., Cui, A., Ross, D., Pathi, V.M., 2008. Impact of Shale Properties on Pore Structure and Storage Characteristics, in: SPE Shale Gas Production Conference.

Carman, P.C., 1937. Fluid flow through granular beds. Chem. Eng. Res. Des.

Chalmers, G.R., Bustin, R.M., Power, I.M., 2012. Characterization of gas shale pore systems by porosimetry, pycnometry, surface area, and field emission scanning electron microscopy/transmission electron microscopy image analyses: Examples from the Barnett, Woodford, Haynesville, Marcellus, and Doig units. Am. Assoc. Pet. Geol. Bull. 96, 1099–1119. https://doi.org/10.1306/10171111052

Chatzis, I., Morrow, N.R., Lim, H.T., 1983. Magnitude and Detailed Structure of Residual Oil Saturation. Soc. Pet. Eng. J. https://doi.org/10.2118/10681-PA

Chi, L., Heidari, Z., 2016. Directional-Permeability Assessment in Formations With Complex Pore Geometry With a New Nuclear-Magnetic- Resonance-Based Permeability Model. SPE J. 21, 1436–1449. https://doi.org/10.2118/179734-PA

Civan, F., 2001. Scale effect on porosity and permeability: Kinetics, model, and correlation. AIChE J. 47, 271–287. https://doi.org/10.1002/aic.690470206

Clarkson, C.R., Freeman, M., He, L., Agamalian, M., Melnichenko, Y.B., Mastalerz, M., Bustin, R.M., Radliński, A.P., Blach, T.P., 2012. Characterization of tight gas reservoir pore structure using USANS/SANS and gas adsorption analysis. Fuel 95, 371–385.

Clerc, J.P., Podolskiy, V.A., Sarychev, A.K., 2000. Precise determination of the conductivity exponent of 3D percolation using exact numerical renormalization. Eur. Phys. J. B.

Comisky, J.T., Newsham, K., Rushing, J.A., Blasingame, T.A., 2007. A Comparative Study of Capillary-Pressure-Based Empirical Models for Estimating Absolute Permeability in Tight Gas Sands, in: SPE Annual Technical Conference and Exhibition. Society of Petroleum Engineers. https://doi.org/10.2118/110050-MS

Comisky, J.T., Santiago, M., McCollom, B., Buddhala, A., Newsham, K.E., 2011. Sample Size Effects on the Application of Mercury Injection Capillary Pressure for Determining the Storage Capacity of Tight Gas and Oil Shales, in: Canadian Unconventional Resources Conference. Society of Petroleum Engineers. https://doi.org/10.2118/149432-MS

Corey, A.T., 1954. The interrelation between gas and oil relative permeabilities. Prod. Mon. 19, 39–41.

Curtis, M.E., Ambrose, R.J., Rai, C.S., 2011. Investigating the Microstructure of Gas Shales by FIB/SEM Tomography & STEM Imaging.

Curtis, M.E., Ambrose, R.J., Sondergeld, C.H., 2010. Structural Characterization of Gas Shales on the Micro- and Nano-Scales, in: Canadian Unconventional Resources and International Petroleum Conference. https://doi.org/10.2118/137693-MS

Curtis, M.E., Cardott, B.J., Sondergeld, C.H., Rai, C.S., 2012a. Development of organic porosity in the Woodford Shale with increasing thermal maturity. Int. J. Coal Geol. 103, 26–31.

Curtis, M.E., Sondergeld, C.H., Ambrose, R.J., Rai, C.S., 2012b. Microstructural investigation of

gas shales in two and three dimensions using nanometer-scale resolution imaging. Am. Assoc. Pet. Geol. Bull. 96, 665–677. https://doi.org/10.1306/08151110188

Daigle, H., 2016. Application of critical path analysis for permeability prediction in natural porous media. Adv. Water Resour. 96, 43–54.

Daigle, H., Ezidiegwu, S., Turner, R., 2015. Determining Relative Permeability In Shales By Including The Effects Of Pore Structure On Unsaturated Diffusion And Advection, in: SPE Annual Technical Conference and Exhibition. https://doi.org/10.2118/175019-MS

Dang, S., Gupta, I., Chakravarty, A., Bhoumick, P., Taneja, S., Sondergeld, C., Rai, C., 2017. Recovering elastic properties from rock fragments. Petrophysics.

David, C., Wong, T.F., Zhu, W., Zhang, J., 1994. Laboratory measurement of compaction-induced permeability change in porous rocks: Implications for the generation and maintenance of pore pressure excess in the crust. Pure Appl. Geophys.

Davudov, D., Ghanbarnezhad Moghanloo, R., 2016. Upscaling of pore connectivity results from lab-scale to well-scale for barnett and haynesville shale plays, in: Proceedings - SPE Annual Technical Conference and Exhibition.

Davudov, D., Moghanloo, R.G., 2019. A new model for permeability impairment due to asphaltene deposition. Fuel 235, 239–248. https://doi.org/10.1016/J.FUEL.2018.07.079

Davudov, D., Moghanloo, R.G., 2018a. Impact of pore compressibility and connectivity loss on shale permeability. Int. J. Coal Geol. 187, 98–113.

Davudov, D., Moghanloo, R.G., 2018. Scale-Dependent Pore and Hydraulic Connectivity of Shale Matrix. Energy and Fuels 32. https://doi.org/10.1021/acs.energyfuels.7b02619

Davudov, D., Moghanloo, R.G., 2018b. Chapter Ten – A Special Focus on Formation Damage in Unconventional Reservoirs: Dynamic Production, Formation Damage During Improved Oil

Recovery. https://doi.org/10.1016/B978-0-12-813782-6.00010-5

Davudov, D., Moghanloo, R.G., Dadmohammadi, Y., Curtis, M., Javadpour, F., 2016. Impact of pore topology on gas diffusion and productivity in Barnett and Haynesville shale plays, in: Proceedings of the International Conference on Offshore Mechanics and Arctic Engineering

Davudov, D., Moghanloo, R.G., Lan, Y., 2018a. Evaluation of Accessible Porosity Using Mercury Injection Capillary Pressure Data in Shale Samples. Energy and Fuels 32.

Davudov, D., Moghanloo, R.G., Lan, Y., 2018b. Pore Volume Compressibility in Shale - Revisited, in: SPE Annual Technical Conference and Exhibition. Society of Petroleum Engineers. https://doi.org/10.2118/191700-MS

Degruyter, W., Burgisser, A., Bachmann, O., Malaspinas, O., 2010. Synchrotron X-ray microtomography and lattice Boltzmann simulations of gas flow through volcanic pumices. Geosphere. https://doi.org/10.1130/GES00555.1

Dewers, T.A., Heath, J., Ewy, R., Duranti, L., 2012. Three-dimensional pore networks and transport properties of a shale gas formation determined from focused ion beam serial imaging. Int. J. Oil, Gas Coal Technol. https://doi.org/10.1504/IJOGCT.2012.046322

Dong, H., Blunt, M., 2007. Micro-CT imaging and pore network extraction. Earth Sci. engeneering.

Dong, J.-J., Hsu, J.-Y., Wu, W.-J., Shimamoto, T., Hung, J.-H., Yeh, E.-C., Wu, Y.-H., Sone, H., 2010. Stress-dependence of the permeability and porosity of sandstone and shale from TCDP Hole-A. Int. J. Rock Mech. Min. Sci. 47, 1141–1157.

Doyen, P.M., 1988. Permeability, conductivity, and pore geometry of sandstone. J. Geophys. Res. 93, 7729. https://doi.org/10.1029/JB093iB07p07729

Driskill, B., Walls, J., DeVito, J., Sinclair, S., 2013. 11 Applications of SEM Imaging to

Reservoir Characterization in the Eagle Ford Shale, South Texas, USA.

Evans, J.P., Forster, C.B., Goddard, J. V., 1997. Permeability of fault-related rocks, and implications for hydraulic structure of fault zones. J. Struct. Geol.

Ewing, R.P., Horton, R., 2002. Diffusion in sparsely connected pore spaces: Temporal and spatial scaling. Water Resour. Res. https://doi.org/10.1029/2002WR001412

Ewing, R.P., Hu, Q., Liu, C., 2010. Scale dependence of intragranular porosity, tortuosity, and diffusivity. Water Resour. Res. https://doi.org/10.1029/2009WR008183

Ewing, R.P., Liu, C., Hu, Q., 2012. Modeling intragranular diffusion in low-connectivity granular media. Water Resour. Res. https://doi.org/10.1029/2011WR011407

Gangi, A.F., 1978. Variation of whole and fractured porous rock permeability with confining pressure. Int. J. Rock Mech. Min. Sci. https://doi.org/10.1016/0148-9062(78)90957-9

Ghanbarian-Alavijeh, B., Hunt, A.G., 2012. Unsaturated hydraulic conductivity in porous media: Percolation theory. Geoderma. https://doi.org/10.1016/j.geoderma.2012.04.007

Ghanbarian, B., Hunt, A.G., Ewing, R.P., Skinner, T.E., 2014. Universal scaling of the formation factor in porous media derived by combining percolation and effective medium theories. Geophys. Res. Lett. https://doi.org/10.1002/2014GL060180

Ghanbarian, B., Sahimi, M., 2017. Electrical Conductivity of Partially Saturated Packings of Particles. Transp. Porous Media. https://doi.org/10.1007/s11242-017-0821-4

Giesche, H., 2006. Mercury porosimetry: A general (practical) overview, in: Particle and Particle Systems Characterization. https://doi.org/10.1002/ppsc.200601009

Guiet, J., Reggio, M., Teyssedou, A., 2011. Implementation and Application of the Lattice Boltzmann Method Using Matlab. Eng. Appl. Comput. Fluid Mech. 5, 117–126.

Guise, P., Grattoni, C.A., Allshorn, S.L., Fisher, Q.J., Schiffer, A., 2018. Stress Sensitivity of

Mercury-Injection Measurements. Petrophysics 59, 25–34.

Han, Y., Misra, S., 2018. A unified inversion scheme to process multifrequency measurements of various dispersive electromagnetic properties. J. Appl. Geophys.

Herring, A.L., Andersson, L., Schlüter, S., Sheppard, A., Wildenschild, D., 2015. Efficiently engineering pore-scale processes: The role of force dominance and topology during nonwetting phase trapping in porous media. Adv. Water Resour.

Herring, A.L., Gilby, F.J., Li, Z., McClure, J.E., Turner, M., Veldkamp, J.P., Beeching, L., Sheppard, A.P., 2018. Observations of nonwetting phase snap-off during drainage. Adv. Water Resour. https://doi.org/10.1016/j.advwatres.2018.07.016

Herring, A.L., Harper, E.J., Andersson, L., Sheppard, A., Bay, B.K., Wildenschild, D., 2013. Effect of fluid topology on residual nonwetting phase trapping: Implications for geologic CO2sequestration. Adv. Water Resour. https://doi.org/10.1016/j.advwatres.2013.09.015

Hori, M., Yonezawa, F., 1977. Theoretical approaches to inhomogeneous transport in disordered media. J. Phys. C Solid State Phys. 10, 229–248.

Hu, Q., Ewing, R.P., Dultz, S., 2012. Low pore connectivity in natural rock. J. Contam. Hydrol. 133, 76–83. https://doi.org/10.1016/j.jconhyd.2012.03.006

Hu, Q., Ewing, R.P., Rowe, H.D., 2015. Low nanopore connectivity limits gas production in Barnett formation. J. Geophys. Res. Solid Earth. https://doi.org/10.1002/2015JB012103

Hu, Q., Gao, X., Gao, Z., Ewing, R., Dultz, S., Kaufmann, J., 2014. Pore Accessibility and Connectivity of Mineral and Kerogen Phases for Shales, in: Proceedings of the 2nd Unconventional Resources Technology Conference. https://doi.org/10.15530/urtec-2014-1922943

Hunt, A.., Gee, G.., 2002. Application of critical path analysis to fractal porous media:

comparison with examples from the Hanford site. Adv. Water Resour. 25, 129–146.

Hunt, A.G., 2001. Applications of percolation theory to porous media with distributed local conductances. Adv. Water Resour. 24, 279–307.

Hunt, A.G., Ewing, R.P., Ghanbarian, B., 2014. Percolation theory for flow in porous media.

Hunt, A.G., Sahimi, M., 2017. Flow, Transport, and Reaction in Porous Media: Percolation Scaling, Critical-Path Analysis, and Effective Medium Approximation. Rev. Geophys.

Jiang, Z., Wu, K., Couples, G.D., Ma, J., 2011. The Impact of Pore Size and Pore Connectivity on Single-Phase Fluid Flow in Porous Media. Adv. Eng. Mater. 13, 208–215.

Jones, F.O., Owens, W.W., 1980. A Laboratory Study of Low-Permeability Gas Sands. J. Pet. Technol. https://doi.org/10.2118/7551-PA

Kang, S.M., Fathi, E., Ambrose, R.J., Akkutlu, I.Y., Sigal, R.F., 2011. Carbon Dioxide Storage Capacity of Organic-rich Shales. SPE J. https://doi.org/http://dx.doi.org/10.2118/134583-PA

Kelly, S., El-Sobky, H., Torres-Verdín, C., Balhoff, M.T., 2016. Assessing the utility of FIB-SEM images for shale digital rock physics. Adv. Water Resour. 95, 302–316.

King, H.E., Eberle, A.P.R., Walters, C.C., Kliewer, C.E., Ertas, D., Huynh, C., 2015. Pore Architecture and Connectivity in Gas Shale. Energy & Fuels 29, 1375–1390.

Klaver, J., Hemes, S., Houben, M., Desbois, G., Radi, Z., Urai, J.L., 2015. The connectivity of pore space in mudstones: Insights from high-pressure Wood's metal injection, BIB-SEM imaging, and mercury intrusion porosimetry. Geofluids. https://doi.org/10.1111/gfl.12128

Kuila, U., Prasad, M., Derkowski, A., McCarty, D.K., 2012. Compositional Controls on Mudrock Pore-Size Distribution: An Example from Niobrara Formation, in: SPE Annual Technical Conference and Exhibition. https://doi.org/10.2118/160141-MS

Kwon, O., Kronenberg, A.K., Gangi, A.F., Johnson, B., 2001. Permeability of Wilcox shale and its effective pressure law. J. Geophys. Res. Solid Earth 106, 19339–19353.

Kwon, O., Kronenberg, A.K., Gangi, A.F., Johnson, B., Herbert, B.E., 2004. Permeability of illite-bearing shale: 1. Anisotropy and effects of clay content and loading. J. Geophys. Res. Solid Earth. https://doi.org/10.1029/2004JB003052

Lan, Y., Moghanloo, R.G., Davudov, D., 2017. Pore Compressibility of Shale Formations. SPE J. 22, 1778–1789. https://doi.org/10.2118/185059-PA

Latt, J., 2009. Palabos, Parallel Lattice Boltzmann solver.

Liu, H., Seaton, N.A., 1994. Determination of the connectivity of porous solids from nitrogen sorption measurements-III. Solids containing large mesopores. Chem. Eng. Sci.

Liu, Z., Herring, A., Arns, C., Berg, S., Armstrong, R.T., 2017. Pore-Scale Characterization of Two-Phase Flow Using Integral Geometry. Transp. Porous Media.

Loucks, R.G., Reed, R.M., Ruppel, S.C., Hammes, U., 2012. Spectrum of pore types and networks in mudrocks and a descriptive classification for matrix-related mudrock pores. Am. Assoc. Pet. Geol. Bull. https://doi.org/10.1306/08171111061

Loucks, R.G., Reed, R.M., Ruppel, S.C., Jarvie, D.M., 2009. Morphology, Genesis, and Distribution of Nanometer-Scale Pores in Siliceous Mudstones of the Mississippian Barnett Shale. J. Sediment. Res. https://doi.org/10.2110/jsr.2009.092

Ma, J., Sanchez, J.P., Wu, K., Couples, G.D., Jiang, Z., 2014. A pore network model for simulating non-ideal gas flow in micro- and nano-porous materials. Fuel. https://doi.org/10.1016/j.fuel.2013.08.041

Metwally, Y.M., Sondergeld, C.H., 2011. Measuring low permeabilities of gas-sands and shales using a pressure transmission technique. Int. J. Rock Mech. Min. Sci.

Moghanloo, R.G., Davudov, D., Akita, E., 2018. Formation Damage by Organic Deposition, in: Formation Damage During Improved Oil Recovery.

Montaron, B., 2009. Connectivity theory – a new approach to modeling non-Archie rocks. Petrophysics 50.

Ojha, S.P., Misra, S., Sinha, A., Dang, S., Tinni, A., Sondergeld, C., Rai, C., 2018. Relative Permeability and Production-Performance Estimations for Bakken, Wolfcamp, Eagle Ford, and Woodford Shale Formations. SPE Reserv. Eval. Eng.

Ojha, S.P., Misra, S., Tinni, A., Sondergeld, C., Rai, C., 2017a. Pore connectivity and pore size distribution estimates for Wolfcamp and Eagle Ford shale samples from oil, gas and condensate windows using adsorption-desorption measurements. J. Pet. Sci. Eng.

Ojha, S.P., Misra, S., Tinni, A., Sondergeld, C., Rai, C., 2017b. Relative permeability estimates for Wolfcamp and Eagle Ford shale samples from oil, gas and condensate windows using adsorption-desorption measurements. Fuel 208, 52–64.

Ojha, S.P., Misra, S., Tinni, A., Sondergeld, C.H., Rai, C., 2017c. Estimation of Pore-Network Characteristics and Irreducible Saturations in Wolfcamp and Eagle Ford Shales Using Low-Pressure-Nitrogen-Adsorption/Desorption-Isotherm Measurements. SPE Reserv. Eval. Eng.

Pape, H., Clauser, C., Iffland, J., 2000. Variation of Permeability with Porosity in Sandstone Diagenesis Interpreted with a Fractal Pore Space Model, in: Fractals and Dynamic Systems in Geoscience. Birkhäuser Basel, Basel, pp. 603–619.

Peng, S., Zhang, T., Loucks, R.G., Shultz, J., 2017. Application of mercury injection capillary pressure to mudrocks: Conformance and compression corrections. Mar. Pet. Geol.

Pommer, M., Milliken, K., 2015. Pore types and pore-size distributions across thermal maturity, Eagle Ford Formation, southern Texas. Am. Assoc. Pet. Geol. Bull.

Potter, P.E., Maynard, J.B., Depetris, P.J., 2005. Mud and mudstones: Introduction and overview, Mud and Mudstones: Introduction and Overview.

Revil, A., 2002. The hydroelectric problem of porous rocks: Themodynamic approach and introduction of a percolation threshold. Geophys. J. Int.

Sahimi, M., 2011. Flow and transport in porous media and fractured rock : from classical methods to modern approaches. Wiley-VCH.

Sahimi, M., 1995. Applications of percolation theory. Tectonophysics.

Seaton, N.A., 1991. Determination of the connectivity of porous solids from nitrogen sorption measurements. Chem. Eng. Sci. 46, 1895–1909.

Shen, Z., Sheng, J.J., 2017. Investigation of asphaltene deposition mechanisms during CO2 huff-n-puff injection in eagle ford shale. Pet. Sci. Technol.

Shi, Y., Wang, C.-Y., 1986. Pore pressure generation in sedimentary basins: Overloading versus aquathermal. J. Geophys. Res. 91, 2153. https://doi.org/10.1029/JB091iB02p02153

Sisk, C., Diaz, E., Walls, J., Grader, A., Suhrer, M., 2010. 3D Visualization and Classification of Pore Structure and Pore Filling in Gas Shales, in: SPE Annual Technical Conference and Exhibition. Society of Petroleum Engineers. https://doi.org/10.2118/134582-MS

Sondergeld, C.H., Ambrose, R.J., Rai, C.S., Moncrieff, J., 2010a. Micro-Structural Studies of Gas Shales, in: SPE Unconventional Gas Conference. Society of Petroleum Engineers.

Sondergeld, C.H., Newsham, K.E., Comisky, J.T., Rice, M.C., Rai, C.S., 2010b. Petrophysical Considerations in Evaluating and Producing Shale Gas Resources, in: SPE Unconventional Gas Conference. Society of Petroleum Engineers. https://doi.org/10.2118/131768-MS

Stauffer, D., Aharony,  a, 1994. Introduction to Percolation Theory. Computer

Succi, S., 2001. The lattice Boltzmann equation for fluid dynamics and beyond. Clarendon Press.

Sukop, M.C., Thorne, D.T., 2007. Lattice Boltzmann modeling : an introduction for geoscientists and engineers.

Swanson, B.F., 1981. A Simple Correlation Between Permeabilities and Mercury Capillary Pressures. J. Pet. Technol. https://doi.org/10.2118/8234-PA

Tathed, P., Han, Y., Misra, S., 2018. Hydrocarbon saturation in upper Wolfcamp shale formation. Fuel. https://doi.org/10.1016/j.fuel.2018.01.116

Tinni, A., Fathi, E., Agarwal, R., Sondergeld, C.H., Akkutlu, I.Y., Rai, C.S., 2012. Shale Permeability Measurements on Plugs and Crushed Samples, in: SPE Canadian Unconventional Resources Conference. https://doi.org/10.2118/162235-MS

Tinni, A., Sondergeld, C., Rai, C., 2014. Particle size effect on porosity and specific surface area measurements of shales, in: International Symposium of the Society of Core Analysts. Avignon.

Tinni, A.O., 2015. Pore Connectivity and Hydrocarbon Storage in Shale Reservoirs.

Tran, H.T., Curtis, M.E., Jernigen, J., Sondergeld, C.H., Rai, C.S., 2017. Investigating Microstructural Heterogeneity in Organic Shale via Large-Scale, High-Resolution SEM Imaging, in: Proceedings of the 5th Unconventional Resources Technology Conference. American Association of Petroleum Geologists, Tulsa, OK, USA.

Vermylen, J.P., 2011. Geomechanical Studies of the Barnett Shale, Texas, USA. Stanford University.

Vogel, H.J., 2008. Morphological determination of pore connectivity as a function of pore size using serial sections. Eur. J. Soil Sci. https://doi.org/10.1111/j.1365-2389.1997.tb00203.x

Vogel, H.J., Weller, U., Schlüter, S., 2010. Quantification of soil structure based on Minkowski functions. Comput. Geosci. https://doi.org/10.1016/j.cageo.2010.03.007

Walls, J., Break, S.S., 2011. Eagle Ford shale reservoir properties from digital rock physics. First Break 29.6, 97–101.

Walsh, J.B., 1981. Effect of pore pressure and confining pressure on fracture permeability. Int. J. Rock Mech. Min. Sci. https://doi.org/10.1016/0148-9062(81)90006-1

Walsh, J.B., Brace, W.F., 1984. The effect of pressure on porosity and the transport properties of rock. J. Geophys. Res. 89, 9425. https://doi.org/10.1029/JB089iB11p09425

Wardlaw, N.C., McKellar, M., 1981. Mercury porosimetry and the interpretation of pore geometry in sedimentary rocks and artificial models. Powder Technol.

Washburn, E.W., 1921. Note on a Method of Determining the Distribution of Pore Sizes in a Porous Material. Proc. Natl. Acad. Sci. https://doi.org/10.1073/pnas.7.4.115

Wildenschild, D., Sheppard, A.P., 2013. X-ray imaging and analysis techniques for quantifying pore-scale structure and processes in subsurface porous medium systems. Adv. Water Resour. 51, 217–246. https://doi.org/10.1016/J.ADVWATRES.2012.07.018

Yang, Y., Yao, J., Wang, C., Gao, Y., Zhang, Q., An, S., Song, W., 2015. New pore space characterization method of shale matrix formation by considering organic and inorganic pores. J. Nat. Gas Sci. Eng. https://doi.org/10.1016/j.jngse.2015.08.017

Yao, Y., Liu, D., 2012. Comparison of low-field NMR and mercury intrusion porosimetry in characterizing pore size distributions of coals. Fuel.

Yu, B., Li, J., 2001. Some Fractal Characters of Porous Media. Fractals 09, 365–372.

Zhou, D., Arbabi, S., Stenby, E.H., 1997. A Percolation Study of Wettability Effect on the Electrical Properties of Reservior Rocks. Transp. Porous Media.

Zimmerman, R.W., Somerton, W.H., King, M.S., 1986. Compressibility of porous rocks. J. Geophys. Res. https://doi.org/10.1029/JB091iB12p12765